High Resolution Transmission Electron Microscopy of Green Fluorescent Protein

Micah Knobles

The R. Malcolm Brown Jr. Laboratory for Cellulose and Biofuels Research: The University of Texas at Austin, Department of Molecular Genetics and Microbiology

Table of Contents

Abstract

Using fluorescence and transmission electron microscopy (TEM), this study investigated the structure of a novel recombinant protein used in tagging molecules. This molecule, green fluorescent protein (GFP) exhibited unexpected aggregation phenomena. The fluorescence, an indicator of protein integrity, could be used to test exposure to conditions of the electron microscope. Negative staining with uranyl acetate was explored to demonstrate how TEM might be employed to observe biological samples with high resolution. Extensive circumstantial evidence suggests that discrete GFP molecules were resolved. This study demonstrated that protein structure can be observed with relatively simple negative staining techniques using uranyl acetate. It was determined that the electron beam was primarily responsible for the degradation of protein structure. Crystal formations with uranyl acetate and GFP produced highly ordered monolayers and complex aggregates. These aided in the analysis of the TEM images. Low dose electron beam exposure and the uranyl acetate stain likely protected the GFP sample. His tag labeling of the recombinant GFP sample with nickel-nitrilotriacetic acid Nanogold (Ni-NTA-Nanogold) was used to definitively identify GFP molecules with inconclusive results. Our findings indicate a newfound use of TEM and negative staining in high resolution transmission electron microcopy studies of globular proteins, biological polymers, and small molecules. With further refinements, these techniques would offer a valuable addition to the contributions of cryo-electron microscopy and X-ray crystallography. The work may help us to interpret complex aggregation phenomena and to increase our understanding of amyloid and prion diseases

whose insoluble protein aggregates consisting of tightly packed beta sheets are not amenable to conventional structural biology techniques.

Introduction

Between the powerful tools of x-ray crystallography and nuclear magnetic resonance (NMR) which are ideal for determining precise but static structures of biological molecules, there is the dynamic world of the light and electron microscope. With a practical resolving power of two angstroms (0.2nm), transmission electron microscopy (TEM) is ideally suited for structural biology studies, the imaging of viruses, small organelles, protein complexes, and nucleic acids (Kondo and Brown, 2001). Paradoxically, though TEM possesses intrinsic resolution, high resolution analysis of biological samples remains challenging due to the inherently destructive vacuum and beam of the electron microscope (Brown and Barnes, 2007). Cryo-electron microscopy (cryo-EM) was developed to mitigate somewhat the effects of dehydration and electron radiation that specimens endure and is currently employed for most high resolution studies of biological specimens. However a dependence on image processing and poor contrast between the sample and amorphous ice detract from this technique (Saibil, 2000). Yet cryo-EM remains a powerful tool. The fine details of frozen viruses with sophisticated imaging allows structures 4.5 angstroms apart to be distinguished. At approximately half a nanometer, near-atomic-level details have become available (Jiang et al, 2008). Though simpler, negative staining remains a largely unexplored alternative for high resolution TEM imaging. The staining process, typically done with uranyl acetate (UA), provides excellent contrast and may offer additional protection to the sample form the electron beam (Kondo and Brown, 2001). Furthermore, this study has demonstrated that upon desiccation, aqueous GFP samples form crystals which aid in the analysis of TEM images, but may also protect the sample.

Green fluorescent protein (GFP) was selected for this structural biology study due its ubiquitous use in the biological sciences, resilient structure, and because fluorescence may serve as a useful indicator of protein function. Originally discovered in 1962 within the bioluminescent jellyfish *Aequorea Victoria*, GFP has proved invaluable as an indicator of gene expression and as a fluorescent marker in the localization of proteins and biopolymers. Osamu Shimomura, awarded the Nobel Prize in Chemistry in 2008 for his discovery of GFP, reported its purification and excitation characteristics in 1974 from 30,000 specimens of *Aequorea Victoria*. The wild type GFP exhibits an excitation maximum at a wavelength of 395 nm and a minor excitation peak at 475 nm, while it fluoresces with an emission maximum of 508 nm. In 1996 the molecular structure of GFP was successfully determined by X-ray crystallography. The native 27 kDa protein consists of 238 amino acid residues in a single polypeptide that forms an 11 stranded beta-barrel, with approximate dimensions of three by four nanometers. A single alpha helix within the center of the beta-barrel contains the fluorophore which is responsible for the protein's fluorescence (Yang et al, 1996). Figure 1 displays two representations of GFP in ribbon diagram form. While X-ray crystallography has determined the structure of GFP with a resolution of 2 angstroms or better, little if any published work has attempted to characterize the structure of GFP through transmission electron microscopy. Figure 1 displays two representations of GFP in ribbon diagram form.

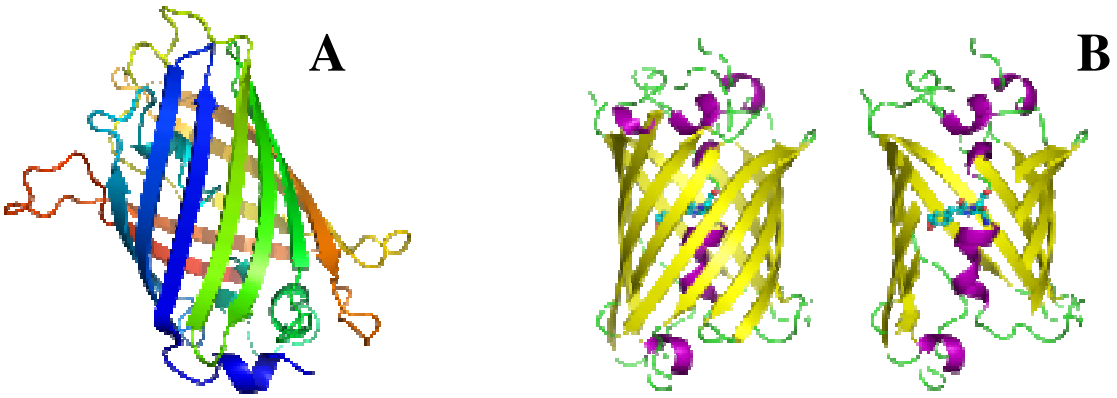

Figure 1: Figure 1A illustrates a GFP ribbon diagram (protein data bank 1EMA) while Figure 1B illustrates two GFP molecules – the first is fully intact while the second removes a side of the beta-barrel to reveal the fluorophore (protein data bank 1GFL)

While the structure of GFP and countless other proteins have been studied and determined through X-ray crystallography, nuclear magnetic resonance techniques, and cryo-EM, little research has been conducted to determine the potential for transmission electron microscopy as a novel method for the study of protein and biopolymer structure at the atomic and molecular levels. The Protein Data Bank (PDB) is the largest repository for the 3-D structural data of biological molecules in the world. As seen in Table 1 which displays the PDP current holdings breakdown as of May 2009, out of 57266 total structures solved only 230 were derived from electron microscopy, which exclusively consists of cryo-EM.

While X-ray crystallography, nuclear magnetic resonance imaging, and cryo-EM are quite powerful and routinely effective at resolving the atomic high resolution structure of proteins, each entails unique disadvantages, such as extensive specimen preparation and harsh conditions which might alter protein conformation. In the case of X-ray diffraction, which represents 90% of protein structures listed in the protein data bank, it is notable that not all proteins can be crystallized and the crystallization process itself

inevitably effects the native conformation of the protein. Furthermore those proteins that form insoluble aggregates can not be imaged with the most powerful techniques. Crucially amyloids and prions, which cause many notable disease in humans, are not suitable for high resolution studies with these methods (Apkarian et al, 2003; Wille et al, 2007). Thus the potential for TEM as a novel method for determining protein structure remains a legitimate subject of scientific interest. In addition TEM has the added benefit of studying proteins and biopolymers in real-time, rather than as static events (Griffiths, 2001). Specimen preparation is relatively simple and inexpensive, while negative staining provides excellent contrast. Previous studies in our lab have resolved polyethylene and cellulose at the atomic level while biological molecules such as Ornithine decarboxylase and Bacitracin have been imaged as well (Brown and Barnes, 2007; Spires and Brown, 1998)

PDB Current Holdings Breakdown

		Molecule Type				
		Proteins	Nucleic Acids	Protein/NA Complexes	Other	Total
Method	X-ray	45825	1141	2110	17	49093
	NMR	6815	850	144	7	7816
	Electron Microscopy	155	16	59	0	230
	Other	110	4	4	9	127
	Total	52905	2011	2317	33	57266

Table 1 displays the PDB Current Holding Breakdown by method used to determine the 3D structure of biological molecules as of May 2009.

For the purposes of this investigation, GFP presented the ideal specimen due to its structural resilience, considering the high vacuum of the electron microscope and the potentially damaging effects of the electron beam. The protein is known to maintain its

fluorescence when fused to other proteins; it is resilient against photo bleaching, moderate oxidizing agents, and moderate reducing agents (2%-β mercaptoethanol, 10 mM DDT). Fluorescence is also maintained after fixation with glutaraldehyde or formaldehyde (Mycek et al, 2003). Additionally studies investigating the denaturation of GFP have shown that the protein is remarkably stable against sodium dodecyl sulfate (SDS), urea, and heat within a pH range of 7.5 to 11.5, but below a pH of 7 is sensitive to denaturation (Alkaabi et al, 2005).

For perhaps the first time in a TEM study, fluorescence has been used as an indicator of protein integrity. The actual fluorophore consists of three sequential amino acids located in the center of the beta-barrel: Ser65, Tyr66, and Gly67. Though common throughout nature, this pattern of residues does not result in fluorescence on its own. Rather the complete beta-barrel structure is essential for the formation and maintenance of the fluorophore. The beta-barrel structure is remarkably stable and remains resistant to reductions in florescence due to fluctuations in pH, temperature, and common denaturants. The exact mechanism of GFP fluorescence is illustrated in Figure 2. Within the hydrophobic environment of the beta-barrel, autocatalytic oxidation between the carboxyl carbon of Ser65 and the amino nitrogen of Gly67 yields an imidazolin-5-one heterocyclic nitrogen ring. Additional oxidation results in the conjugation of the imidazoline ring with Tyr66, which results in the mature fluorophore. The wild GFP fluorophore exists in two states. The protonated form, which predominates, has an excitation maximum at 395 nanometers, while the unprotonated form has an excitation maximum at 475 nanometers. The net fluorescence emission has a maximum peak

wavelength at 507 nanometers, but the emission spectrum is broad and poorly defined (Piston et al, 2007).

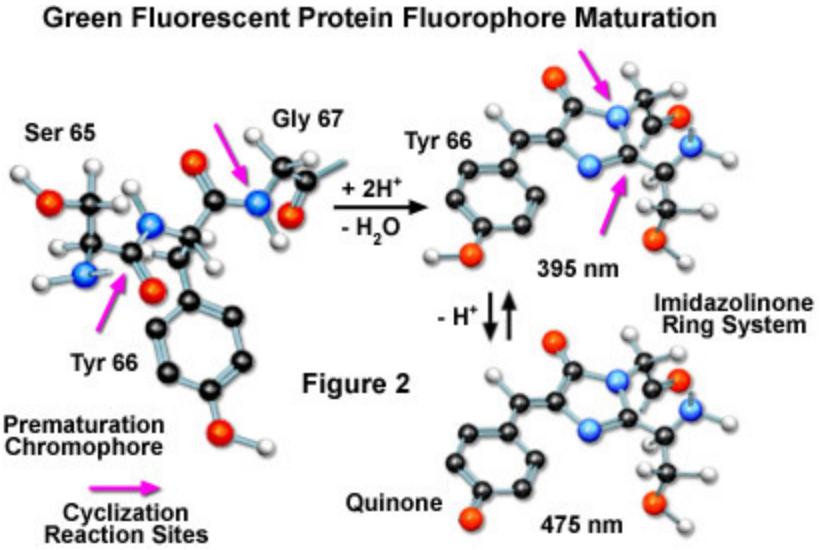

Figure 2 illustrates the maturation of the green fluorescent protein fluorophore (Piston, 2007).

GFP directly isolated from the jellyfish *Aequorea* Victoria, purified by column chromatography, and dialyzed against distilled water to remove salts was found to form elongated needle shaped crystals. These crystals were reported to be 3-µm to under 1-µm wide and some 20- to 100-µm long (Inoue, 2001). Considering that the chemistry of the fluid and conditions under which a crystal is solidified influence the final crystal structure, various crystal structures of GFP and its many variants likely exist. This study reports the crystallization of GFP in a PBS buffer solution under a fluorescent microscope and examines with TEM aggregations that were analogous those crystal structures. At high magnification, images that likely constitute the discrete protein were resolved. In order to definitively identify these objects as GFP molecules, His tag labeling with nickel-nitrilotriacetic acid Nanogold (Ni-NTA-Nanogold) was employed, with inconclusive results.

Methods

Experimental Procedure

This study was conducted over many experiments, with thousands of micrographs taken over the course of approximately two years. The first series investigated a commercially acquired GFP under a fluorescent light microscope. The original concentration of the GFP protein sample was 1 mg/ml in phosphate buffered saline (PBS). An undiluted quantity was placed on a formvar coated copper grid positioned on a glass slide and tested for fluorescence. As the green fluorescent proteins in PBS buffer desiccated, the solution appeared to crystallize and elaborate patterns were observed. These intricate designs were subsequently examined with dark field microscopy.

GFP samples were alternatively examined for fluorescence and subjected, with and without uranyl acetate, to the vacuum of the electron microscope and the electron beam. Specimens were prepared by applying the liquid GFP sample to formvar coated copper grids with a micropipette. Less than 10 μL would be placed on a grid, which due to the liquid's surface tension resembled a small bubble, and allowed to sit for one minute. A micropipette was similarly employed to remove most of the liquid and the solution would desiccate soon afterwards. The first grid was exposed to the TEM vacuum of 10^{-7} Torr for one minute. A second grid was exposed to the vacuum for thirty seconds and then subjected to the electron beam at an accelerating voltage of 100 kV for an additional thirty seconds with the objective aperture removed. The magnification was 45X so that the beam was spread considerably. The electron beam exposure was recorded as

approximately 10.7 pico ammeters. This experiment was subsequently repeated with uranyl acetate by diluting the GFP specimen by half with a 2% uranyl acetate solution.

The second series of experiments examined the commercially acquired GFP sample with transmission electron microscopy. The original concentration of the GFP protein sample was 1 mg/ml in a PBS. The GFP sample was examined using several different preparations, all of which involved applying the liquid specimen to formvar coated copper grids. The liquid would be permitted to sit on the copper grids for up to one minute with the excess being removed with a paper wick. The first protocol consisted of undiluted GFP without any additives. Secondly, specimens were stained with uranyl acetate (UA) by either diluting the GFP specimen directly with 2% UA solution or by washing the grid with 2% UA solution after applying the GFP sample. For most negatively stained examples, the GFP sample was typically diluted by half with 2% UA. As indicated in the results sections, in several experiments the GFP was first diluted with a binding buffer containing 20 mM Tris, .15 M NaCl, and .1% (w/v) Tween 20 adjusted to pH7.6. Finally, colloidal nickel-nitrilotriacetic acid Nanogold (Ni-NTA-Nanogold), designed for labeling His tagged fusion proteins, was used to examine the GFP sample. When viewing the Nanogold directly or combined with UA, the product was diluted 1:5 with deionized water. For viewing the Nanogold only in combination with GFP, 1:5 Nanogold in deionized water was diluted by half with the GFP sample and allowed to incubate for 10 minutes at room temperature. For viewing the GFP, UA, and Nanogold together, two approaches were used after some initial trial and error.

The first protocol called for a stock 1:4 Nanogold solution diluted with the binding buffer. This stock Nanogold solution was then diluted 2:1 with GFP and allowed to incubate for approximately 20 minutes. The Nanogold/GFP solution was then applied to the grids and allowed to sit for 3 minutes. As the solution evaporated, a drop of 2% UA was applied to the grid and then dried with a wick after 5 seconds. The grids were then ready for viewing or alternatively washed once with a washing buffer containing 50 mM Tris, 300 mM NaCl, 20 mM imidazole, and .1% Tween 20 adjusted for pH7.6. The second protocol incubated at room temperature for six minutes 8 µL of GFP with 18 µL of 1:5 Nanogold solution diluted with the binding buffer. 10 µL of UA were then directly added and the solution was applied to the formvar coated copper grids. After sitting for five minutes and nearly evaporating, the excess liquid was removed with a wick and the grid was either ready for viewing or alternatively washed three times with the washing buffer. Once again the excess liquid was removed with a wick. For all electron microscope experiments, the specimens were examined at instrument magnification settings ranging from 3000X to 750,000X. Different spot sizes were used for the electron beam to see what if any affect electron exposure had on the sample.

Sample Specifications

The commercial sample of recombinant enhanced green fluorescent protein (EGFP) in PBS was acquired from BioVision (catalog # 4999-100). The protein is 29 kDa with 265 amino acids, tagged with six histidine residues on both the N and C terminus. The excitation and emission spectra for the recombinant GFP is identical to GFP purified from *Aequorea Victoria*. The sample appears green and has a stated purity greater than 97%.

The colloidal nickel-nitrilotriacetic acid Nanogold (Ni-NTA-Nanogold), simply referred to as Nanogold, was acquired from Nanoprobes (catalog # 2080). The product concentration is 10nmol/ml of Nanogold in 50 mM MOPs adjusted for pH 7.9. As illustrated in Figure 3 below, the product consists of a 1.8 nm Nanogold particle coordinated with multiple nickel-nitrilotriacetic acid functionalities. Each Ni^{2+} coordinates with one nickel-nitrilotriacetic acid and two histidines to form a complex with the His tagged fusion protein.

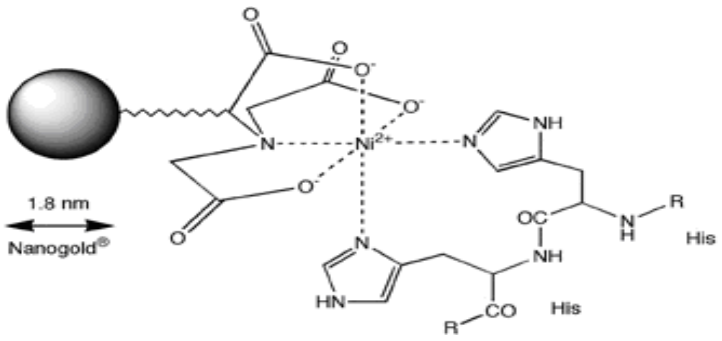

Figure 3 illustrates the nickel-nitrilotriacetic acid Nanogold (Ni-NTA-Nanogold) binding to a His tag.

Microscope Specifications

The visualization devices used for light and fluorescence microscopy consisted of an Olympus BHT and Carl Zeiss Photomicroscope equipped for epifluorescence microscopy. A Philips 420 transmission electron microscope (TEM) was used for the second set of experiments to image the GFP sample. For observation, the specimen was mounted on a copper specimen grid coated with a thin formvar film. Observations were made with an accelerating voltage of 80Kv to 100kV at TEM instrument magnification settings ranging from 3000X to 450000X. Electron signals are converted to high resolution photon images using a Gatan camera system consisting of a yttrium aluminum

garnet (YAG) crystal. The image is subsequently transmitted to a Kontron IBAS imaging system where it is digitized at a final screen magnification of approximately 18 times the instrument magnification. Besides the Gatan camera system, an ion-getter pump maintains a clean vacuum which exceeds 10^{-7} Torr at the specimen level. These factors, along with the use of a tungsten filament and biased electron gun, which provides a uniform and coherent electron beam, allow for this Philips instrument to regularly resolve 3.35 Å graphite lattices in addition to 2.01 Å atomic gold lattices (Sharp and Brown, 1995).

Calibration Protocol

The TEM is regularly calibrated to better than 3.35Å resolution by focusing on graphite lattices. Graphite, the specimen from which all calibrations were made, is one of the allotropes of carbon. Its atomic structure consists of covalently bonded carbons. Each atom, refer to Figure 4, is bound to three other carbon atoms which form flat hexagonally structured sheets. The sheets themselves are not covalently bonded, but rather interact though Van der Waals forces (Spires and Brown, 1998).

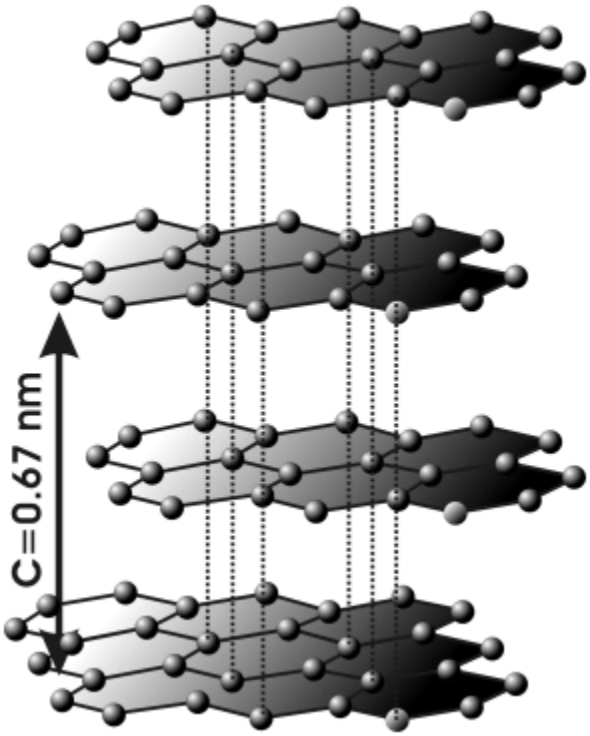

Figure 4: The atomic structure of graphite, represented by layered sheets of hexagonal arrangements of covalently bonded carbon atoms (Jaszczak, 2006).

By summing the number of intervals between carbon lattice sheets, a precise distance can be calculated. Each interval corresponds to .335 nm. As observed in Figure 5, the intervals are easily distinguished at higher magnifications. However, at lower magnifications it is necessary to use points of reference because it becomes increasingly difficult to resolve the individual carbon spacings. For magnifications smaller than 3000X, precise calibrations are infeasible and no reference bars are shown with such images. As observed in Figure 6, two unambiguous points of reference may be used for calibrations at lower magnifications.

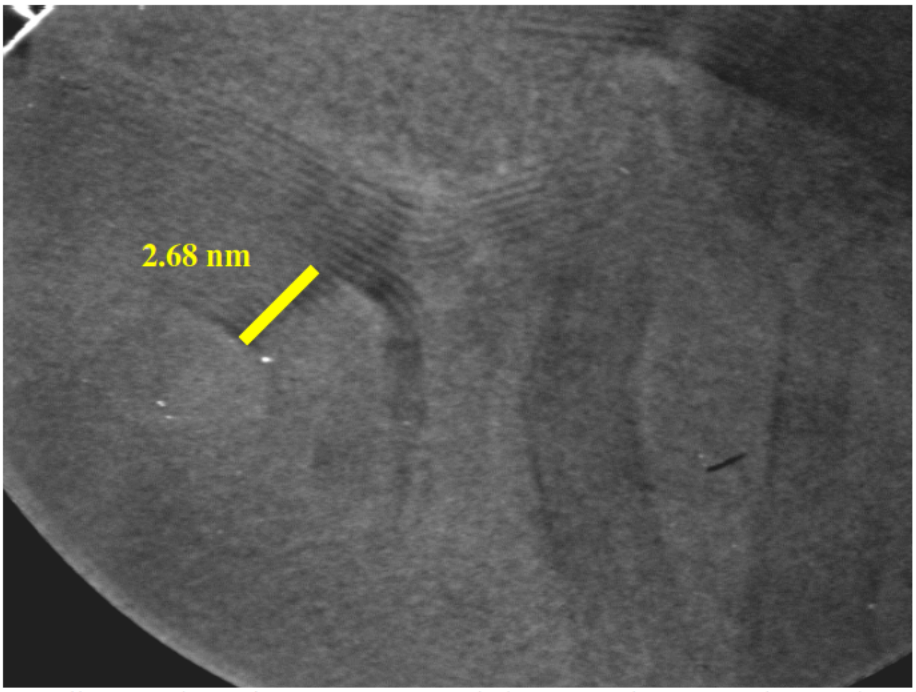

Figure 5: As illustrated at 450000X, 8 intervals between theses graphite carbon lattices correspond to a distance of 2.68 nm.

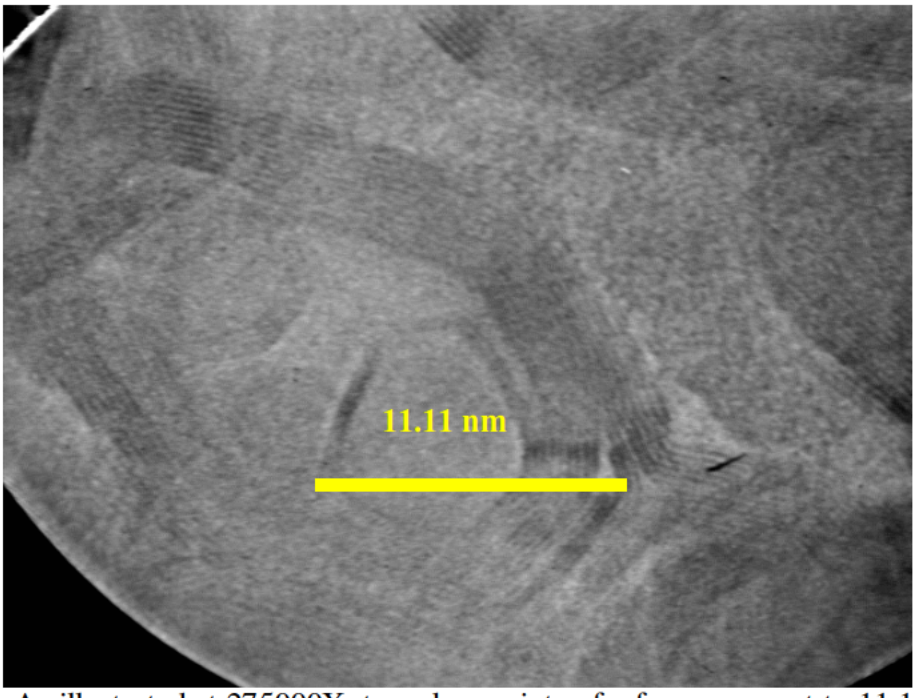

Figure 6: As illustrated at 275000X, two clear points of reference are set to 11.11 nm. This same feature is visible at 96000X where presumably another point of reference might be identified.

Results

The following galleries are organized into two categories. The first contains the fluorescence and light micrographs of the GFP sample, while the second contains electron micrographs. The electron micrograph sections include specimens of pure GFP, GFP negatively stained with uranyl acetate, and GFP labeled with Nanogold.

Fluorescence Micrographs

As expected the commercial GFP sample fluoresced quite strongly under UV light. Figure 7A corresponds to a site where the GFP/PBS solution escaped onto the glass slide. The leading edge of the solution is clearly visible, while what appear to be crystals form as the solution dries. Figure 7B shows similar crystals under higher magnification. Dark field microscopy was used to increase the contrast of the image so that the elaborate patterns might be observed. Figures 7C and 7D show the GFP sample using dark field microscopy. After one year in storage these samples still fluoresced, but at a diminished capacity.

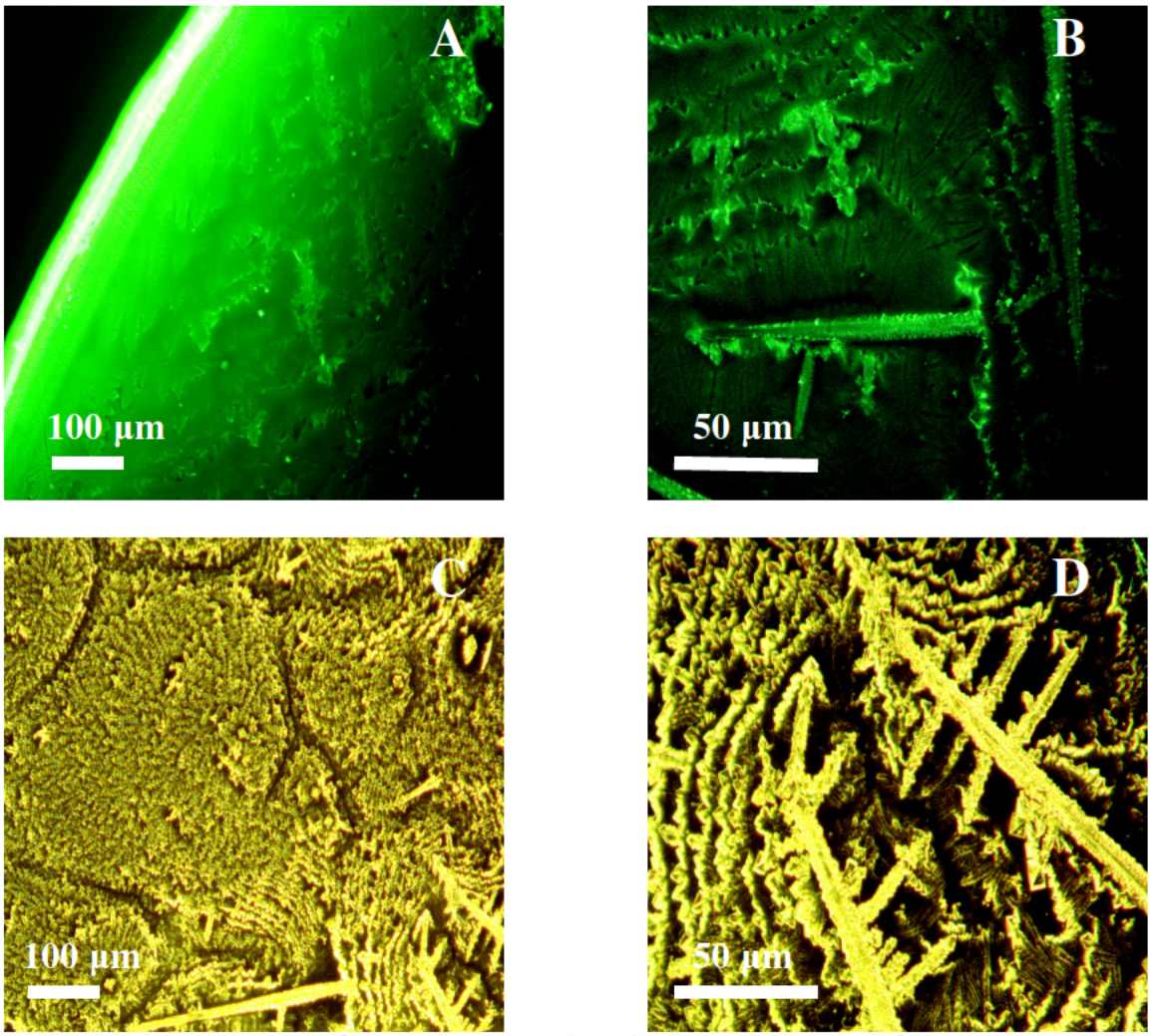

Figures 7A and 7B display the fluorescent micrographs under 10X and 40 X magnification respectively. Figures 7C and 7D display intricate crystal formations, using dark field microcopy, which emerged as the GFP solution dried under 10X and 40 X magnification respectively.

The next phase of the study subjected the GFP sample to the conditions of the electron microscope. The vacuum appeared to have no noticeable effect on fluorescence. However as seen in Figure 8, GFP fluorescence in the specimen region exposed to the electron beam was clearly diminished. The circular shadow corresponds exactly to the electron beam as it appeared in the transmission electron microscope. As seen in Figure 8, crystal formations similar to those in Figure 7 were observed on the grids.

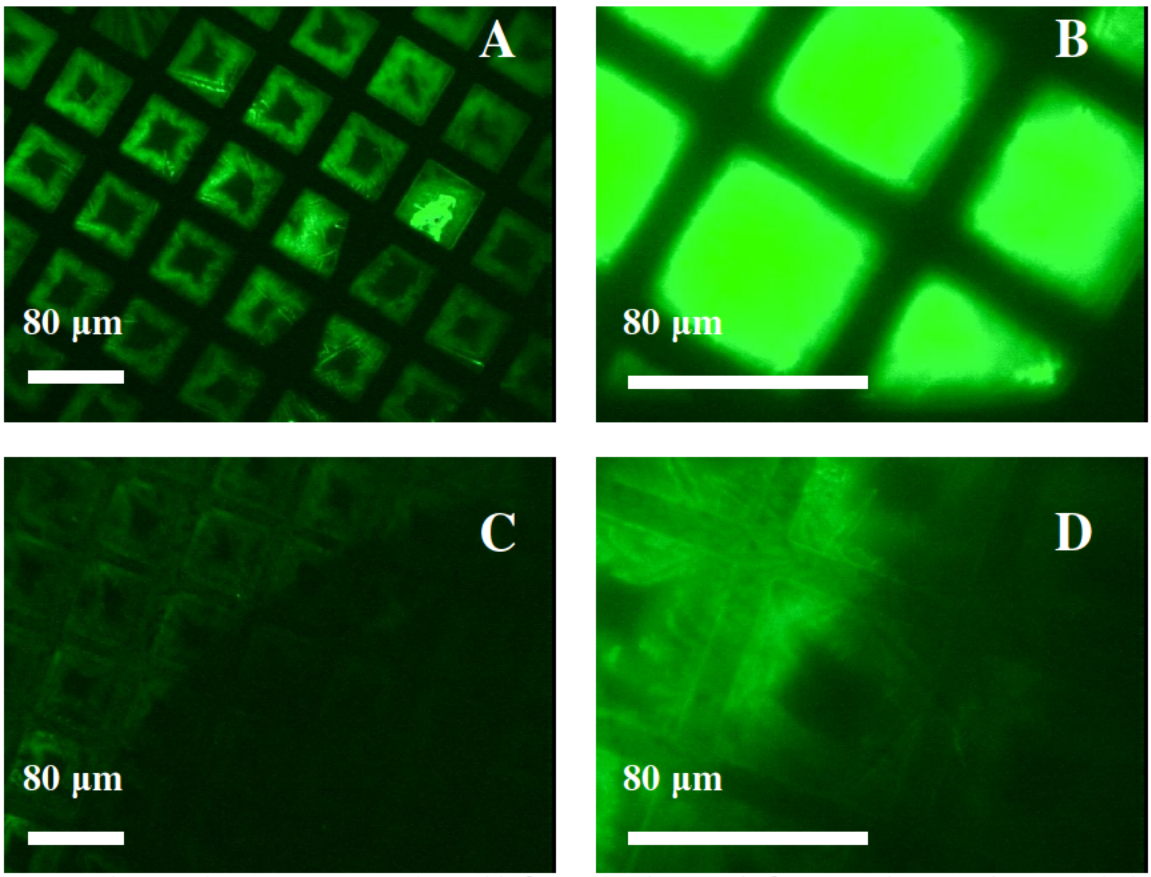

Figure 8 displays the GFP sample on the grid before (8A and 8B) and after (8C and 8D) irradiation with the electron beam. 8A and 8C are taken at 16X, while 8B and 8D are taken at 40X. Notice the near circular region in which fluorescence has been greatly diminished.

For the grids negatively stained with uranyl acetate (UA), the initial florescence was qualitatively less than those prepared with the undiluted GFP. This decrease in florescence is most likely attributable to the decrease in GFP concentration. Figure 9 displays the negatively stained GFP grid at 16X and 40X. Like the unstained GFP sample, the vacuum appeared to have no noticeable effect on fluorescence. Similarly the electron beam noticeably decreased fluorescence. While the GFP stained with UA showed similar crystal formations as those observed in Figure 7, the aggregations and their patterns of deposition were different. Fewer long needle like crystals can be seen and the fluorescent aggregations are less diffuse.

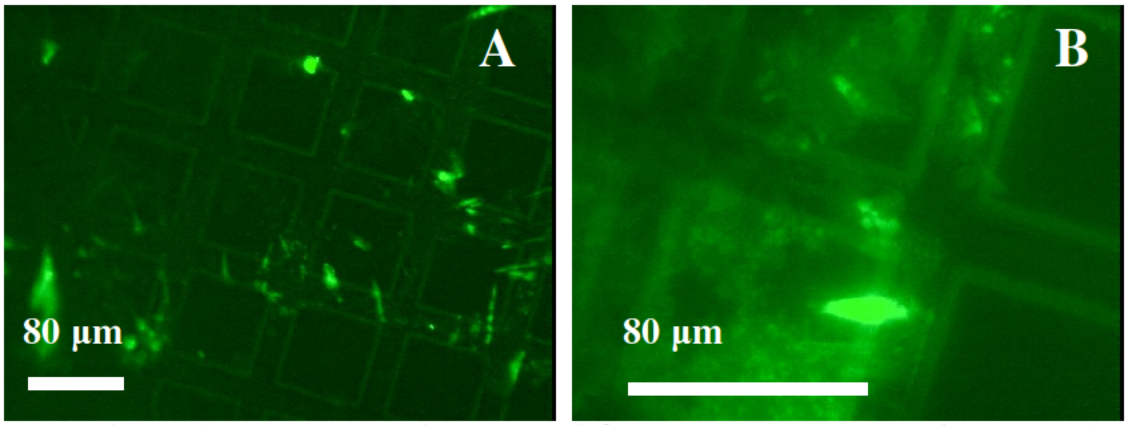

Figure 9 displays the negatively stained GFP sample before electron exposure. 9A is taken at 16X, while 9B is taken at 40X.

The remainder of the results section consists of images captured using transmission electron microscopy (TEM). They show suspected aggregations of GFP under varying degrees of structural order. The following sections are organized as follows. Presented first are micrographs taken of the pure GFP sample, which illustrate the relative instability and low contrast of specimens not stained with uranyl acetate. This is followed by negatively stained GFP specimens depicting large objects that correspond to the crystal formations and fluorescing aggregates observed with fluorescence microscopy. Presented next are aggregations exhibiting what appears to be a monolayer of the discrete GFP protein. Presented third are intermediate and high resolution images of the GFP / uranyl acetate aggregations. Evidence of secondary protein structure such as polypeptide chains, beta sheets, and alpha helices are then showcased. Finally those experiments which employed Nanogold His tag labeling of GFP are presented.

Unstained GFP and Sample Instability in the Electron Beam

Unstained specimens of the undiluted GFP sample coalesced into large fluorescing crystals which exhibited poor contrast as seen in Figure 10. These examples proved to be

quite thick and did not transmit the electron beam very well. However the edges of such objects were finer and did provide some interesting observations. Using spot size one, as evident in Figure 11, quickly destroyed the more delicate examples of crystal structure that radiated from the larger objects. The denser objects themselves also proved to be sensitive to the electron beam and would disintegrate upon prolonged examination. It is speculated that larger objects accumulated a significant amount of charge and subsequently would fly off the viewing area.

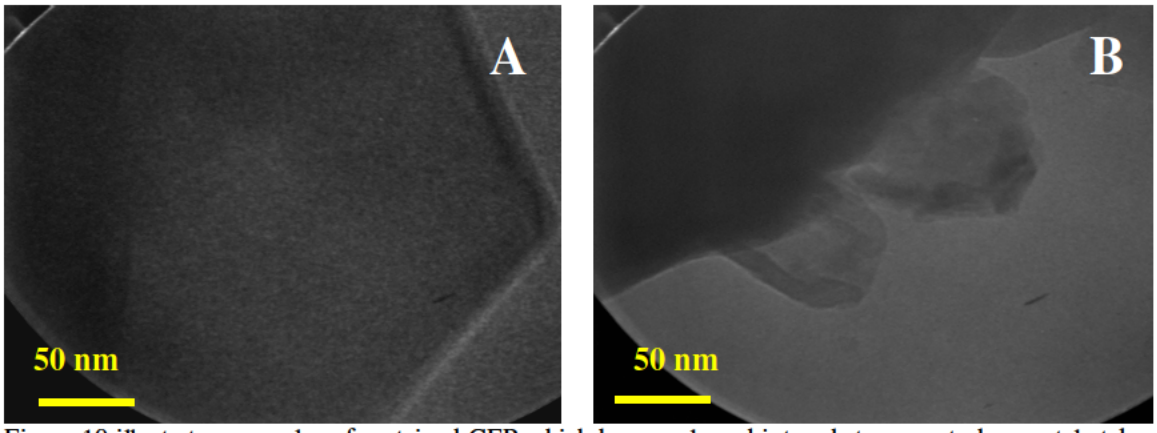

Figure 10 illustrates examples of unstained GFP which have coalesced into what appear to by crystals taken at 45K magnification.

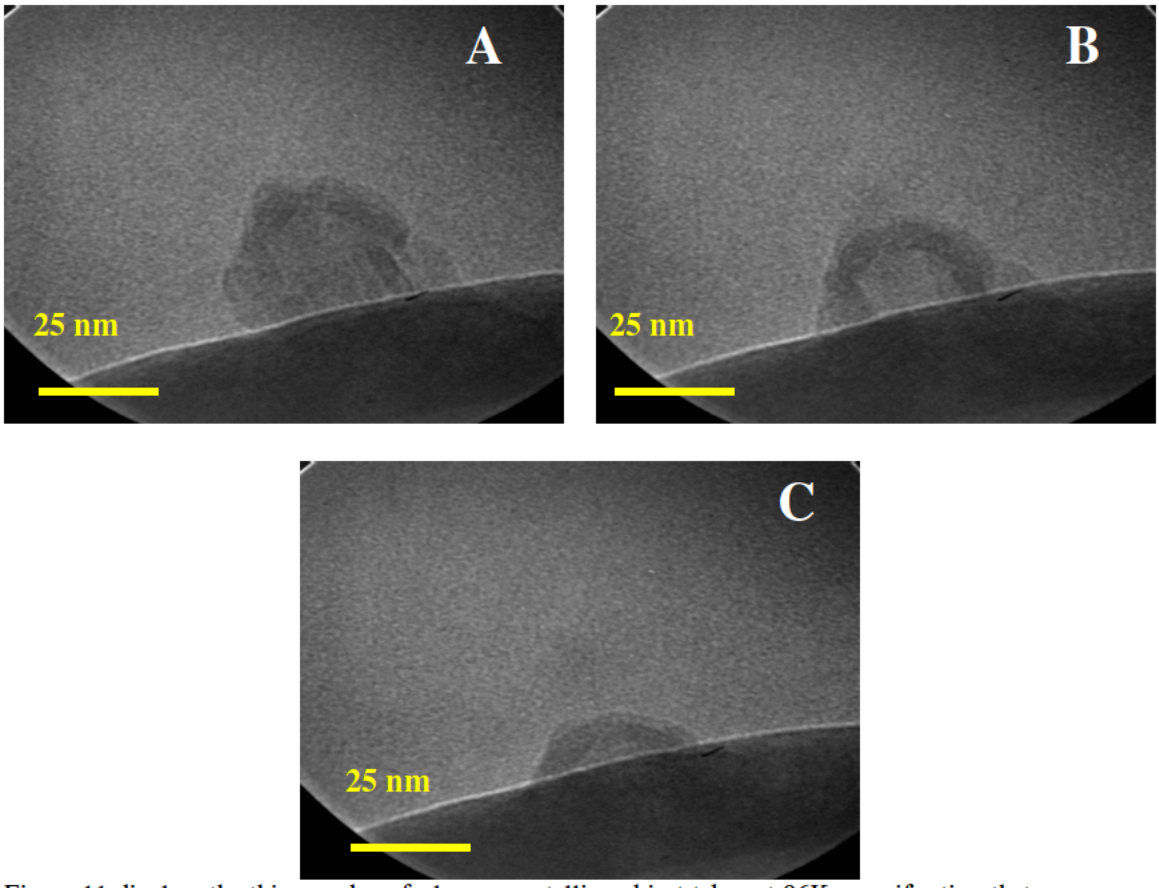

Figure 11 displays the thinner edge of a larger crystalline object taken at 96K magnification that disintegrated upon exposure to the electron beam over the course of several seconds.

The relative sensitivity and low contrast of the unstained GFP specimens made high resolution electron micrographs difficult to acquire. However by reducing the electron beam exposure to spot size four and maximizing the gain of the camera, it was possible to resolve discrete structures at high magnification as seen in Figure 12. In some examples, blue arrows indicate objects approximating the 3 by 4 nm barrel shaped GFP molecule.

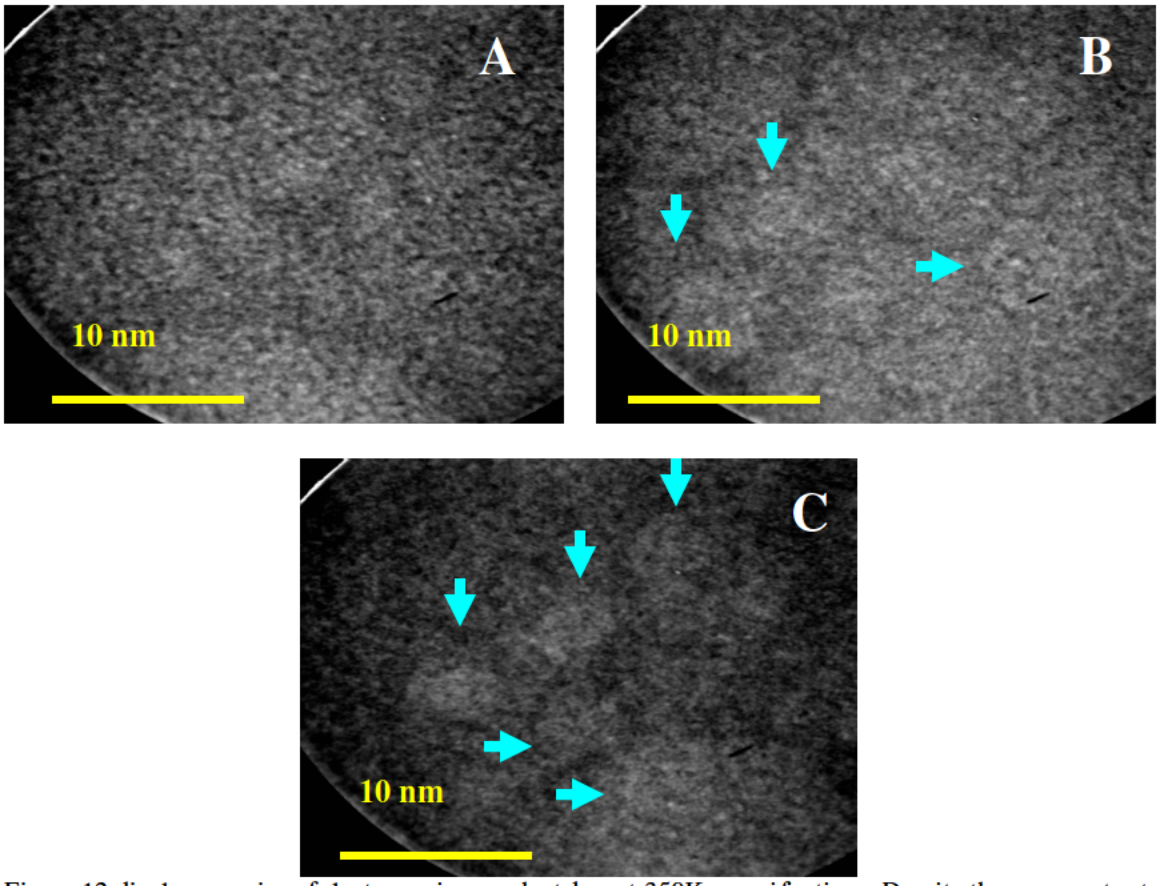

Figure 12 displays a series of electron micrographs taken at 350K magnification. Despite the poor contrast, objects which may represent the GFP molecules are visible.

Crystal Formations and GFP / Uranyl Acetate Aggregations

Unless otherwise specified, the GFP sample was diluted by half with a 2% uranyl acetate solution using a micropipette and then applied to formvar coated copper grids for examination with TEM. This process produced large and distinct aggregations of electron dense material visible at magnifications as low as 3K which undoubtedly correspond to the crystal formations observed using fluorescence microscopy. Figure 13 displays one such example of a crystal formation form 3K to 160K magnification. This particular sample was irradiated for nearly a minute and a half at the same level as the specimen in Figure 8. The well-defined angles of the aggregations suggest a well ordered crystalline structure. They appear to have remained intact despite their exposure to the

electron beam. The uranyl acetate is believed to have offered some protection to the sample.

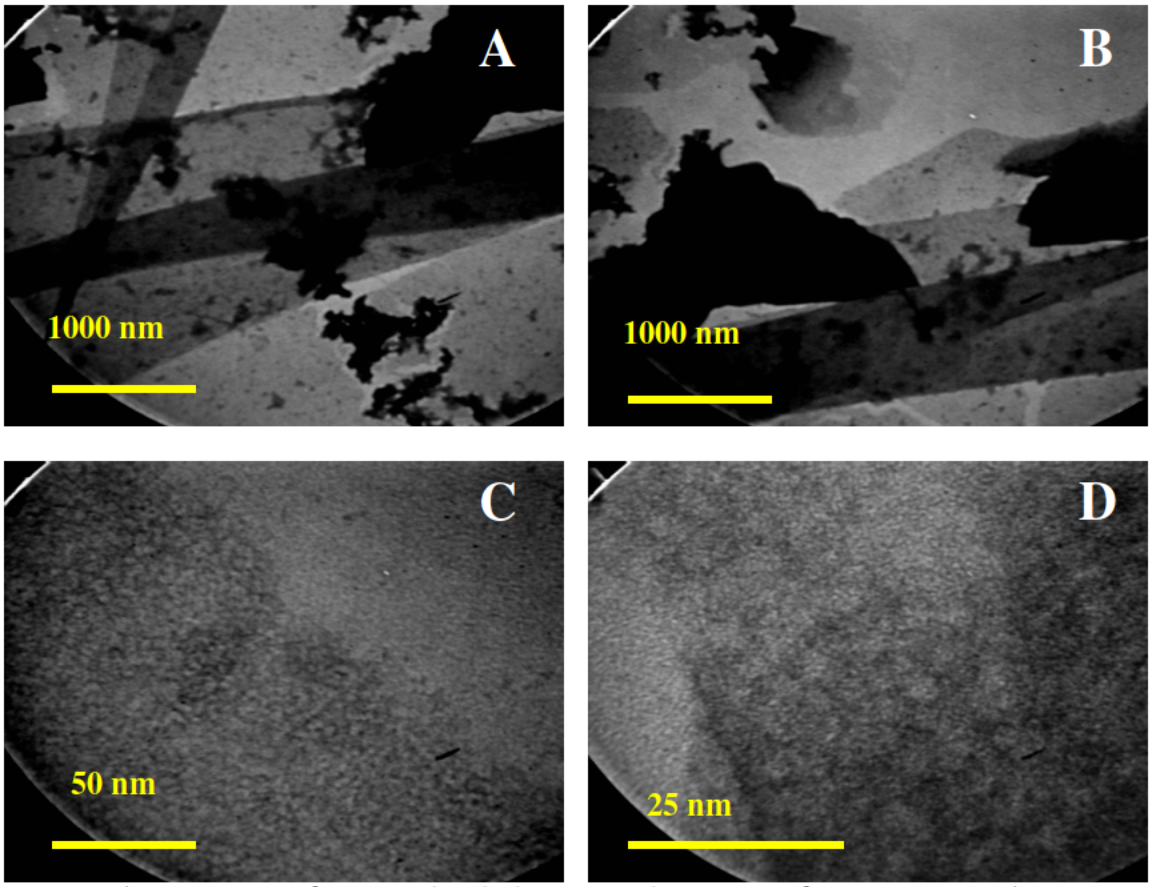

Figure 13 displays a series of micrographs which appear to show a crystal formation. 13A and 13B are taken at 3K magnification; 13C is taken at 55K magnification; while 13D is taken at 160K magnification.

As seen in figure 13, smaller aggregations of GFP and UA are visible among the long triangular like structures. Figure 14 displays a series of such aggregations taken from another sample not previously irradiated before examination.

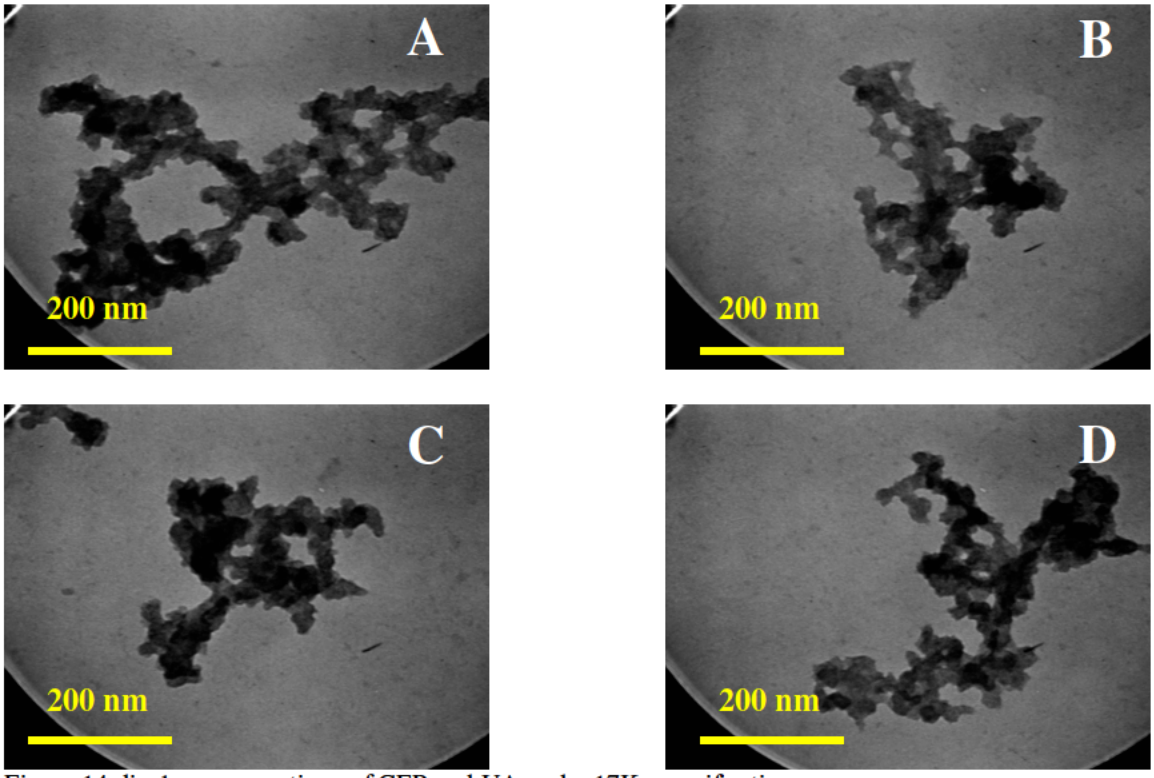

Figure 14 displays aggregations of GFP and UA under 17K magnification.

Figure 15 displays more crystal structures under various magnifications. The sharp angles offer further evidence that the GFP, UA, and buffer salts have aggregated into a co-crystalline complex. Figure 15E displays a fluorescent micrograph of negatively stained GFP in which fluorescing crystals, analogous to those observed in the TEM, are visible.

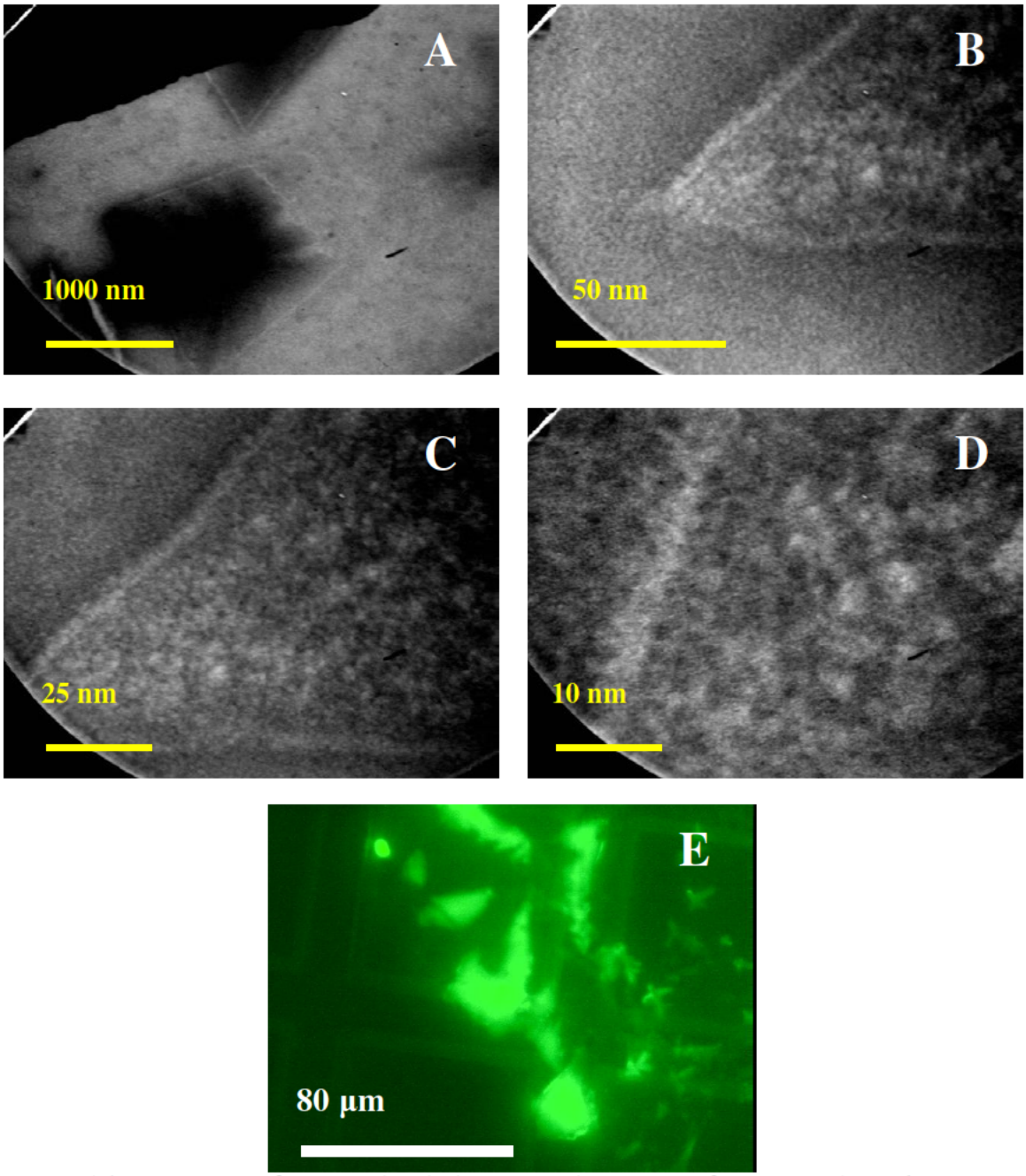

Figure 15 displays a series of micrographs which appear to show a crystal formation. 15A is taken at 3K magnification; 15B is taken at 75K magnification; 15C is taken at 96K magnification; while 15D is taken at 210K magnification. 15E displays a fluorescent micrograph of the negatively stained GFP sample under 40X.

The remaining micrographs in this section are comprised of specimens prepared of a 1:2:1 solution of the pure GFP sample, binding buffer, and 2% UA respectively. The solution was applied to formvar coated grids and allowed to sit as a small bubble until

most of the liquid had evaporated. The grids were then washed three times with the washing buffer and the excess liquid was removed with a wick. This particular preparation produced some of the more stunning examples of crystal formations during the study. As seen by Figure 16, an elaborate arbor pattern emerges from a much larger object that is differentially stained with UA. The highly ordered diffraction patterns produced by this object and others like it are also presented in Figure 16, which offer compelling evidence of their crystalline structure.

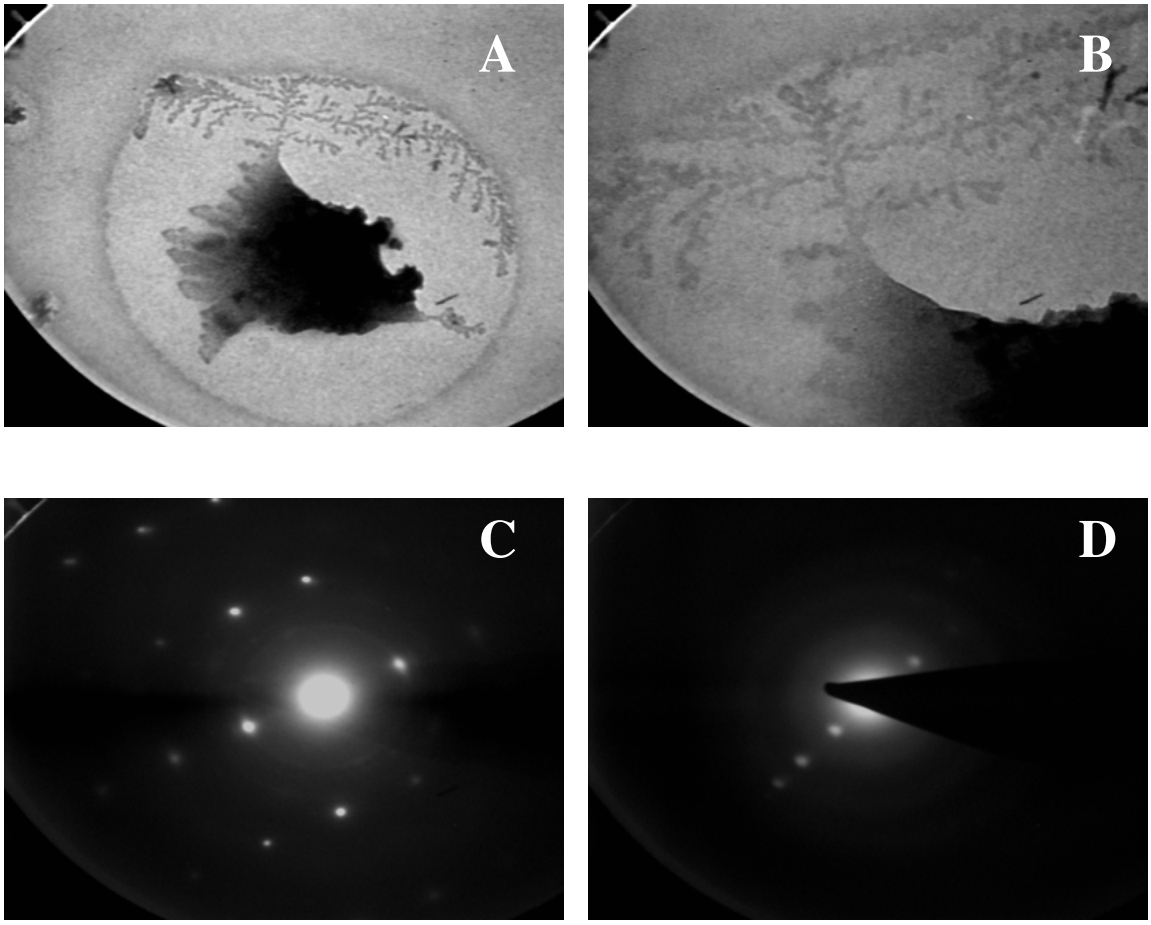

Figures 16A and 16B show an arbor like crystal formation at 3000K and 7500K respectively. Figures 16C and 16D show two diffraction patterns that emerged from the objects taken with a camera length of 122 mm at spot size 5.

Further evidence that these objects constitute crystals is evident in Figure 17, where the edge of one crystal clearly shows many subunits oriented similarly. The tightly packed subunits are poorly stained with UA, therefore negatively affecting contrast. The structure essentially disintegrated after several seconds, even though spot size 5 was used. As the object breaks up, several barrel shaped subunits are visible in Figure 17B as indicated by blue arrows.

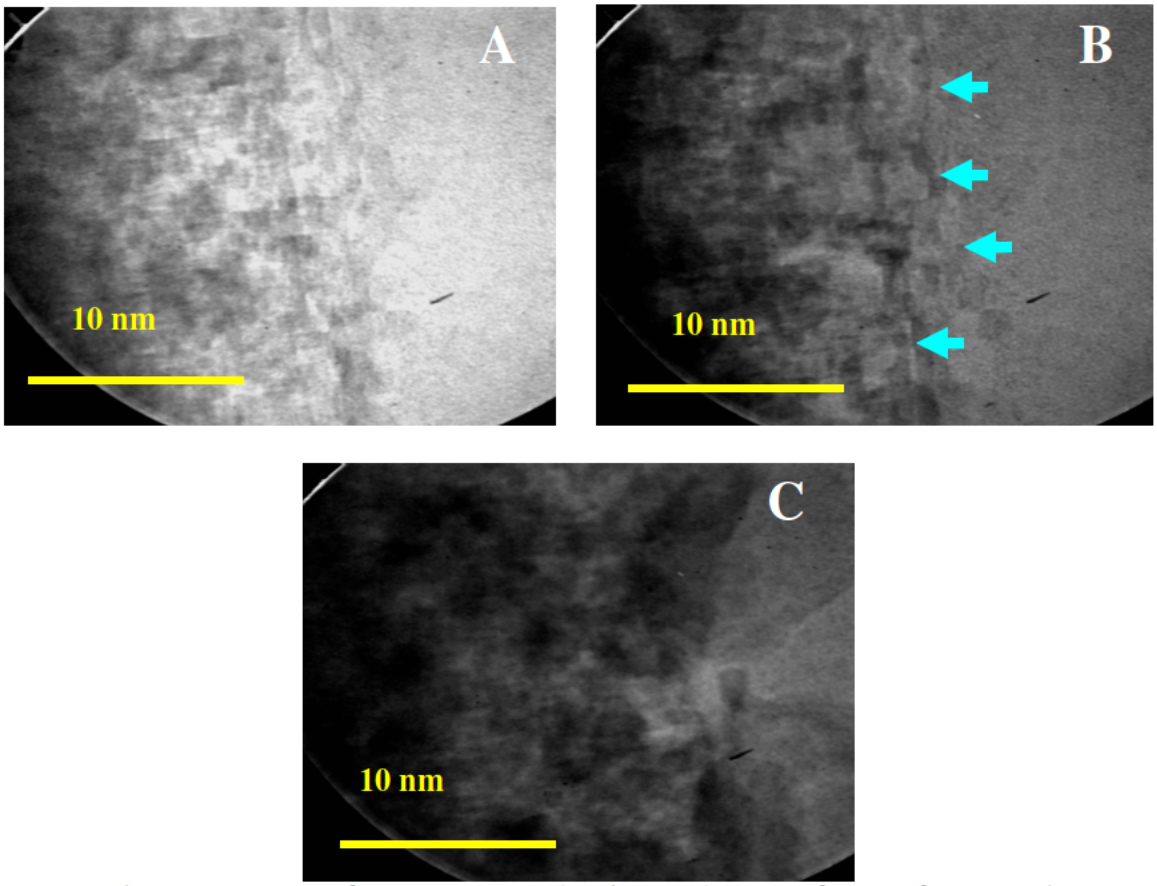

Figure 17 displays a sequence of electron micrographs taken at 450K magnification of a crystal edge as it was destroyed by the electron beam over the course of several seconds. The tightly packed and ordered structure of the object is evident in Figures 17A and 17B.

The diffraction patterns proved difficult to acquire as the more transparent edges of the objects under examination proved sensitive to the electron beam and were easily damaged. Using higher spot sizes reduced the beam exposure somewhat and provided

enough sample stability to acquire some higher magnification images. Figures 18A and 18B show one triangular shaped crystal before and after several seconds of electron beam exposure. Note how the staining of the object is changed as indicated by the pink arrow, suggesting that the UA may have penetrated parts of the crystal structure only after the sample was subjected to the electron beam for several seconds. This brings up the distinct possibility that GFP crystals may have formed in solution before the sample was applied to the formvar coated copper grids. This is not entirely impossible because some GFP samples were stored in refrigeration for several months. The UA would then seem to have settled on top of the crystals, being unable to penetrate their dense packing. As the electron beam disrupted the structure of the crystal, UA may have then penetrated the sample. Interestingly as seen in Figure 18C, the field of view shows both the crystal structure and a less ordered aggregation of the GFP where the UA more completely penetrated. This observation eloquently surmises one finding of this study that the GFP sample, depending on its preparation and even within the same specimen, exhibits varying degrees of structural order and displays unexpected aggregation phenomena. The less ordered aggregations seem to possess greater contrast because of their more comprehensive interaction with the UA. However because crystalline objects possess intrinsic order, resolving the discreet GFP molecules within such formations becomes somewhat simpler. As seen in Figure 18D at high magnification, several objects that approximate the dimensions of the GFP beta-barrel are indicated by blue arrows.

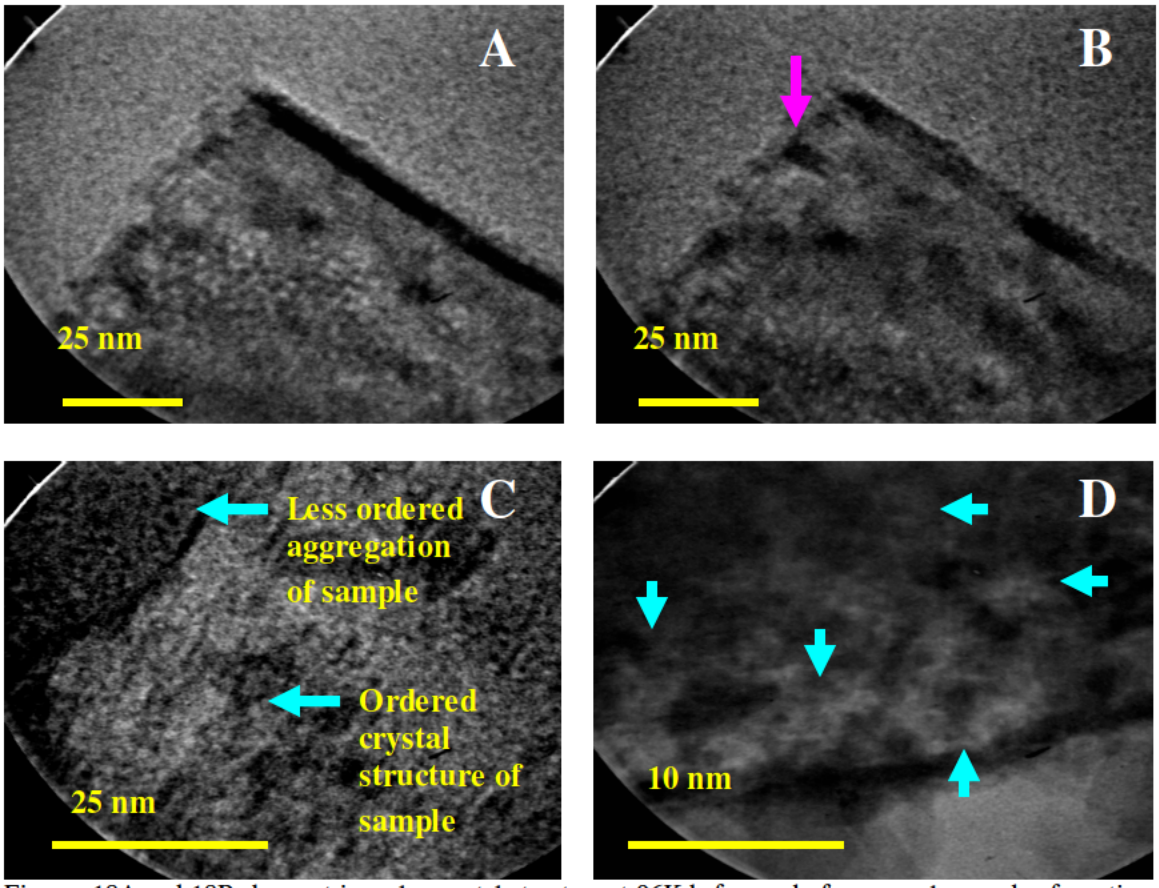

Figures 18A and 18B show a triangular crystal structure at 96K before and after several seconds of scrutiny by the electron beam. Figures 18C and 18D display the same sample, but at 160K and 450K magnifications respectively. Figure 18C is important in that it shows both a crystal and less ordered aggregation of the GFP sample in the same viewing area. Figure 18D shows the edge of one crystal formation.

Arrangements of GFP molecules with less ordered structures result in the discreet proteins being positioned in many different orientations. As illustrated in Figure 19, higher magnification images of aggregations show many objects whose dimensions fit those of the discreet GFP molecule. Figure 19A is representative of many samples presented in this study which likely constitute aggregations of the sample, but lack enough order to conclusively determine which objects correspond to the discreet protein. Many motifs are present including fine lines, some parallel, and even what appears to be a 'doughnut' with a central pore. Blue arrows indicate several examples of such motifs. It is possible that this particular recurring aggregation presents the GFP molecules in

many different orientations and to varying degrees of intactness. Figures 19B through 19D possess a slightly more organized aggregation phenomenon. Here suspected 3 by 4 nm GFP molecules are indicated by yellow circles.

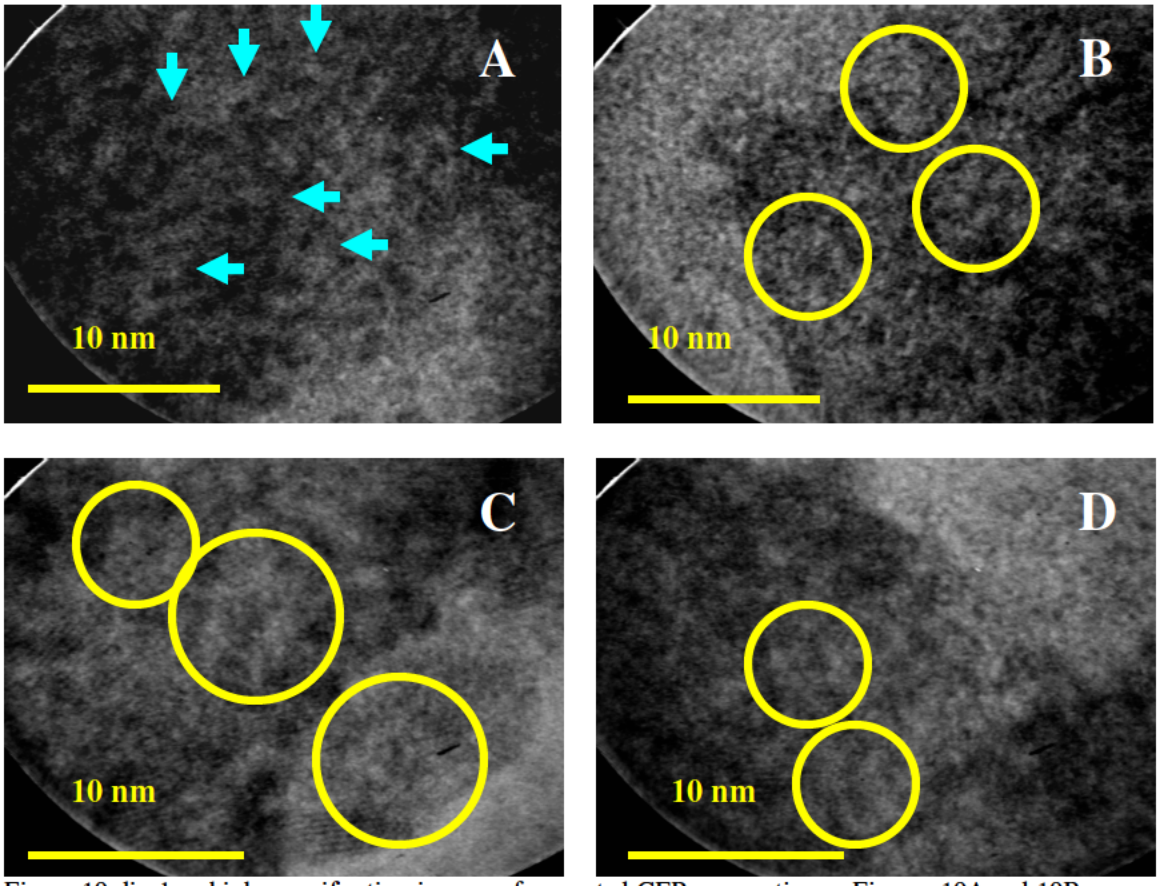

Figure 19 displays high magnification images of suspected GFP aggregations. Figures 19A and 19B are taken at 350K magnification, while Figures 19C and 19D are taken at 450K magnification.

Resolution of a Discrete GFP Protein Monolayer

For some specimens large aggregations with self similar properties were observed which when examined under high magnification yielded what appeared to be highly ordered assemblies of objects that approximate the dimensions of the discrete GFP protein. These large aggregations took two forms. The first as seen in Figure 20 consisted of unusually well maintained aggregations similar to those crystal formations observed in Figures 13

and 15. While the center of aggregations revealed larger objects, those objects towards the periphery become progressively smaller until the edge of the aggregation phenomenon is reached, where the smallest units are found. Figures 20E and 20F present high resolution images of the aggregation edge. The units are approximately 3 by 4 nm, which constitutes the dimensions of the GFP molecule, and are suspected to have organized into a monolayer whose edge, due to its relative transparency, is more easily resolved by the electron microscope.

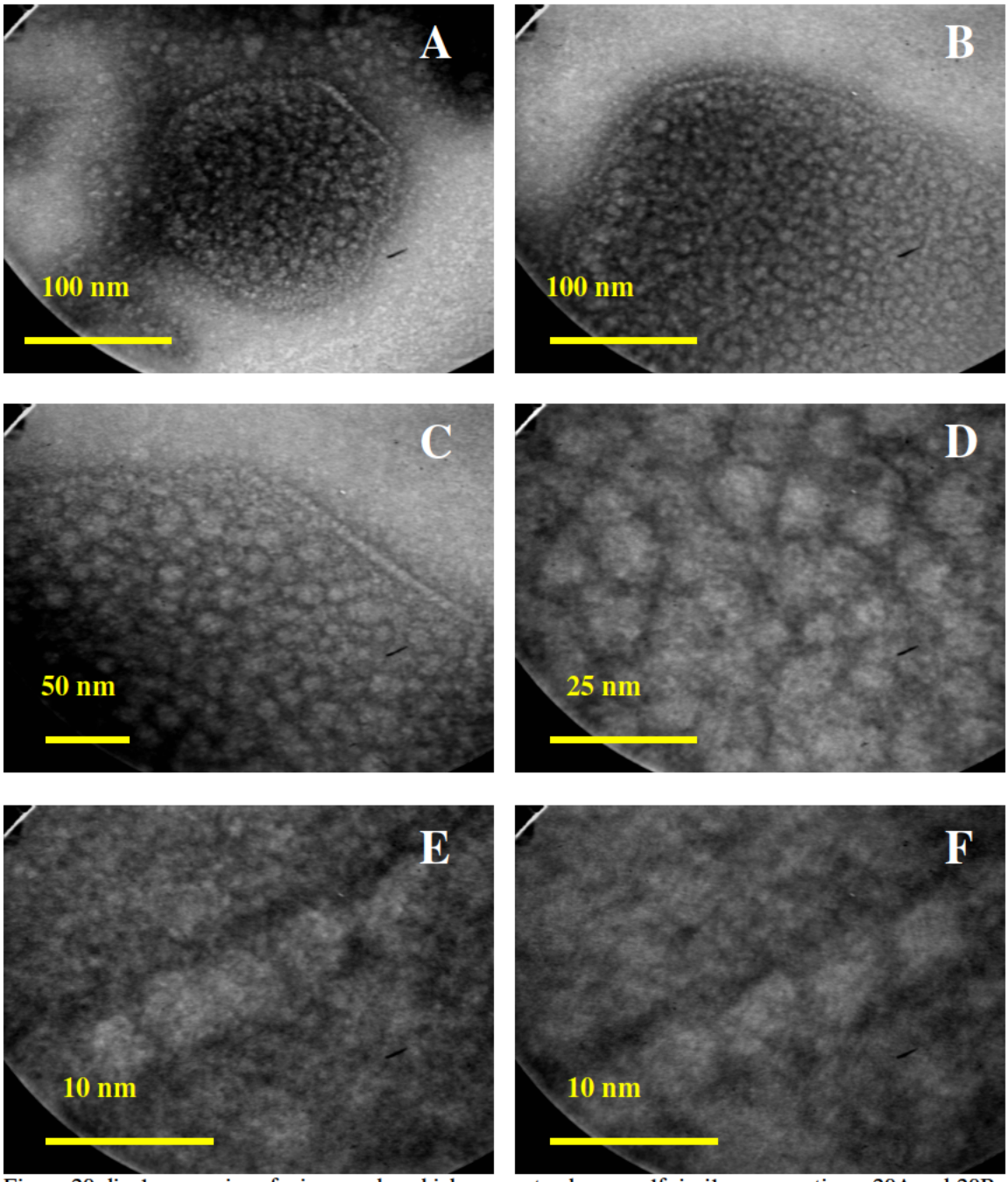

Figure 20 displays a series of micrographs which appear to show a self similar aggregation. 20A and 20B are taken at 27500 magnification; 20C is taken at 45K magnification; 20D is taken at 124K magnification; while 20E and 20F are taken at 350K magnification.

Figure 21 shows another aggregation at various magnifications similar to the one imaged in Figure 20. Along the edge of the aggregation, what appears to be the distinct protein is resolved.

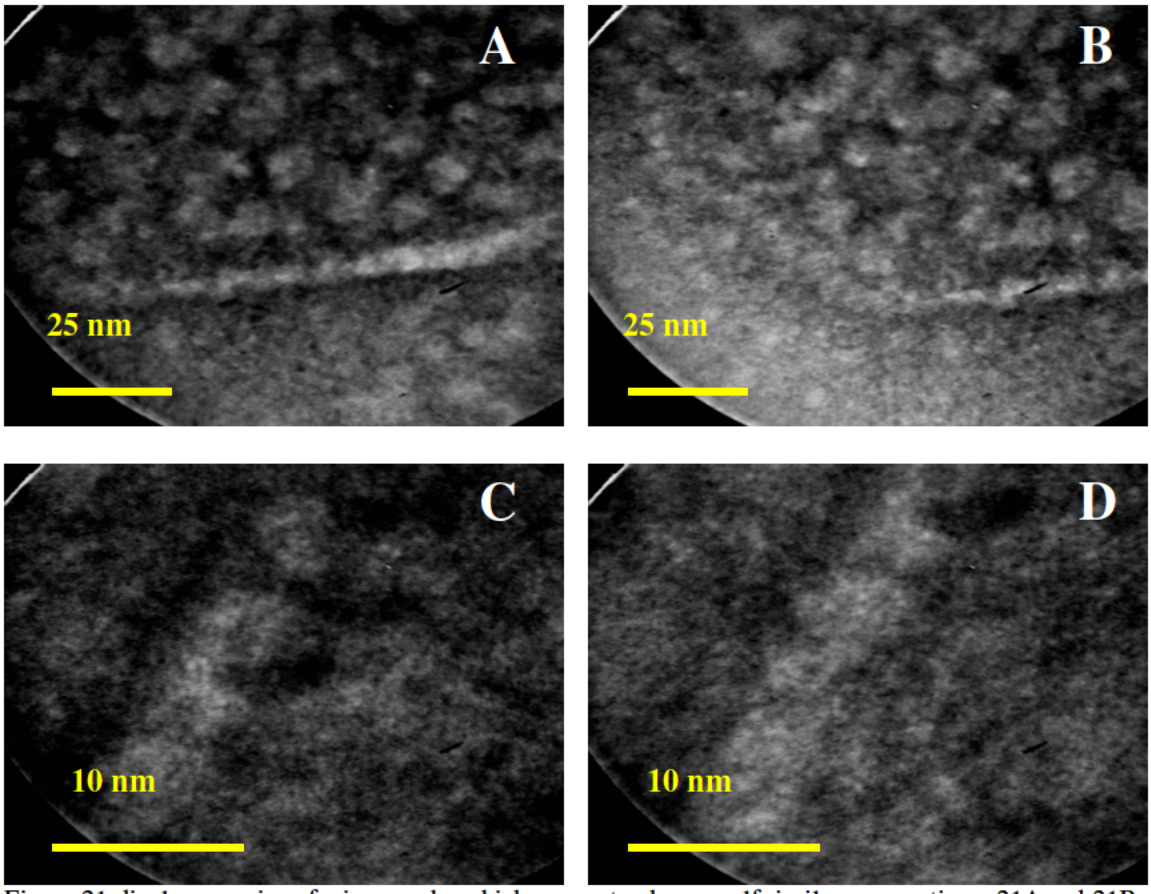

Figure 21 displays a series of micrographs which appear to show a self similar aggregation. 21A and 21B are taken at 96K magnification; while 21C and 21D are taken at 350K magnification.

The second structure presented in this section consisted of long folds that superficially resemble the edges of the aggregation phenomenon observed in Figures 20 and 21. These folds consisted solely of a sequences of what may constitute the discrete protein surrounded by amorphous material. The following images were taken from the same specimen as Figure 13 and were thus thoroughly irradiated with the electron beam before examination. Figures 22 and 23 display these folds, which were found among the large

crystal formations observed in Figures 13A and 13B. The high resolution images of the folds do not show the suspected GFP as clearly as those observed in Figures 20 and 21, perhaps as a result of the additional electron beam exposure.

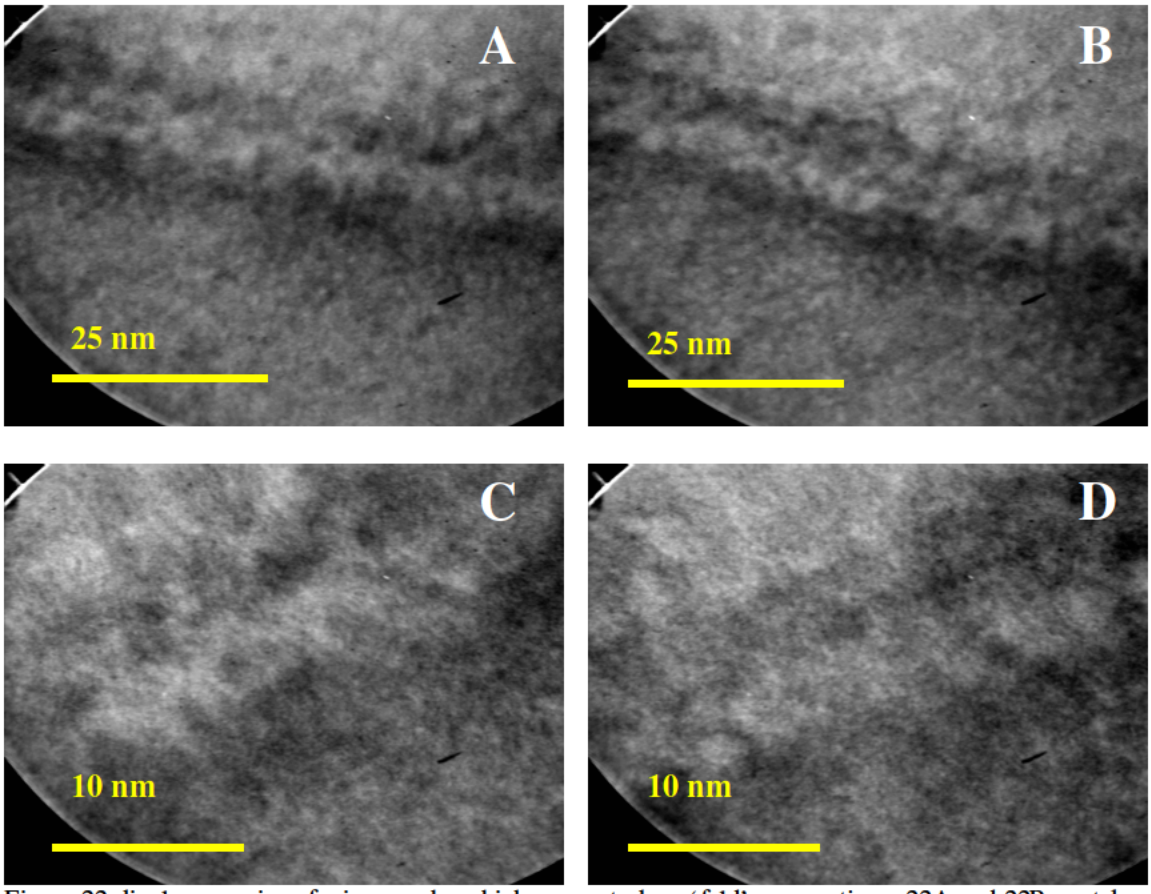

Figure 22 displays a series of micrographs which appear to be a 'fold' aggregation. 22A and 22B are taken at 160K magnification; while 22C and 22D are taken at 350K magnification.

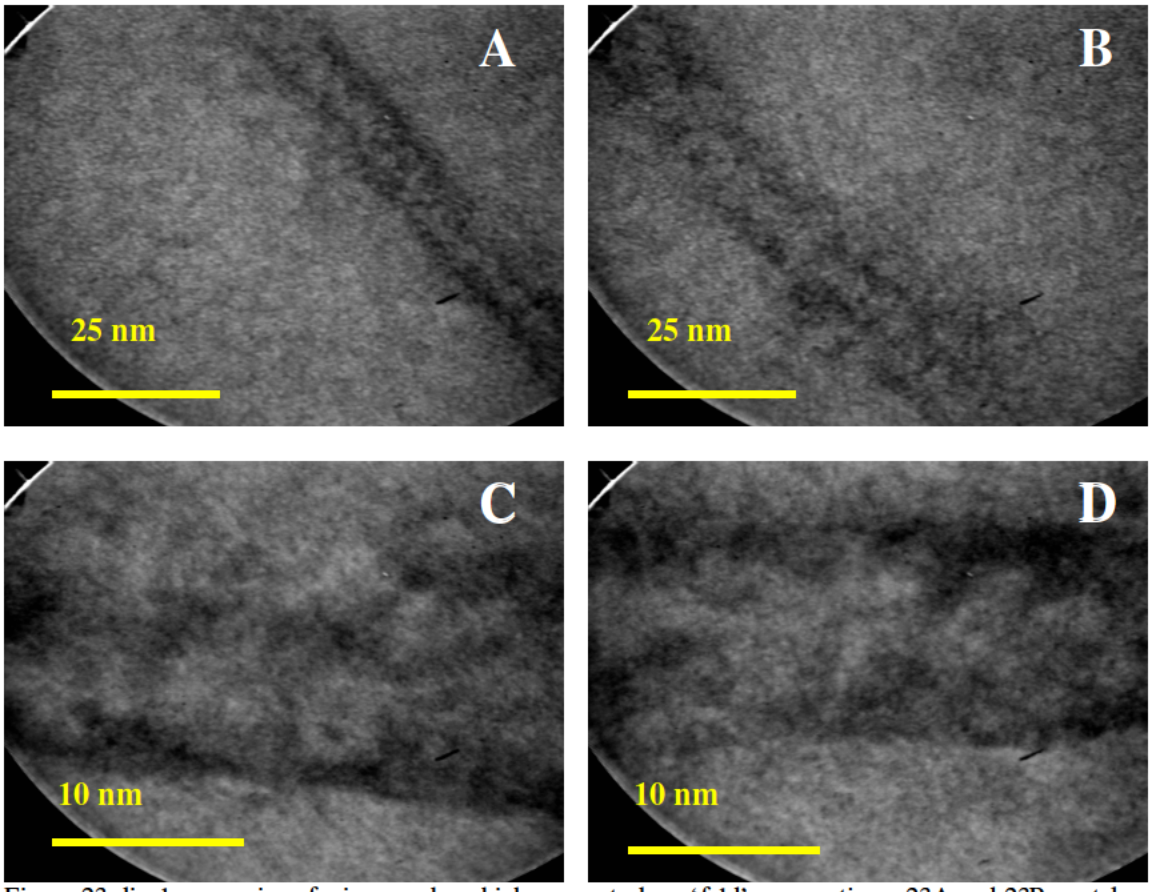

Figure 23 displays a series of micrographs which appear to be a 'fold' aggregation. 23A and 23B are taken at 124K magnification; while 23C and 23D are taken at 350K magnification.

Intermediate and High Resolution Images of the GFP / Uranyl Acetate Aggregations

First it is noteworthy to point out that the imaged objects are indeed formed by the sample. In many cases the vacant formvar and aggregations have been imaged within the same electron micrograph. For many micrograph in a series it is possible to distinguish between the sample and the blank formvar. While this observation alone might not appear to be profound, distinguishing between the sample and the formvar background was initially of great consequence to this project. Working at high magnifications, without the aid of context or a clear understanding of what the image should look like, can infuse doubt into the results. However as seen in Figure 24, control studies were preformed with blank and negatively stained formvar. These preparations did not

produce the unique aggregations that resulted from the negatively stained GFP samples and in fact appeared to be void of any material.

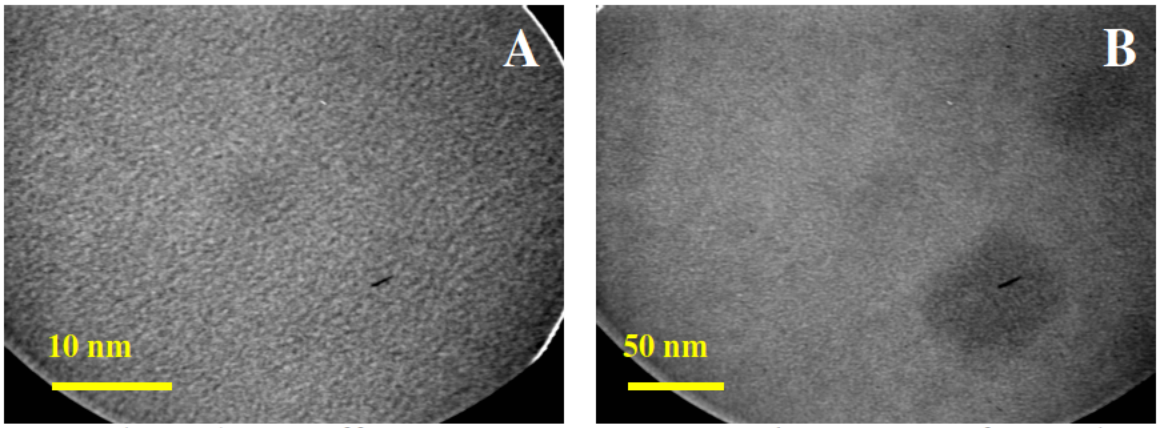

Figure 24 displays the results of formvar control experiments. 24A is taken at 210K magnification and represents unstained formvar at a high magnification. 24B is taken at 45K magnification and represents negatively stained formvar.

As observed in Figure 13, GFP negatively stained with uranyl acetate (UA) is deposited on formvar coated copper grids in what appears to be crystal formations and well defined aggregates. It is speculated that these aggregations form as the liquid sample dries, thus leaving behind a solid and perhaps crystalline accumulation of GFP and UA. While these structures might superficially appear to be amorphous, recurring forms and motifs are evident and have been pointed out where instructive. The following electron micrographs examine these structures at increasing magnifications.

The first sample in our series, Figure 25, was prepared slightly differently that the others. The copper grid was first treated with Triton, a surfactant, followed by an undiluted quantity of GFP which was permitted to sit for one minute and then removed by drawing off the excess liquid with paper. A 0.5% solution of UA was then applied and allowed to sit for 15 seconds, then removed in a similar fashion. Figure 25 displays the typical appearance of the GFP/UA aggregates. Note that the aggregates have similar repeating

structures, indicted by blue arrows, embedded in the more heavily stained background. These objects, too large to be the discrete protein, may be units of GFP that have assembled into ordered arrangements. Some resemble a 'doughnut.'

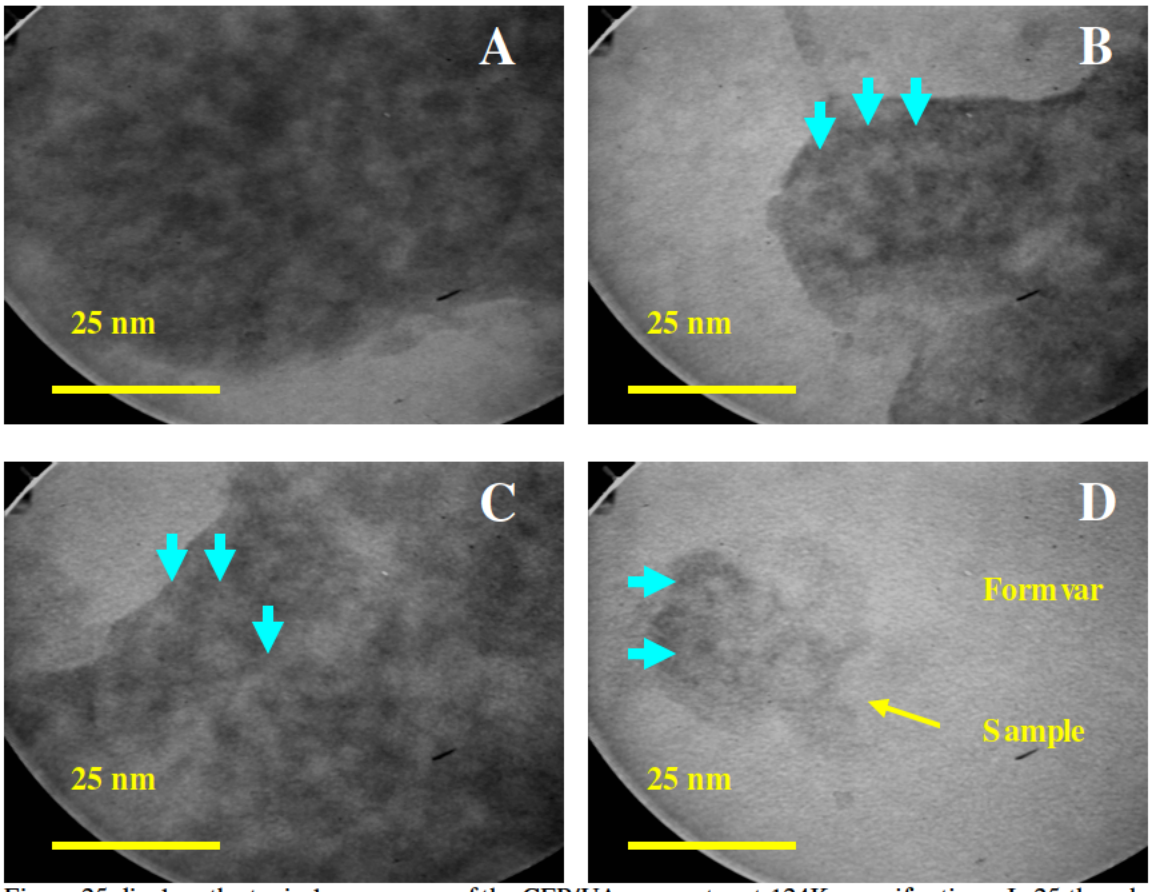

Figure 25 displays the typical appearance of the GFP/UA aggregates at 124K magnification. In 25 though 25, the vacant formvar is visible adjacent to the sample.

Figure 26 displays the same sample that was imaged in Figure 13. Despite being irradiated by the electron beam, measured at 10.7 pico ammeters, for a minute and a half the aggregates remain fairly intact and closely resemble those structures observed in Figure 25, though the additional electron beam exposure seems to have resulted in a more amorphous condition.

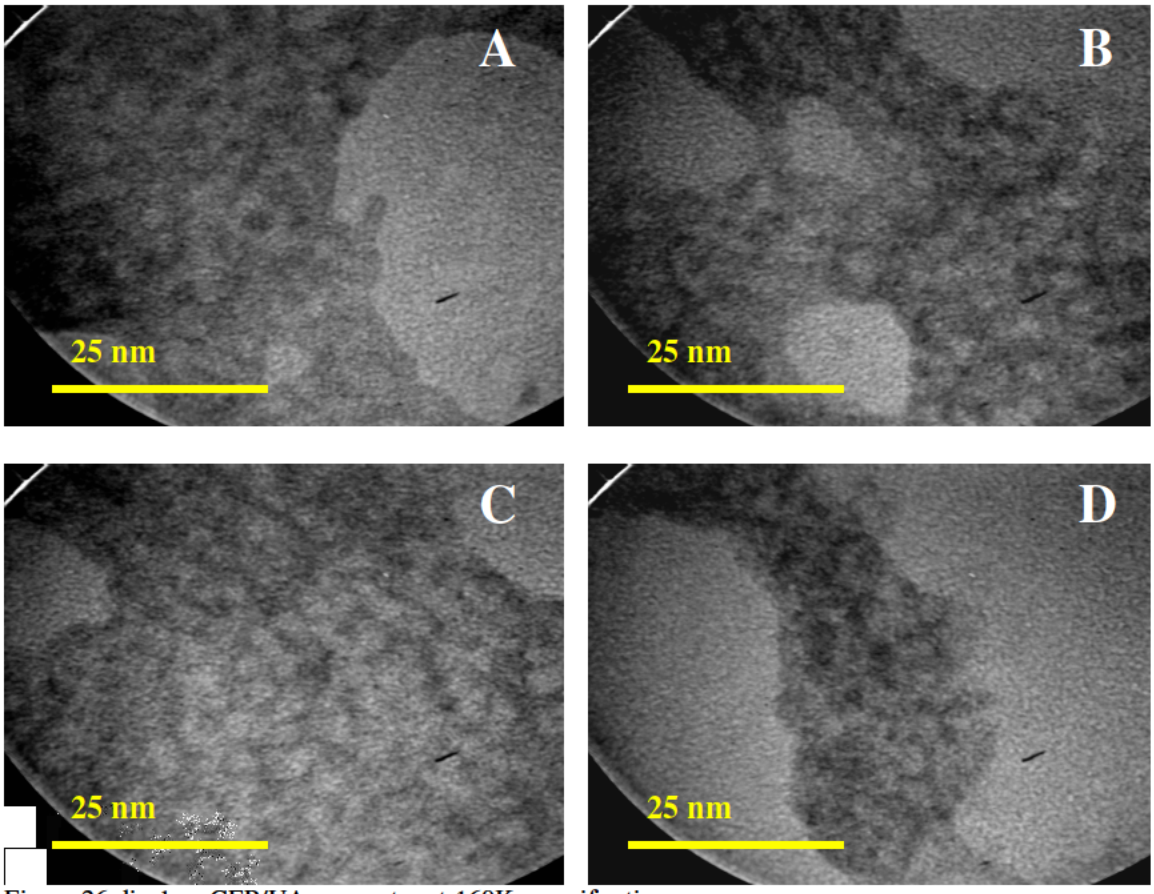

Figure 26 displays GFP/UA aggregates at 160K magnification.

Figure 27 is unique in that it was prepared in a similar manner to Figure 13, but not subjected to the electron beam before examination. Only spot sizes three and five were used to examine the specimen. Thus the area of electron exposure was small, approximately equal to the area of the image. The electron beam that bombarded the sample likely never exceeded 1 pico ammeter. As seen in figure 27, the structures within the aggregate are similar to those observed in Figure 26, but they appear to be slightly more intact. The smaller spot size also reduced charging and specimen drift which aided in resolving the images. The last micrograph in the series shows a section of the specimen that is apparently blank and thus represents negatively stained formvar. Various objects, indicated by blue arrows and yellow circles, point to what may

constitute the discrete protein. Interestingly, some of the objects arrange themselves around a central pore creating a 'doughnut.' Somewhat larger barrel shaped objects, indicated by yellow circles, are also visible.

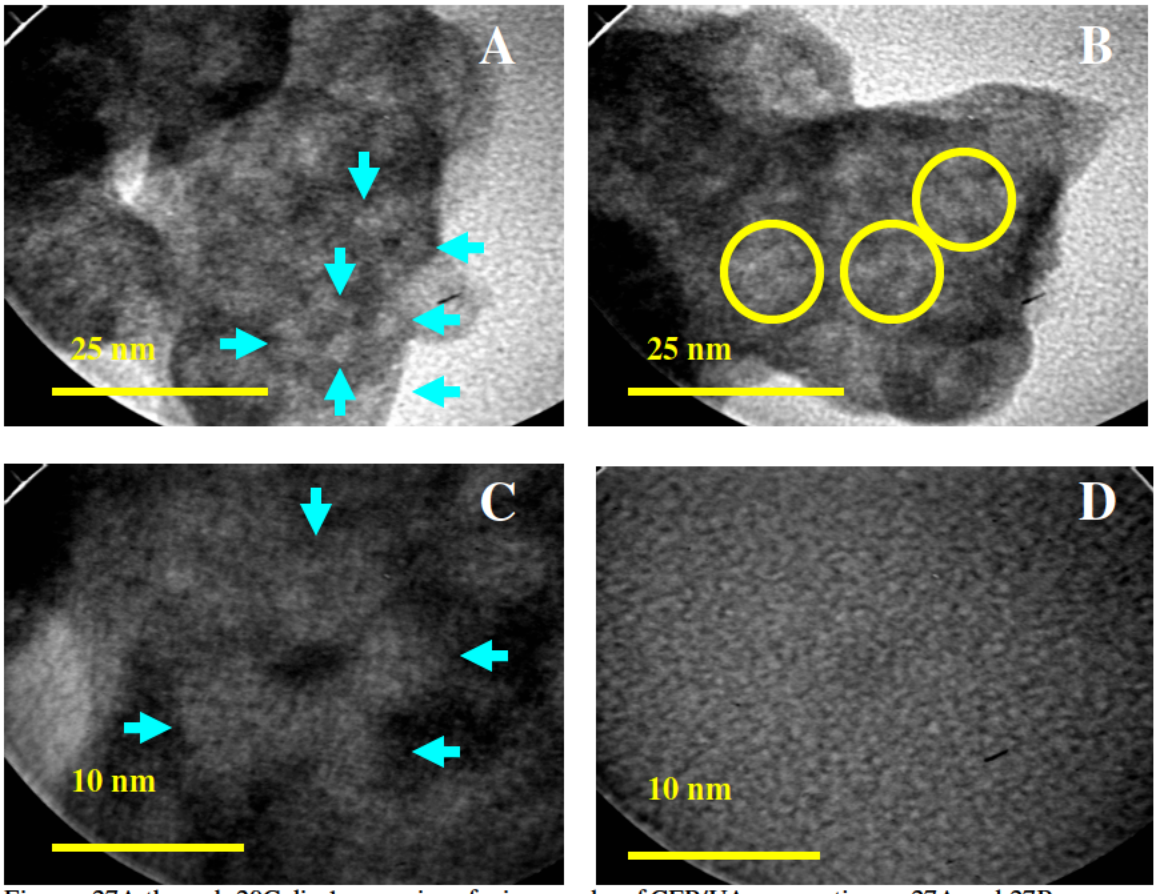

Figures 27A through 20C display a series of micrographs of GFP/UA aggregations. 27A and 27B are taken at 160K magnification; 27C is taken at 350K magnification; while 27D is taken at 350K magnification and shows a section of the specimen that is blank with no sample.

Figure 28 displays an enlarged micrograph of Figure 27C at 350K magnification. At this magnification, evidence of secondary protein structure becomes apparent in the form of fine lines. Fine lines conceivably represent the polypeptide chain of the proteins. Blue arrows point to objects which approximate the dimensions of GFP. The objects, which appear to form around a central pore, may be an ordered arrangement of GFP that has

assembled into some polygon structure. The pink arrow points to a series of perpendicular lines that perhaps correspond to the beta strands of a beta-barrel.

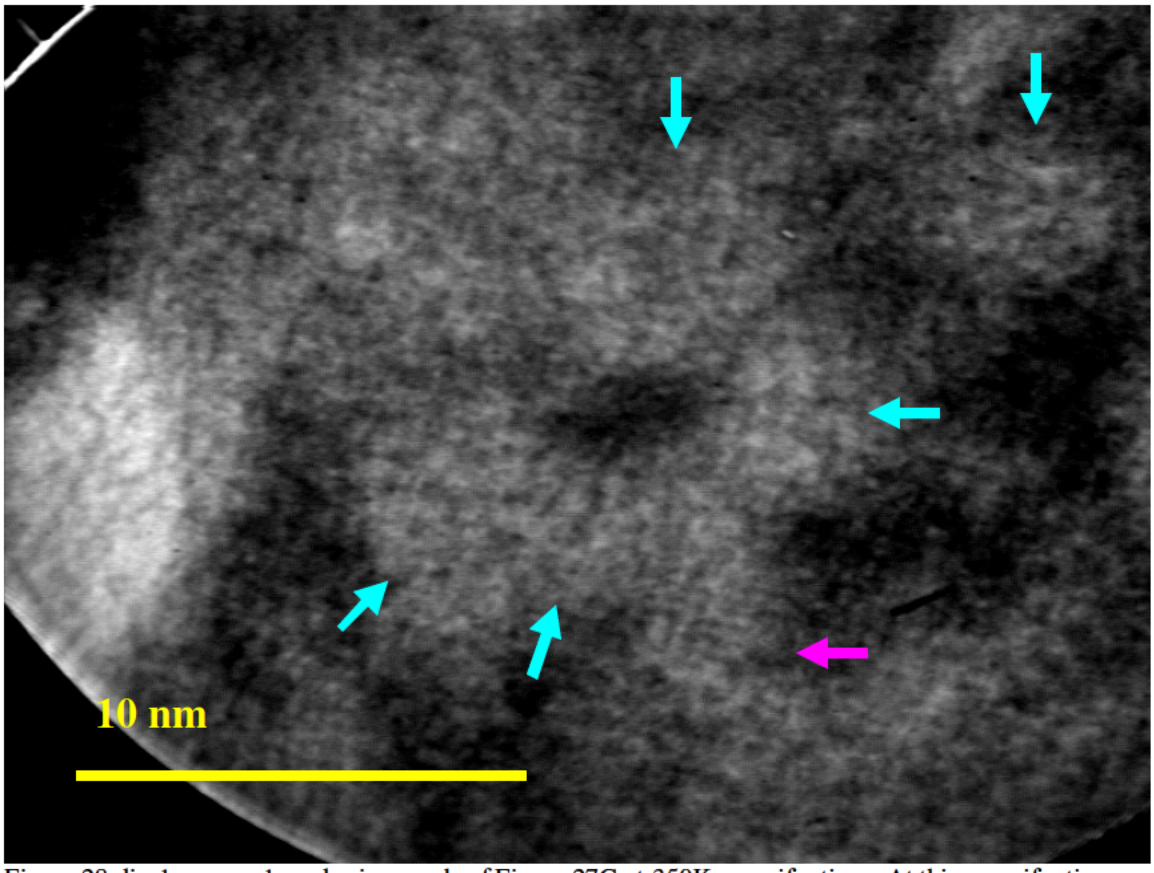

Figure 28 displays an enlarged micrograph of Figure 27C at 350K magnification. At this magnification, evidence of secondary protein structure (pink arrow) becomes apparent.

At high magnifications, the GFP/UA aggregations exhibit clear delineations of low and high electron density possibly representative of the GFP protein. Figures 29 and 30 were imaged from the same small aggregations observed in Figure 14. Figure 29 displays three series of images, 29A-29B and 29C-29D at 350K magnification and 29E and 29F at 450K respectively. The first of each series is in focus, while the second is over focused to increase contrast with markers provided. What appear to be 'doughnuts' (marked by blue arrows) and parallel lines which in some cases resemble a barrel (marked by a

yellow circle) are evident. Figure 30 displays images exhibiting similar repetitive structures at 450K magnification.

Altogether, Figures 29 and 30 show two recurring structures – a circle approximately 5 nm in diameter and parallel lines whose length and width approach the 3 by 4 nm dimensions of the GFP beta-barrel. These items may in fact be the same formation, but from different perspectives. The 'doughnut' might conceivably be the beta-barrel exhibiting its small axis, while the 3 by 4 nm rectangular structures might represent the long axis of the cylinder. Also of interest are the many right angles observed in the figures.

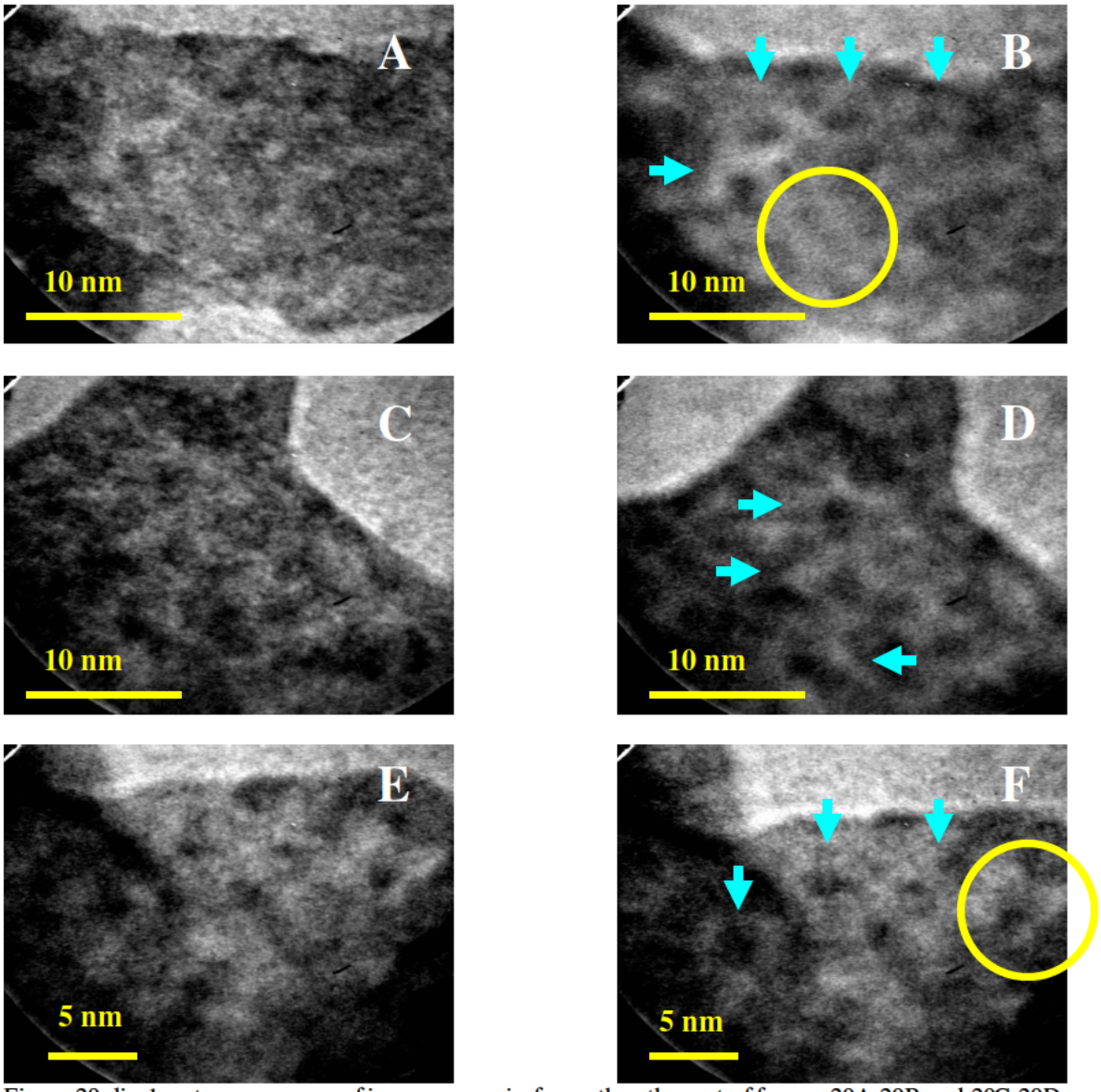

Figure 29 displays two sequences of images – one in focus, the other out of focus. 29A-29B and 29C-29D are taken at 350K magnification; while 29E-29F are taken at 450K magnification.

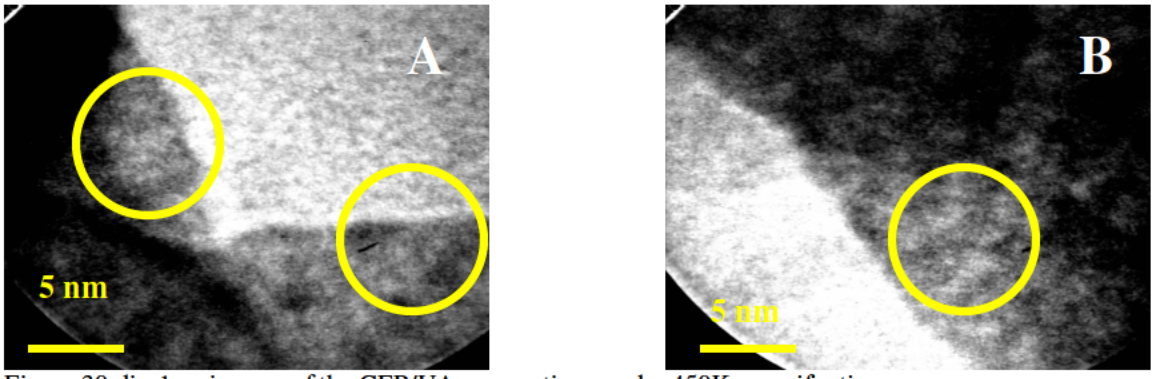

Figure 30 displays images of the GFP/UA aggregations under 450K magnification.

Figures 31 and 32 are a continuation of the specimen presented Figure 27, which was unique because only spot sizes three and five were used to examine the sample. Thus the area of electron exposure was small and the intensity likely never exceeded 1 pico ammeter. Numerous objects that approximate the beta-barrel dimension of GFP are visible; blue arrows and yellow circles point to areas of interest. The pink arrows in Figure 32 indicate the 'doughnut' motif or what is speculated to be an ordered arrangement of GFP that has assembled into some polygon complex.

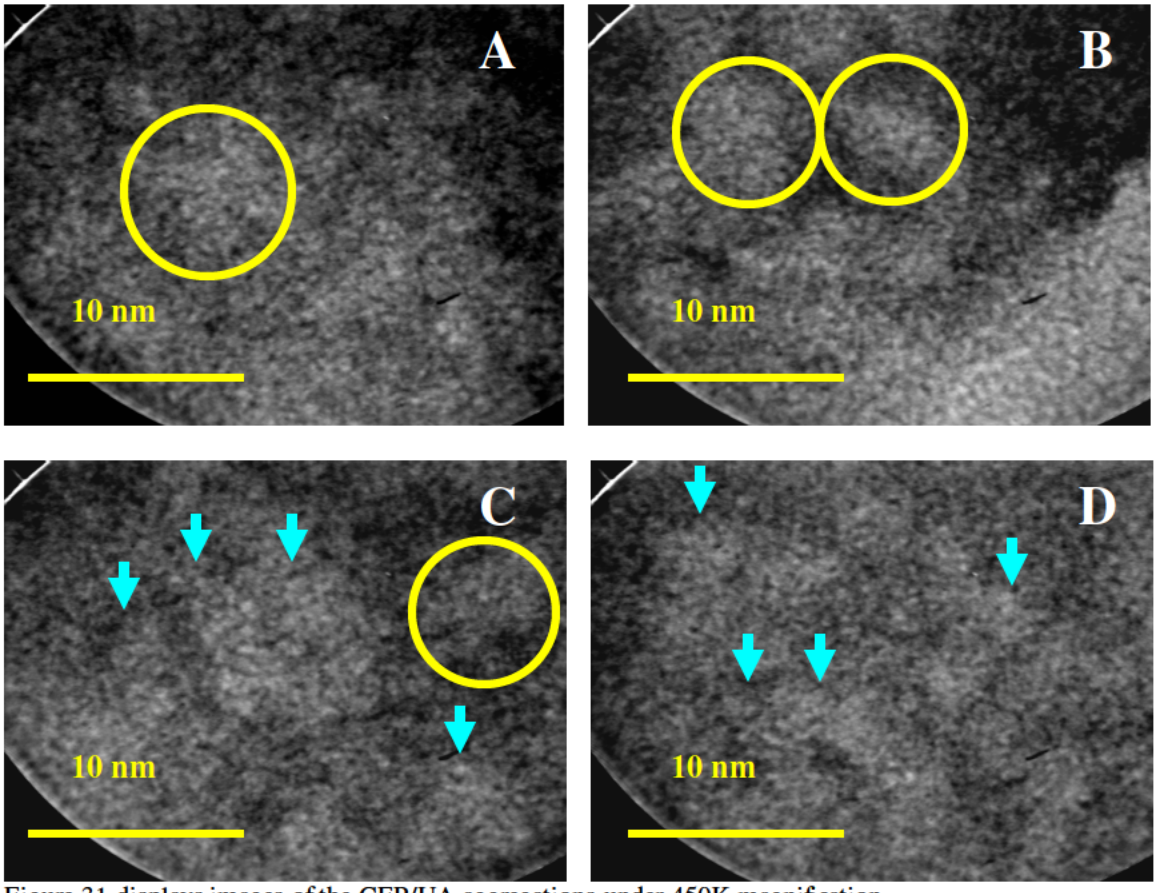

Figure 31 displays images of the GFP/UA aggregations under 450K magnification.

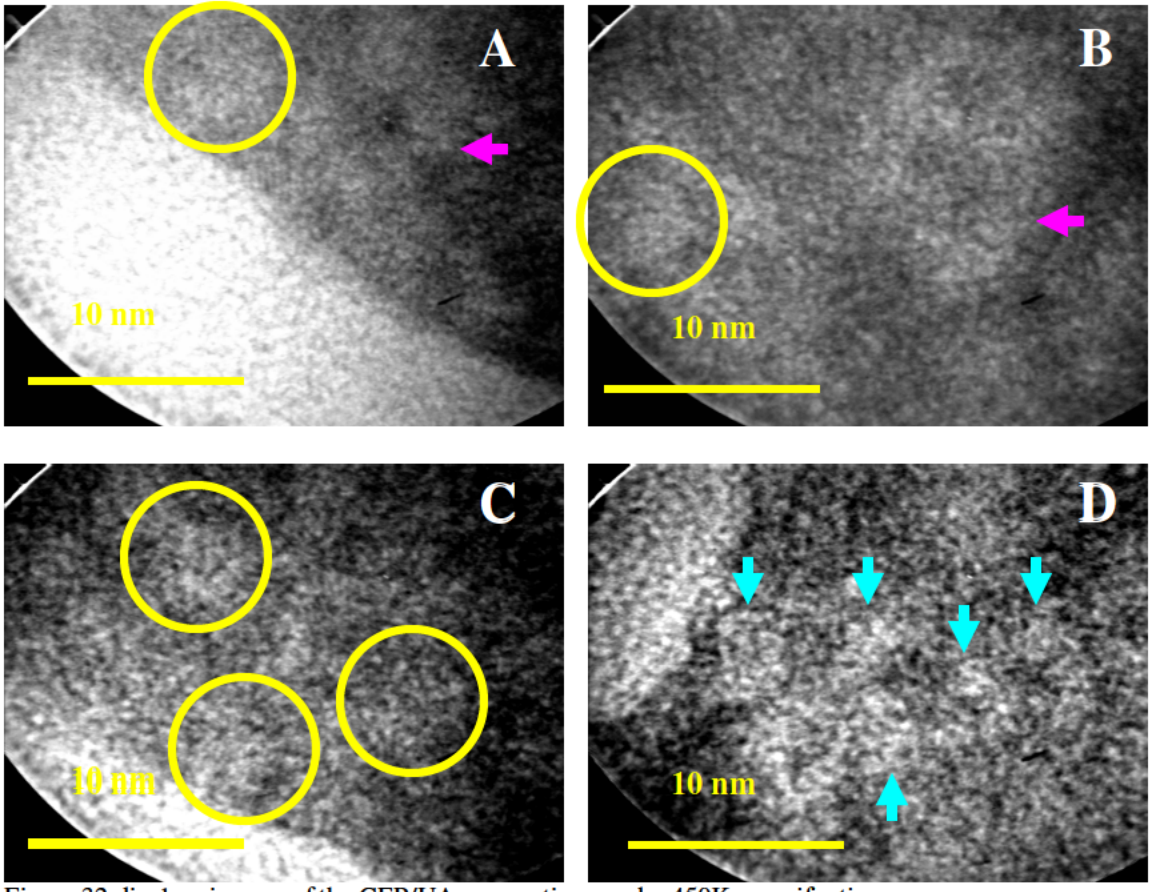

Figure 32 displays images of the GFP/UA aggregations under 450K magnification.

Evidence of Secondary Protein Structure

Figures 34 through 36, taken at 450K magnification, have been enlarged to appreciate what may be evidence of secondary protein structure. Numerous fine lines, some parallel, are suggestive of what may indicate alpha helices or beta sheets. Figure 33, rendered through MDL Chime, offers a brief review of the GFP secondary structure, with the color gold representing extended beta sheets and the color pink representing alpha helices.

It is also worth reviewing idealized protein secondary structures. For a polypeptide chain in an idealized extended chain, the repeat between identically oriented R-groups is 7.0 Å, with 3.5 Å per amino acid, matching the fiber diffraction data for beta-keratins. An alpha

helix has a diameter of about 5-6 Å (0.5-0.6 nm), not counting the side chains - these might add another 3-4 Å of diameter. The repeat unit for an alpha helix is 5.4 Å, with 3.6 amino acids per turn of the helix. A single beta strand is about 4-5 Å wide, so a flat, extended beta sheet of 5 strands would be about 20-25 Å wide.

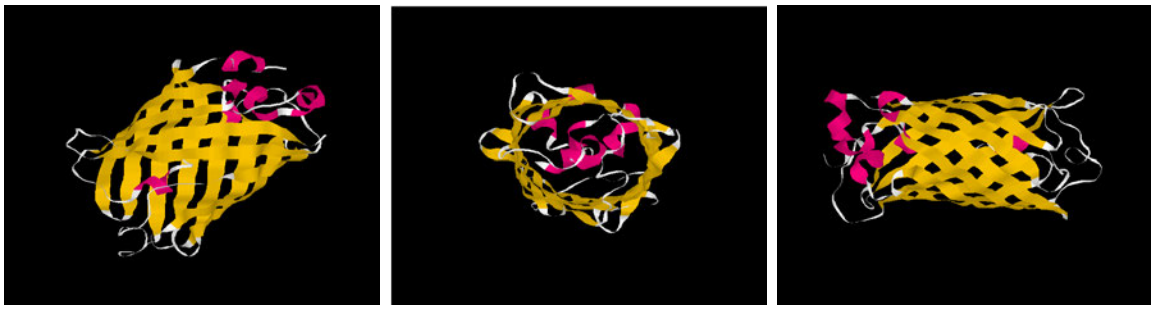

Figure 33, rendered through MDL Chime, displays the GFP beta-barrel at several different orientations. The native 27 kDa protein consists of 238 amino acid residues in a single polypeptide that forms an 11 stranded Beta-barrel, with approximate dimensions of 3 by 4 nanometers. A single alpha helix within the center of the beta-barrel contains the fluorophore which is responsible for the protein's fluorescence.

In Figures 34 through 36, blue arrows are used to indicate exquisite examples of fine lines where the UA has deposited in such a way as to suggest the presence of a periodic sequence. Because the periodicity of units in the indicated lines is less than 1 nm, it is possible that such strands represent polypeptide chains. Each point may represent an amino acid residue. These lines or chains in some respects resemble beads on a necklace. Alternatively, the larger lines may represent alpha helices with their periodic units being turns. Blue dashes, running perpendicular to their targets of interests, are used to indicate examples of parallel lines which are speculated to be either epitaxially deposited uranium lattices or real protein structure such as parallel beta sheets. The beam induces uranium atoms to migrate and form a monoatomic crystal (Kondo and Brown, 2003). The observation of uranium lattices confirms that the microscope is operating at the high resolution transmission electron microscopy (HRTEM) level. Uranium aggregates with

itself but is epitaxially deposited. The growth of the crystal is unique depending on where it is seeded and which organized structure it first associates with (Brown and Barnes, 2007). However the uranium would seem to be associated with the GFP such that the appearance of epitaxially deposited uranium identifies or covers up protein structures. In Figure 34, which is an enlarged image of Figure 31A, pink arrows point to what may be alpha helices on the top side of the beta-barrel. The may also be the Histidine tag which might conceivably bind deferentially to uranium (Hyatt, 2000). The large square shaped object below approximates the dimensions of GFP. Note how the fine lines indicated by the pink arrows appear to turn and make loops. Because the fine lines and parallel lines observed in Figures 34 through 36 occur in multiple directions, the possibility that these phenomena are merely the result of poor stigmation control is discredited.

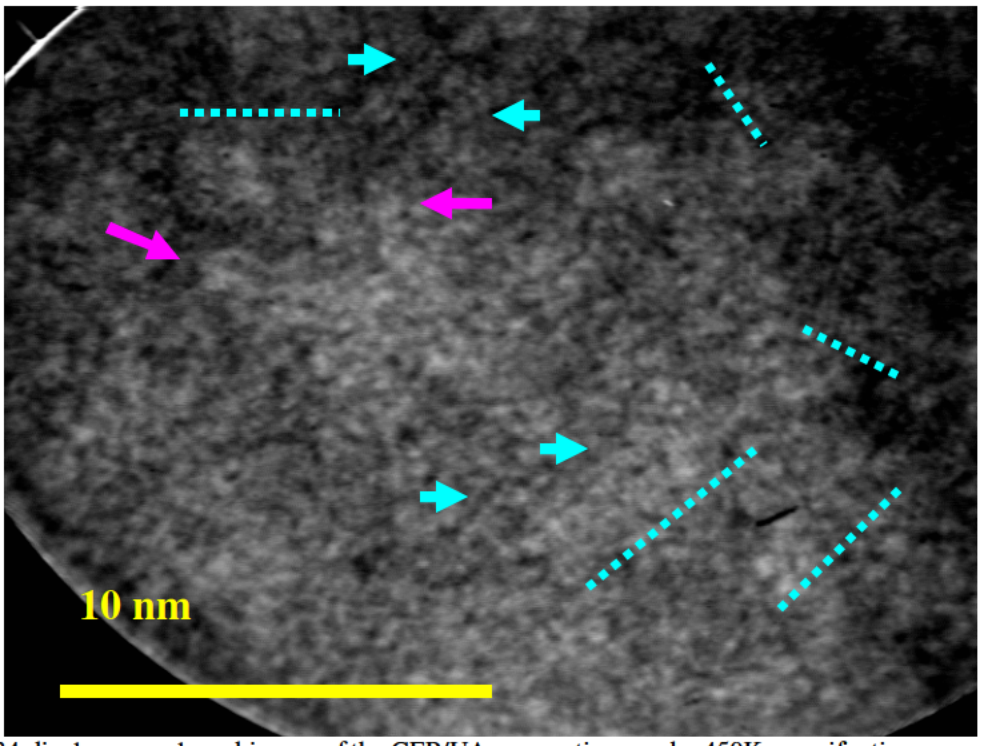

Figure 34 displays an enlarged image of the GFP/UA aggregations under 450K magnification.

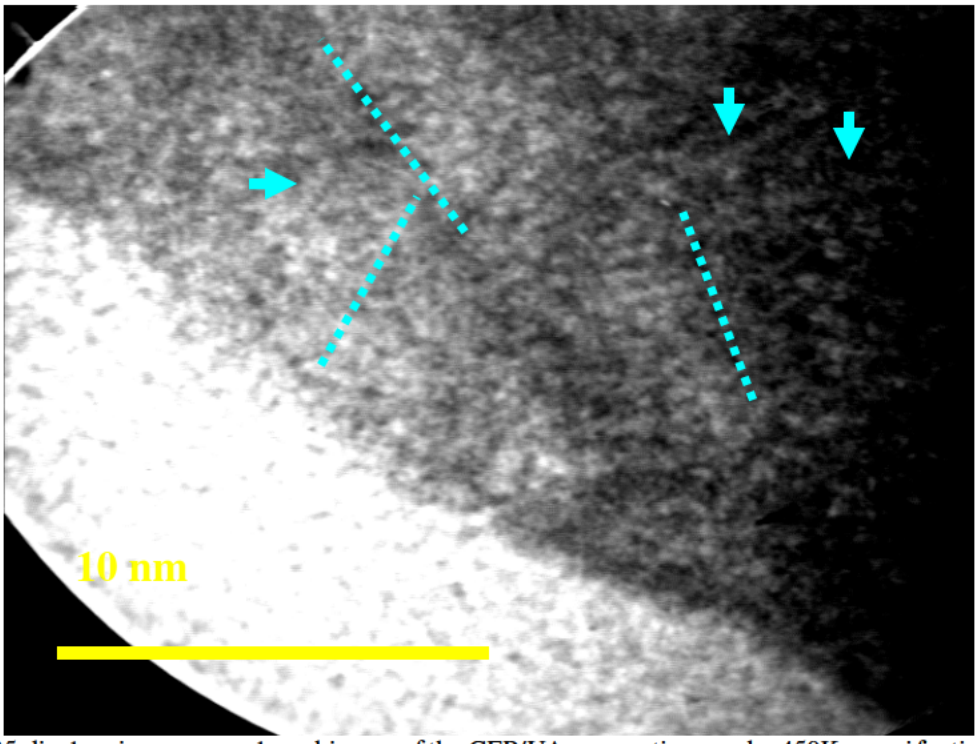

Figure 35 displays images an enlarged image of the GFP/UA aggregations under 450K magnification.

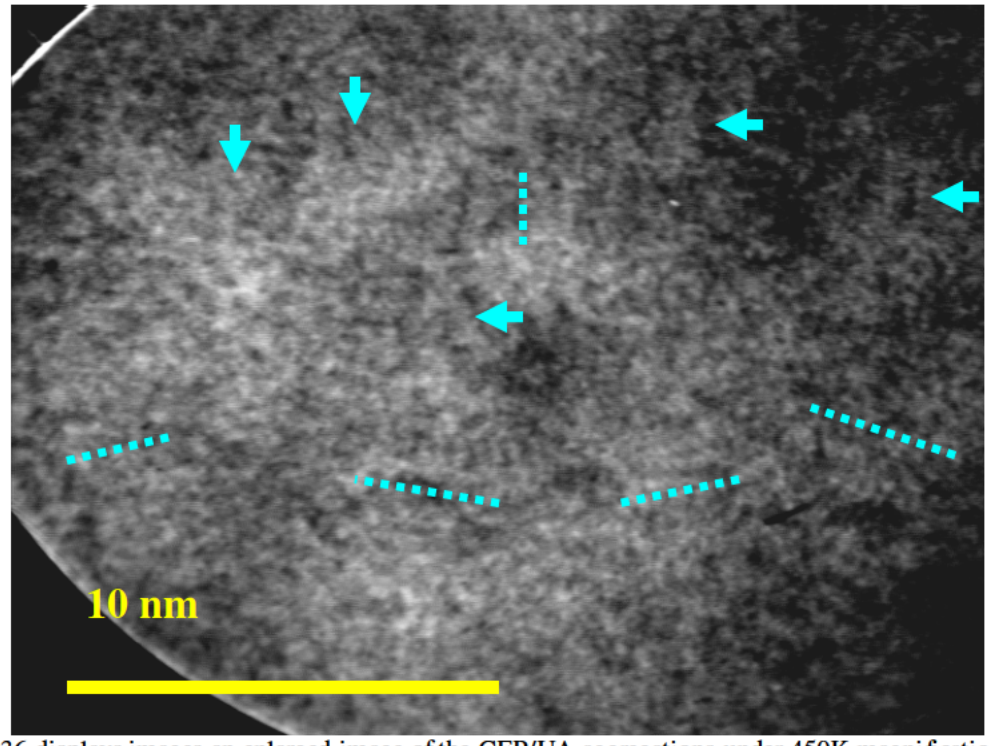

Figure 36 displays images an enlarged image of the GFP/UA aggregations under 450K magnification.

GFP His Tag Labeling with Ni-NTA-Nanogold

Despite extensive evidence that GFP had been successfully resolved using transmission electron microscopy (TEM), it was desirable to use a marker that might independently verify such findings. Because the commercially acquired recombinant GFP sample used in this study was prepared by affinity purification using a polyhistidine-tag, His tag labeling offered a viable option for selective labeling of the GFP sample. The protein provided by BioVision is 29 kDa with 265 amino acids, tagged with six histidine residues on both the N and C terminus. According to the product data sheet, the sample can be detected by both His-tag antibody and GFP antibody on Western Blot analysis. As seen in Figure 37, the N and C termini of the wild type GFP are located on one side of the barrel. Presumably the His tags would follow very closely and offer easy access for any marker.

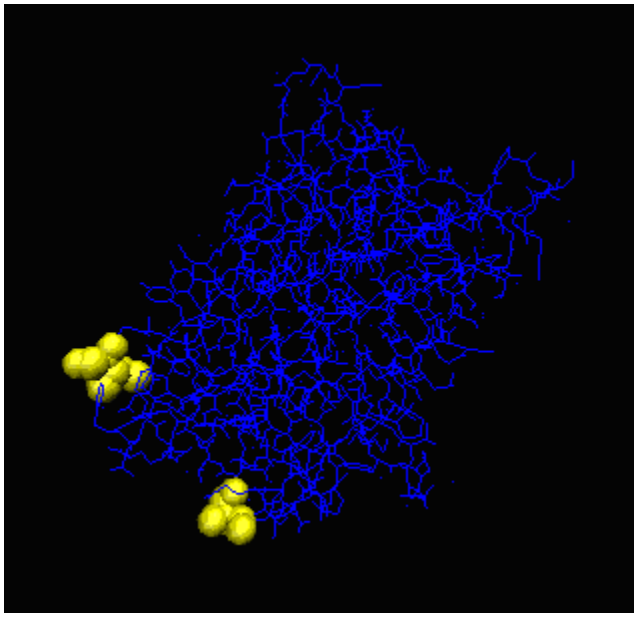

Figure 37 displays a wild type GFP with the N and C termini marked in yellow.

Because any marker would need to withstand the conditions of the electron microscope, nickel-nitrilotriacetic acid Nanogold (Ni-NTA-Nanogold) was selected for this study.

According to the manufacture, Ni-NTA-Nanogold is designed for detection of recombinant His tagged proteins using electron microscopy, light microscopy and blotting. Furthermore the imaging of the 1.8 nm gold particles was expected to be relatively straightforward compared to resolving antibodies with the electron microscope. Though providing good selectivity, antibodies are proteins and therefore might easily be confused with the GFP sample. However as experiments would show for negatively stained samples, the Nanogold presented some difficulty in being distinguished from uranyl acetate due to the high atomic number of both elements.

First several control experiments were in order before the Nanogold was used to label the GFP sample. Figure 38 displays a specimen of Nanogold that was diluted 1:5 with deionized water. The excess liquid was simply wicked off the formvar coated copper gird. When viewed just by itself, the gold was extremely easy to identify, even at relatively low magnifications. The contrast and stability of the sample proved excellent. The suspected gold particles are approximately 1.8 nm, but it is assumed that the nickel-nitrilotriacetic acid functionalities might also be visible. As seen in Figure 38D, it was possible to use a magnification setting of 750K to image the gold. Because this study did not normally image biological samples at such a high instrument magnification setting, no calibrated distance is available for this micrograph.

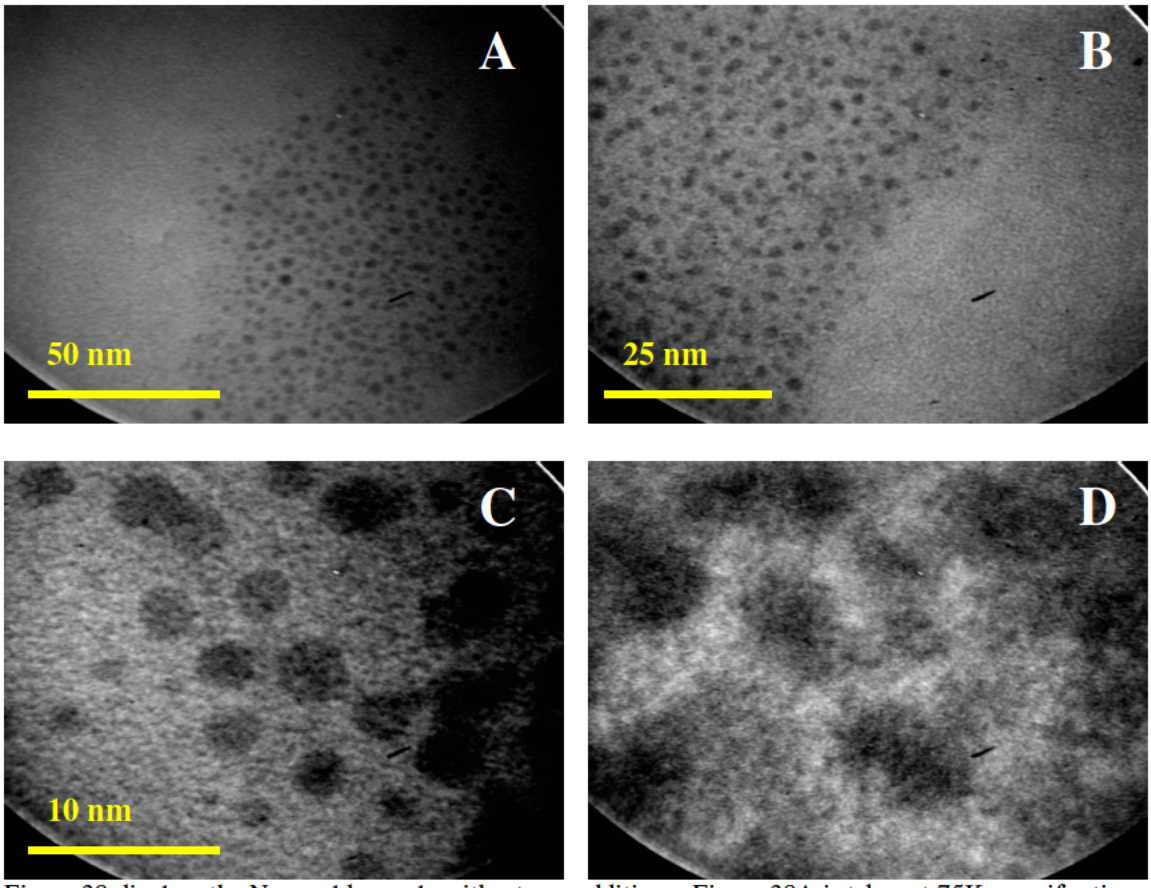

Figure 38 displays the Nanogold sample without any additives. Figure 38A is taken at 75K magnification, 38B is taken at 124K magnification, 38C is taken at 350K magnification, while 38D is taken at 750K magnification. The individual Nanogold particles are assumed to be the circular objects.

The next control experiment involved imaging the Nanogold negatively stained with uranyl acetate. The specimen was prepared similarly to the first control experiment except that after applying the diluted Nanogold, the grid was washed once with a 2% UA solution. As seen in Figure 39, the gold is visible at low magnification and appears to present itself in clusters in association with the uranyl acetate. At higher magnifications the gold is also visible, but the gold and uranium appear to be somewhat more difficult to distinguish between. However the darker circular objects, as indicated by blue arrows, are almost certainly the Nanogold.

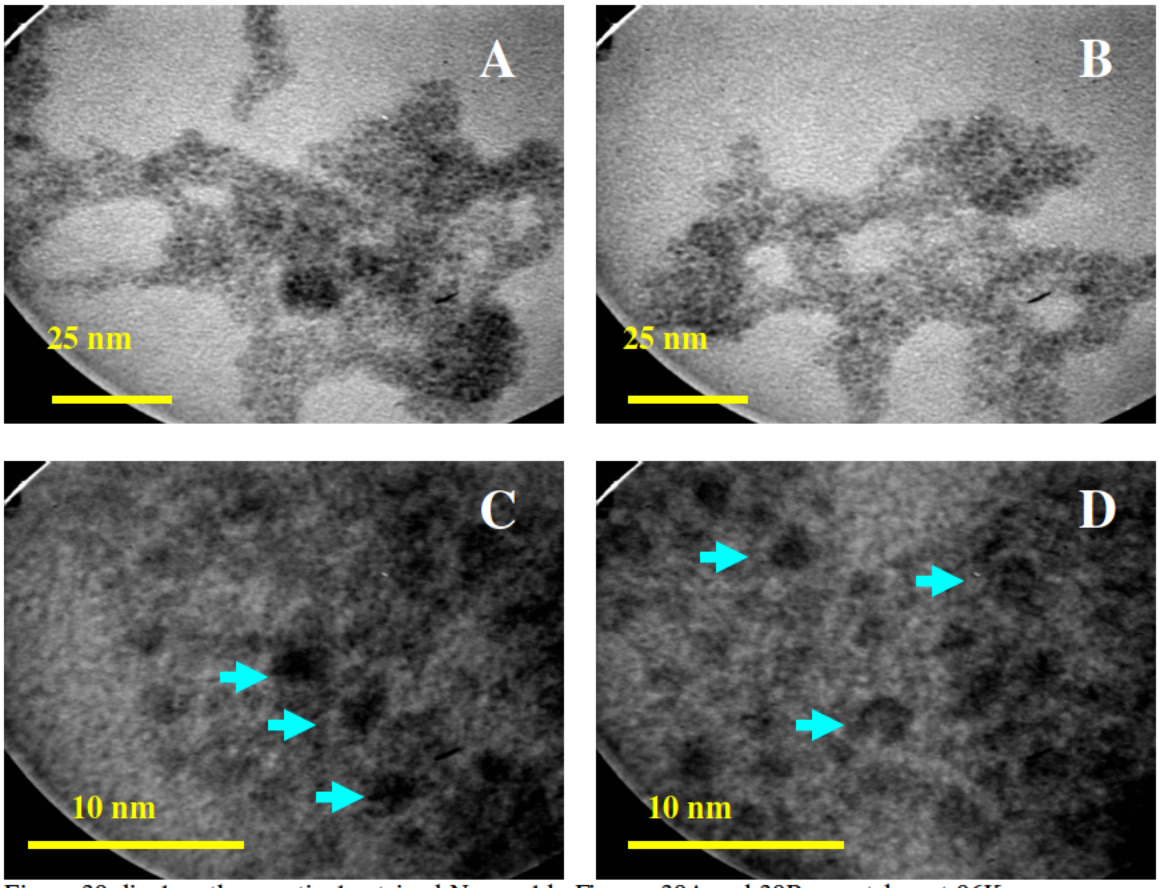

Figure 39 displays the negatively stained Nanogold. Figures 39A and 39B were taken at 96K magnification, while Figures 39C and 39D were taken at 450K magnification.

The following experiments examined GFP that was labeled with Nanogold, but not negatively stained. The specimen was prepared by diluting equal parts GFP sample with 1:5 Nanogold in deionized water. The preparation was allowed to incubate for 10 minutes at room temperature. As seen in Figure 40 the Nanogold labeled GFP appears to aggregate, although interestingly outliers tend to prominently appear in pairs as indicated by yellow circles. This raises the possibility that GFP molecules that did not aggregate were in some cases tagged with two Nanogold particles, one for each His tag. The larger aggregations representative of Figures 40A and 40D present the Nanogold quite clearly, but the areas in between the Nanogold particles are not as transparent as in the case of Figure 38B, which displayed the Nanogold without GFP at similar magnification.

Therefore it might be surmised that the aggregations present in Figure 40 constitute GFP that has been labeled with Nanogold. Figure 40D is even suggestive of some structural order. Figure 40E is an enlarged image of Figure 40D that has been processed using a fast Fourier transform (FFT) algorithm from Image- Pro Plus software to highlight a region of what appears to be an ordered lattice of gold and perhaps GFP.

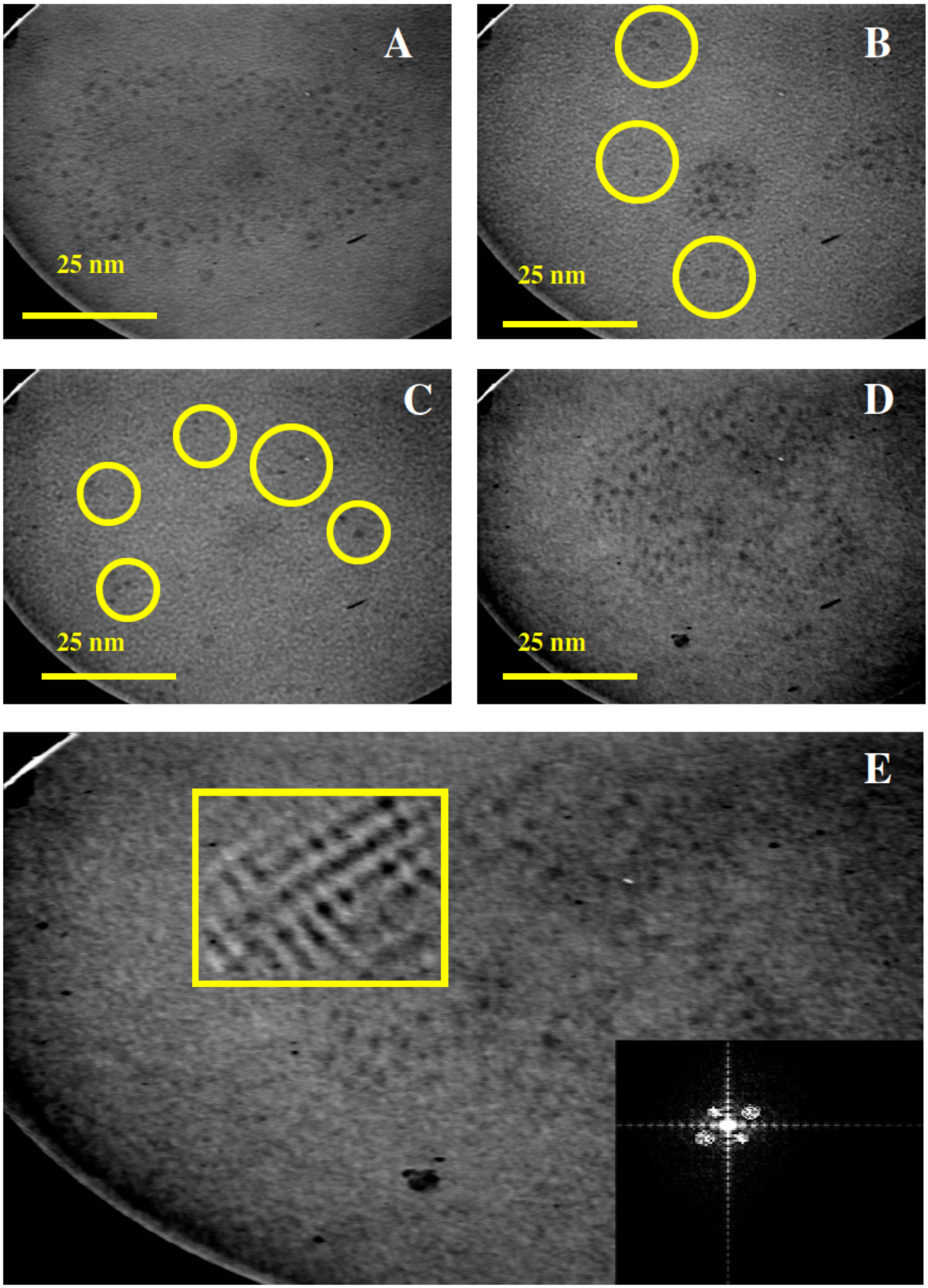

Figure 40 displays GFP labeled with Nanogold. Figures 40A through 40D were taken at 124K magnification. Figure 40E is an enlarged image of Figure 40D that has been processed using a fast Fourier transform (FFT) algorithm of Image- Pro Plus software to highlight a region of what appears to be an ordered lattice of gold and perhaps GFP.

Figure 41 displays the GFP and Nanogold specimen at a higher magnification. Like the lower magnification images, some ordering of the Nanogold particles is apparent. Often as indicated by blue arrows, the particles appear top to bottom as if in rows. Prominent pairs are also indicated by yellow circles. It is unknown whether this phenomenon is a consequence of the gold interacting with itself or a result of GFP aggregating and then being labeled with the Nanogold. Interestingly, the pairs of gold particles are approximately 3 nm apart, which might constitute the distance between the His tags on a single GFP molecule.

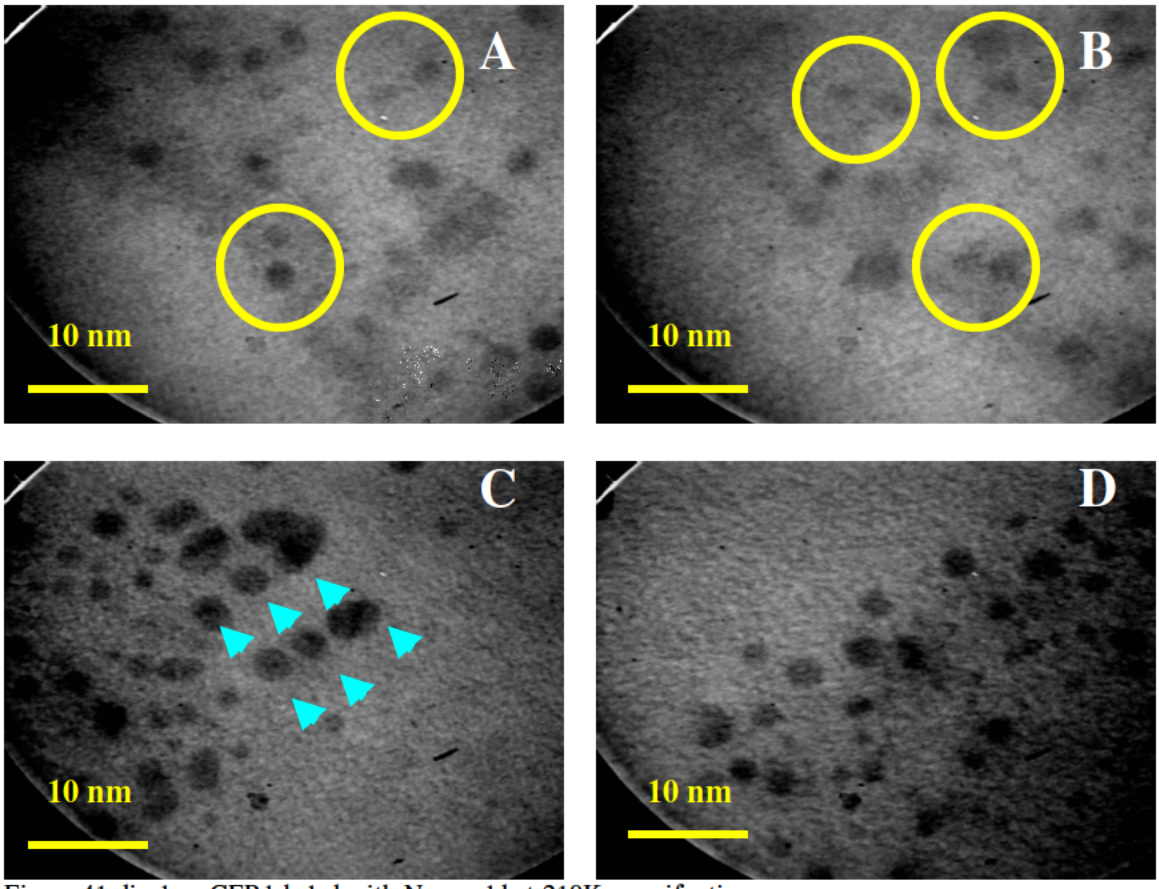

Figure 41 displays GFP labeled with Nanogold at 210K magnification.

The remaining micrographs in this section are devoted to specimens that combined GFP, Nanogold, and uranyl acetate. Apart from varying the concentrations of each constituent,

after applying the specimen to the formvar coated copper grid it was possible to either wash or not wash the grid with what was been referred to as a washing buffer. As suggested by the manufacturer, the intended purpose of the washing buffer was to remove Nanogold that was not selectively bound to the sample. The binding buffer referred to throughout the paper, but specifically described in the methods section was also proposed by the Nanogold manufacture as a method to increase the selective binding of the Nanogold to the target protein. After some trial and error, satisfactory protocols were developed that provided extensive evidence that the GFP sample was resolved, but the images fell short of our expectations that the Nanogold might incontrovertibly label the negatively stained discrete GFP molecules. This question will be addressed in greater detail during the results section.

Two protocols, protocol one and protocol two, were ultimately used to prepare specimens containing GFP, Nanogold, and uranyl acetate. The first protocol called for a stock 1:4 Nanogold solution diluted with the binding buffer. This stock Nanogold solution was then diluted 2:1 with GFP and allowed to incubate for approximately 20 minutes. The Nanogold/GFP solution was then applied to the grids and allowed to sit for 3 minutes. As the solution evaporated, a drop of 2% UA was applied to the grid and then dried with a wick after 5 seconds. The grids were then ready for viewing or alternatively washed once with the washing buffer. The second protocol incubated at room temperature for six minutes 8 µL of GFP with 18 µL of 1:5 Nanogold solution diluted with the binding buffer. 10 µl of UA were then directly added and the solution was applied to the formvar coated copper grids shortly thereafter. After sitting for five minutes and nearly evaporating, the excess liquid was removed with a wick and the grid was either ready for

viewing or alternatively washed three times with the washing buffer. Once again the excess liquid was removed with a wick.

Figures 42 displays specimens prepared using protocol one and was not washed. As seen the images share many similarities with those taken of negatively stained GFP. The lower magnification images of 42A and 42B look very similar to Figure 25. Areas where Nanogold can be seen labeling the sample are indicated by pink arrows. Differentiating between the Nanogold and uranium is difficult due to the tight packing of the aggregate and because the negatively stained surroundings of the proteins contrast somewhat poorly with the Nanogold. However many objects are visible at high magnification, some of them the recurring 'doughnut' motif, which appear to be in close proximity to a gold particle. These have labeled with blue arrows. It is difficult to say whether these objects have truly been selectively labeled with the Nanogold or whether they constitute GFP molecules that have simply been negatively stained so that a central portion of the object is differentially bound to uranyl acetate.

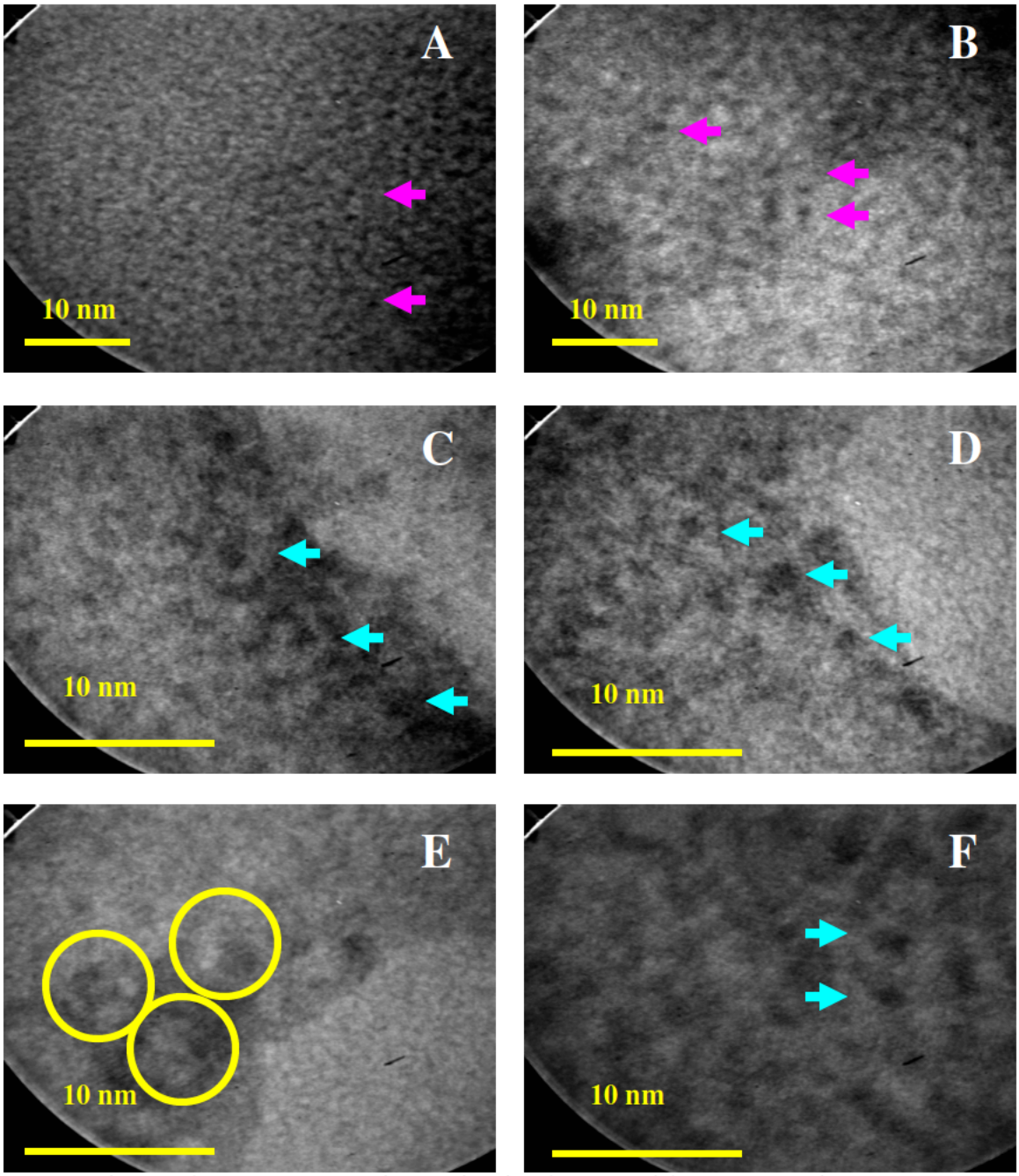

Figure 42 displays the negatively stained GFP labeled with Nanogold that was prepared using protocol one and was not washed. Figures 42A and 42B were taken at 210K magnification, while Figures 42C through 42F were taken at 450K magnification.

Figure 43 displays specimens prepared using protocol one and was washed once. Immediately it is clear that the images are not as cluttered as in Figure 42. Evidently washing the specimen positively increases contrast between the Nanogold and UA,

because the darker gold particles can be more easily differentiated. The lower magnification images of Figures 43A and 43B demonstrate that the gold has selectively labeled the sample or otherwise aggregated with it. Higher magnification images are not too unsimilar from those of negatively stained GFP and many objects which approximate the 3 by 4 nm dimensions of the GFP beta-barrel are resolved, some closely associated with gold particles. Blue arrows highlight some of the more prominent examples. Figure 43E is especially informative because prominent uranyl acetate lattices are visible, which confirms that the sample was negatively stained with UA.

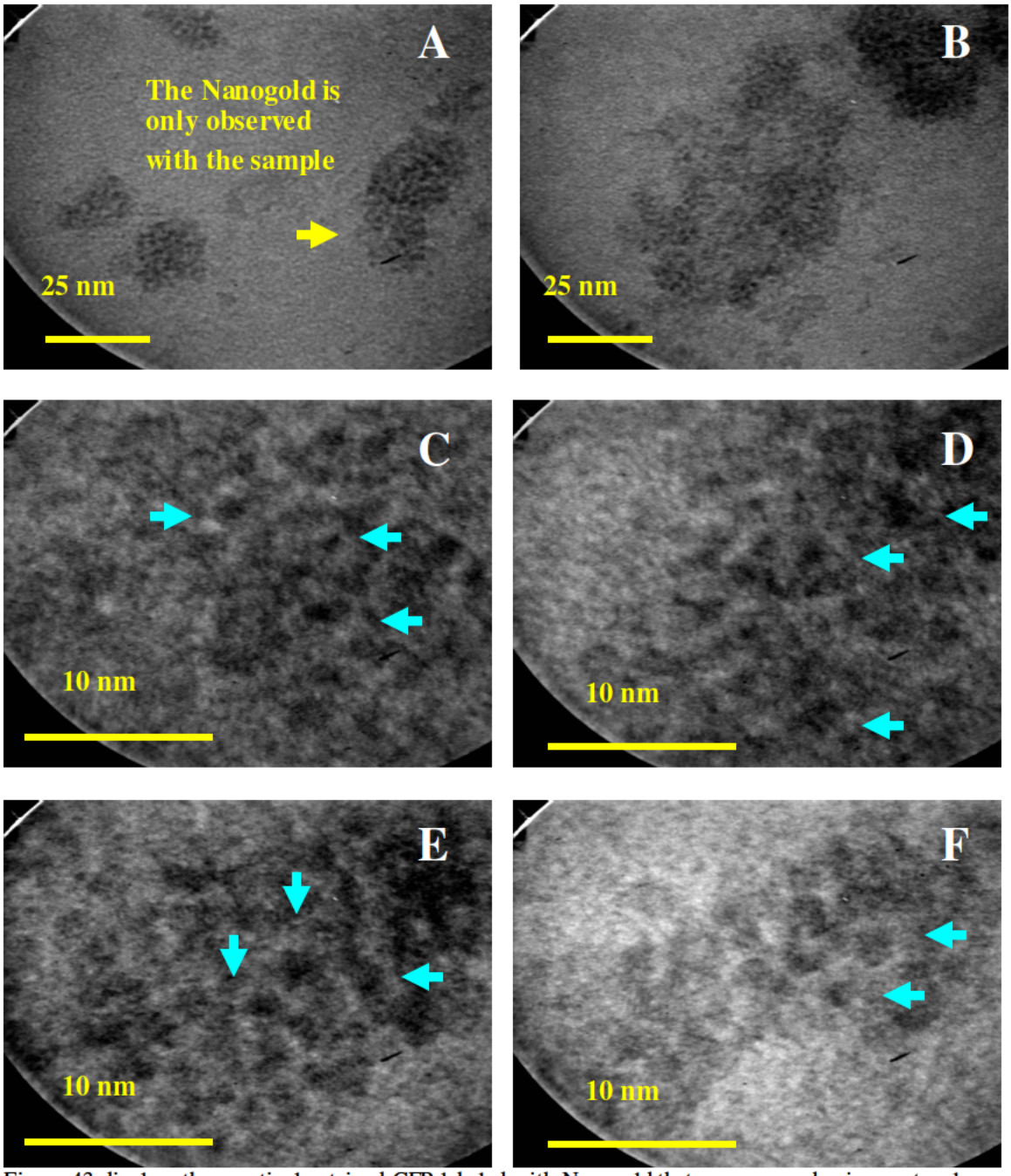

Figure 43 displays the negatively stained GFP labeled with Nanogold that was prepared using protocol one and was washed once. Figures 43A and 43B were taken at 96K magnification, while Figures 43C through 43F were taken at 450K magnification.

Figures 44 and 45 display images of a specimen prepared using protocol two that was washed three times. The specimen resembles closely negatively stained GFP. Many discreet objects orientated in multiple directions are visible in Figure 44, which presents

the low magnification images. This particular preparation had a lower concentration of gold and added UA directly into the solution before it was applied to the grid. Consequently the contrast between the gold, which seems to be somewhat scarce, and the uranium is poorer than in Figure 43. However darker circular objects embedded in the sample which might constitute Nanogold labeling are visible and for some examples have been indicated with blue arrows.

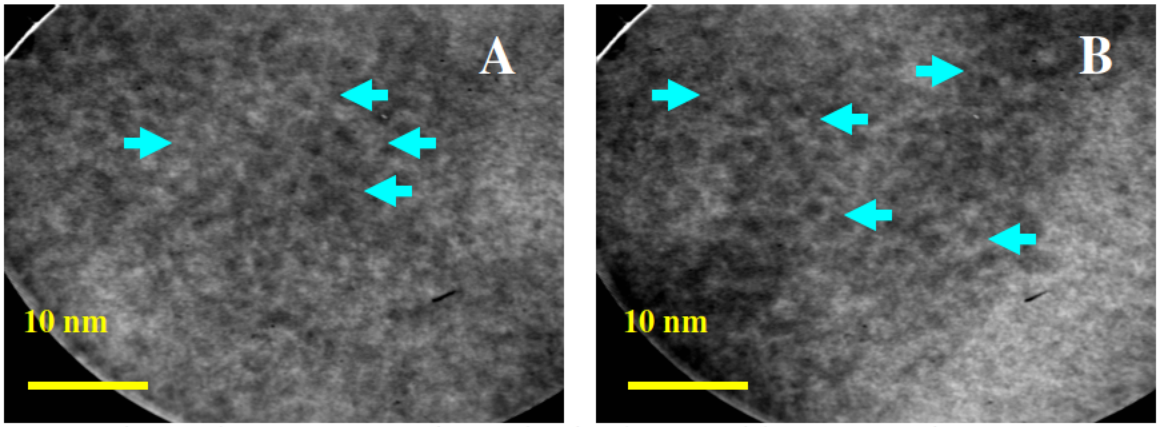

Figure 44 displays the negatively stained GFP labeled with Nanogold that was prepared using protocol two and was washed three times taken at 210K magnification.

Figure 45 displays high resolution images of those presented in Figure 44. Many fine lines are visible as are objects suspected of being the discreet GFP protein. Because the darker regions of the image are relatively uniform, it is difficult to differentiate between the Nanogold and uranium. However yellow circles indicate suspected GFP molecules.

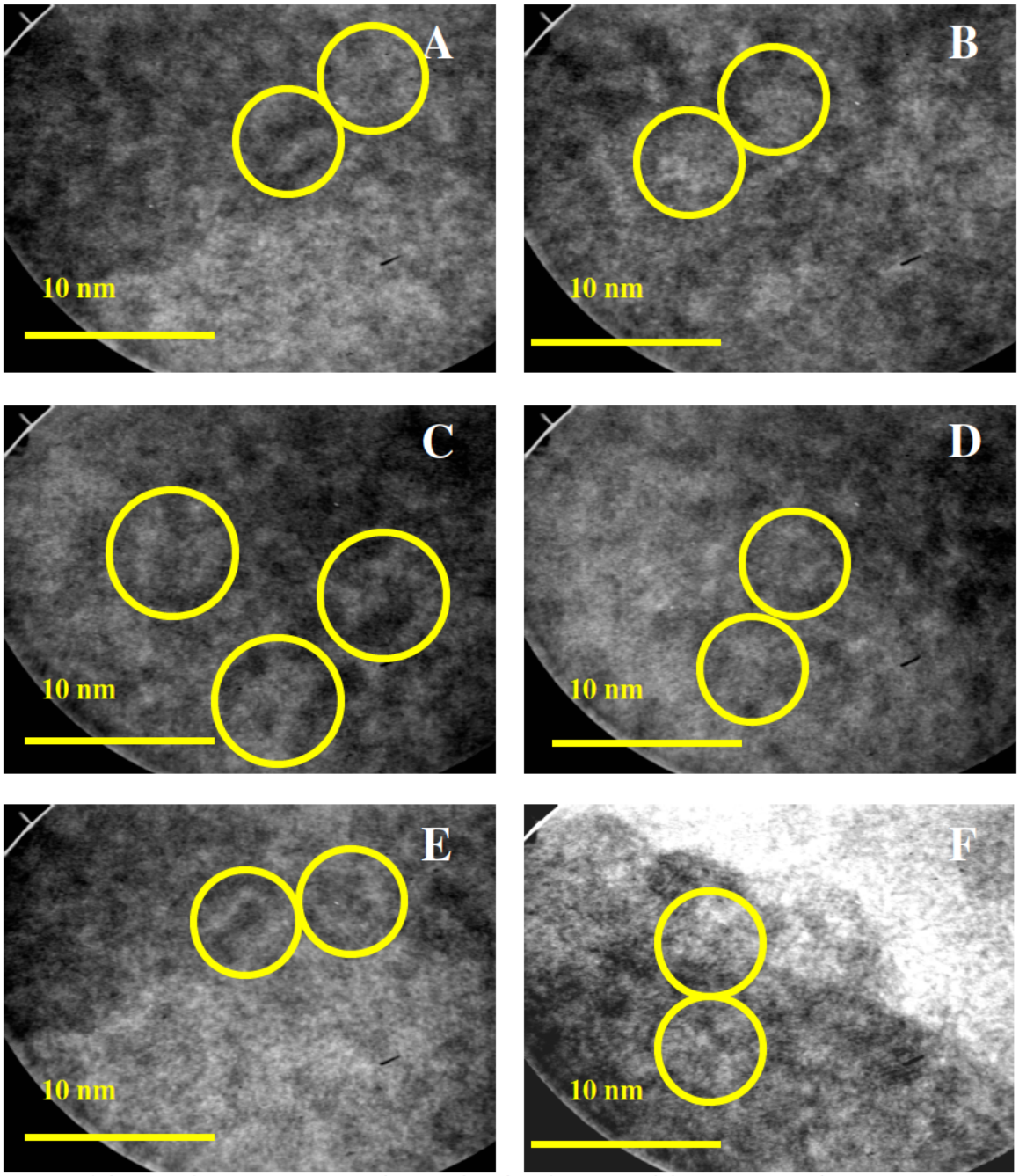

Figure 45 displays the negatively stained GFP labeled with Nanogold that was prepared using protocol two and was washed three times. All electron micrographs were taken at 450K magnification, while yellow circles draw attention to objects which approximate the dimensions of the GFP beta-barrel.

Discussion

GFP Crystal Formation

As evident from the fluorescent micrographs, the commercial GFP sample was quite active. Considering the declared purity of the sample is 97%, the fluorescence observed in Figure 7 is unexpected. More interesting however is the crystallization of the GFP in PBS solution. Under the light microscope as shown in Figure 7, elaborate patterns emerged that were suggestive of crystal formations as the GFP in PBS buffer solution desiccated. The observed images are undoubtedly crystal formations as indicated by the self-similar arrangement and well-defined angles. While the observed images are objectively of crystals, their composition is not so obvious. From Figure 7 it is clear that the crystal formations are not uniform; indeed multiple motifs are present. This would suggest that the solution is not uniform. Whereas Inoue successfully purified GFP by column chromatography and dialyzed against distilled water to remove salts, a PBS buffer served as the solvent for our GFP sample. Because PBS buffers contain sodium chloride and sodium phosphate, it is likely that the observed crystals are partly if not mostly the result of salt crystals which precipitated out of solution as the liquid GFP sample dried. Whereas Inoue reported purified GFP to form elongated needle shaped crystals, 3-μm to under 1-μm wide and approximately 20- to 100-μm long, the crystals observed in Figure 7 are not exactly uniform. However the possibility that the observed crystals are comprised of both GFP and salts cannot be eliminated because as observed in the fluorescence microscope, the crystals are fluorescent. The buffer salts and GFP would therefore appear to have assembled into a crystalline aggregation.

Fluorescence as an Indicator of Protein Integrity

Interestingly the TEM vacuum of 10^{-7} Torr appeared to have no noticeable effect on the GFP sample's fluorescence, while the electron beam sharply decreased fluorescence. Previous studies have demonstrated that GFP is structurally resilient to external disturbances. Thus it would appear that GFP is resilient to dehydration as well. To what degree the crystalline aggregation of GFP, buffer salts, and uranyl acetate protect the protein will remain a question of great interest in this discussion.

As seen in Figure 8, GFP fluorescence in the specimen region exposed to the electron beam was clearly diminished. Two explanations for this observation come to mind. One possibility is that the electron beam has destroyed the beta-barrel, thus disrupting the internal environment which is essential for the formation and maintenance of the fluorophore. It is alternatively possible that the electron beam has left the beta-barrel largely intact, but impaired the function of the fluorophore alone. Either way, it was encouraging to still see some fluorescence after exposure to the electron beam, which suggests that low dose TEM might successfully image an intact GFP molecule. As seen in Figure 9, the negative staining process does not appear to significantly affect GFP fluorescence. Any decrease in fluorescence is most likely attributable to the decrease in GFP concentration seeing as the negative staining protocol called for the dilution of one part GFP with a one part 2% UA solution. Either way fluorescence of the sample suggests functionality and therefore confirms the structural integrity of the GFP molecule.

GFP and Uranyl Acetate Aggregation

One significant conclusion that can be drawn from this study is that the GFP aggregations exhibit a continuum of organization. The most noticeable difference between GFP and negatively stained GFP specimens, as compared by Figures 8 and 9, is the dissimilar deposition of fluorescing units on the grids. While the GFP stained with UA exhibited similar crystal formations as those observed in pure GFP, the aggregations and their patterns of deposition were more compact. Fewer long needle like crystals can be seen and the fluorescent aggregations are less diffuse. The GFP, UA, and buffer salts have produced what appears to be a co-crystalline complex, while the GFP, despite dehydration, has not lost fluorescence. Thus crucially the protein has not lost intrinsic structure or function as a result of the negative staining process. The evidence strongly suggests that the observed electron dense objects are in fact aggregations of the GFP, UA, and buffer salts which were directly applied to the formvar coated grids. In view of the fact that no other substance was applied to the grids, it is highly unlikely that the observed objects represent anything but the sample.

The preparation of negatively stained GFP produced large aggregations of electron dense material visible at magnifications as low as 3K as displayed in Figure 13. The question over whether such objects represent crystals or simply irregular aggregations of GFP, UA, and PBS buffer salts is complex. Evidence supporting a crystal hypothesis includes Figures 15, 16, and 17 which display well-defined triangular crystals under various magnifications. The sharp nature of the boundary between the formvar and the sample is suggestive of the ordered margins of a crystal. Unambiguous highly ordered diffraction patterns and high resolution images which appear to show tightly packed subunits

provide further evidence for the formation of crystals. One interesting question is whether these crystals formed in solution or as a result of the dehydration process. Figure 16, with its intricate arbor like crystals would suggest that the crystal formed as the liquid dried. However Figure 18 and the large triangular crystals indicate that the UA may have settled on top of previously formed crystals.

Other aggregation phenomena are visible as well. Figure 14 lacks a well defined crystalline appearance. These darker and somewhat smaller aggregations are displayed in Figure 14 at a low magnification of 17K. The objects do not appear to have a uniform structure, are irregularly shaped, and lack the distinct geometries of any crystal. Figure 18C is unique in that it shows both a crystal and less ordered aggregation of the GFP sample in the same viewing area. Thus it would appear that the GFP sample aggregates to varying degrees of structural order. Whether or not these aggregates represent true crystals or an amorphous conglomeration of GFP and UA remains unknown given the current data. Some aggregates are linear as in the observed GFP monolayer, others are polygonal as seen in Figure 27, while the regular patterns of Nanogold as displayed in Figure 40 indicate that the aggregations of the sample are not just random. The most highly organized structures are represented by the obvious crystals observed in Figures 15, 16, and 17. Additionally the monolayer of the discrete GFP protein observed along the edges of some crystal formations, as displayed in Figures 20 and 21, and within certain folding regions, as displayed in Figures 22 and 23, ought to appropriately be counted among the more ordered examples of GFP aggregates. Conversely more indefinite aggregates, such as those displayed in Figures 14, 25, and 26 possess less

structural organization. But even these examples, which lack the remarkable order of the discrete GFP protein monolayer, possess some recurring features and motifs.

At higher magnifications the sample displays an unexpected and novel aggregation phenomenon. In Figures 25 and 26, taken at 124K and 160K magnification respectively, recurring motifs that are too large to be the discrete protein are ubiquitous and in many cases continuous. It is therefore suggested that the even the less definite GFP aggregates possess some organization as apposed to being completely amorphous. The visualization of these recurring structures is made possible by the intrinsic capability of TEM to image the whole field of view over a range of magnifications. Figure 46, which is an enlarged image of Figure 27A, displays several examples which appear to arrange themselves around a central pore creating a 'doughnut.' This 'doughnut' motif is speculated to be an ordered arrangement of GFP that has assembled into some polygon aggregate. Smaller 'doughnuts' may represent the GFP beta-barrel with the short axis facing upwards. As visible from the micrograph, the circled objects appear themselves to be made of constituent parts. Thus the GFP may be forming dimmers, trimmers, or some other macromolecular complex. While Figure 46 displays a specimen that was not previously exposed to the electron beam and for which low TEM was consistently employed, Figure 47 was previously irradiated with the electron beam before examination. Unlike Figure 46 no GFP complexes are observed in Figure 47, an enlarged image of Figure 26B taken at 160K magnification, while the specimen itself presents a more amorphous quality. However the contrast and brightness of the image has been altered to better illustrate how the discreet GFP associates in more indefinite aggregations. The most interesting quadrant of Figure 47 is the lower right, which shows many densely packed objects

which the uranium doesn't seem to have penetrated very well. The additional electron beam exposure may have degraded the specimen, but discrete objects are visible nonetheless although their dense arrangement makes examination difficult.

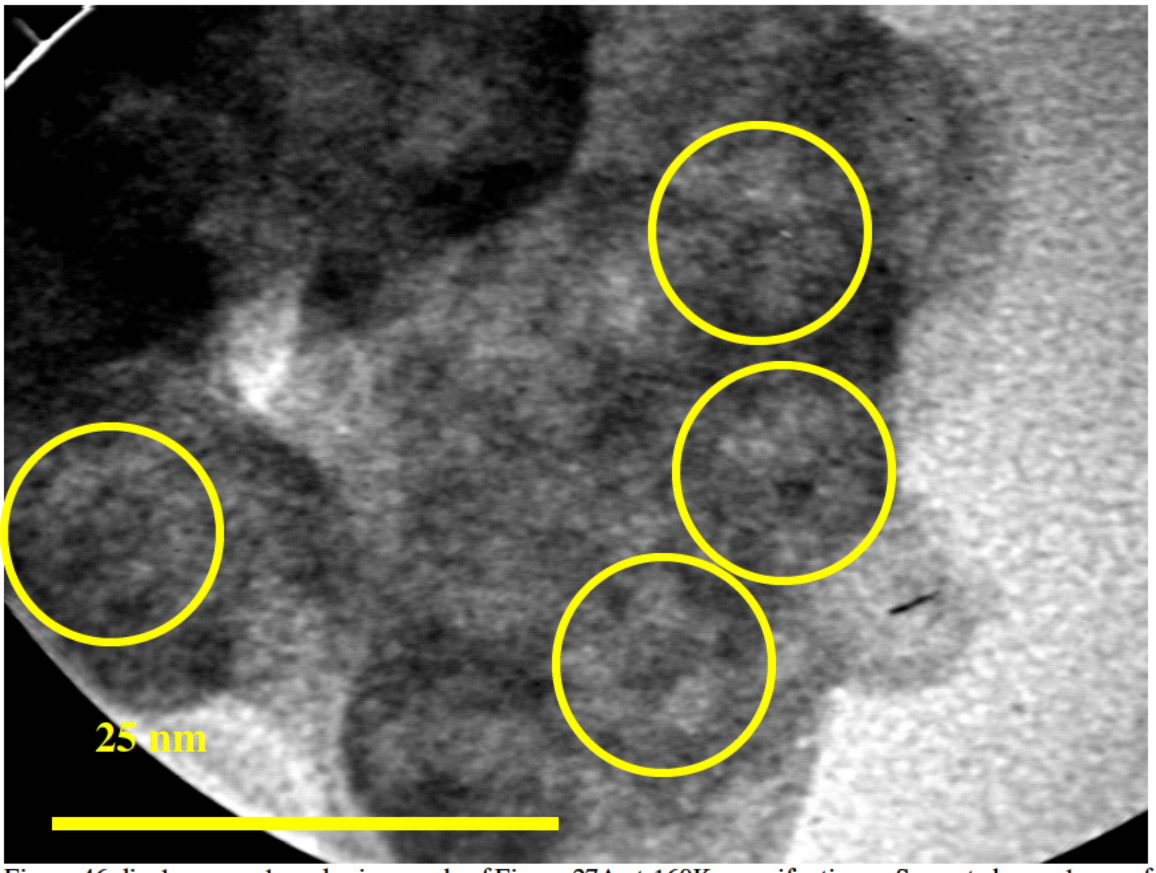

Figure 46 displays an enlarged micrograph of Figure 27A at 160K magnification. Suspected complexes of GFP are designate by yellow circles.

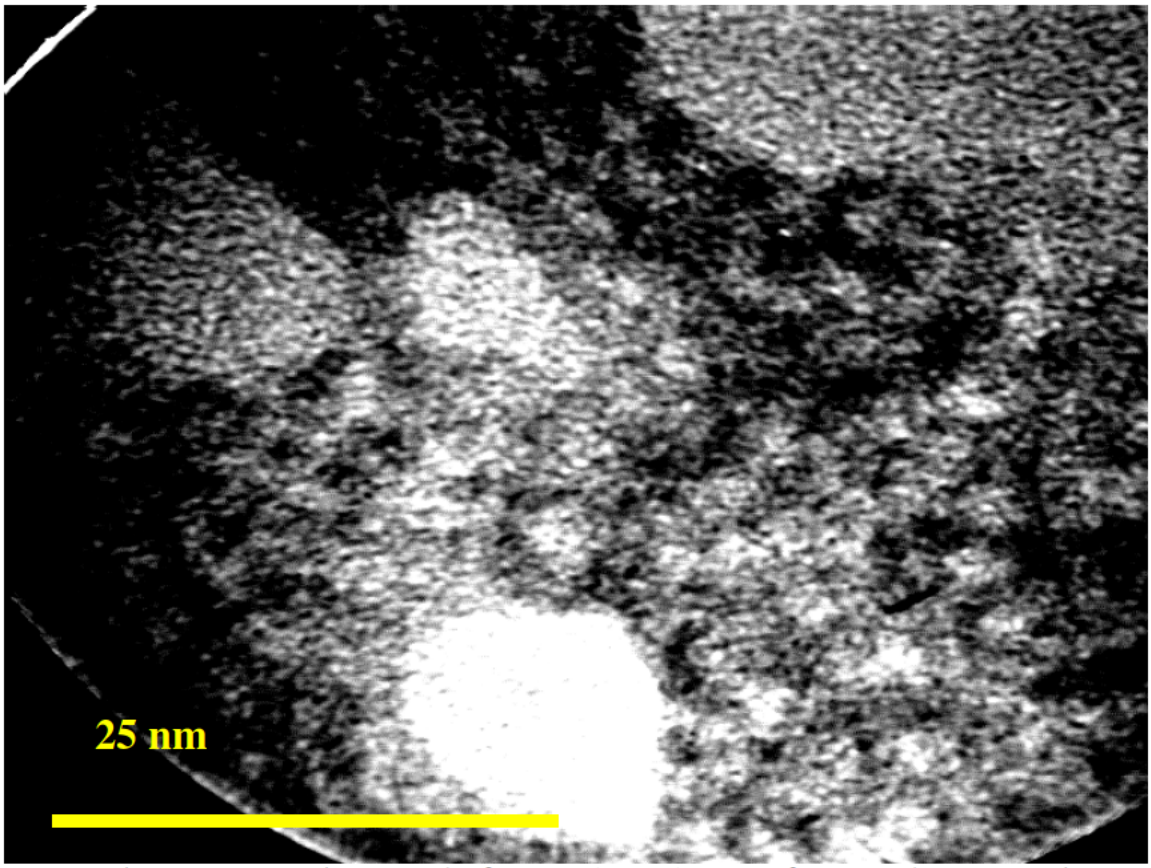

Figure 47 displays an enlarged micrograph of Figure 26B at 160K magnification. The contrast and brightness of the figure has been altered to better differentiate between the constituents of the aggregate. The lower right quadrant of the micrograph shows a region of the aggregate that is densely packed, though what appear to be discrete objects are still detectable.

Because this study has characterized the many varieties by which negatively stained GFP aggregates and simultaneously resolved the discreet green fluorescent protein, it may prove useful in the research of other proteins that are insoluble, aggregate, or do not readily crystallize. X-ray diffraction produces the highest quality 3-D structural data of large biological molecules with a resolution of 2-3.5Å, but the process requires that the protein be amenable to crystallization.

Amyloids, insoluble protein aggregates consisting of tightly packed beta sheets, are responsible for various diseases in humans known as amyloidosis and are suspected in participating in the pathology of neurodegenerative diseases such as Alzheimer's.

Previous studies have attempted to examine β-amyloid fibrils using a uranyl acetate negative-stain with TEM, but encountered the old problem of radiation damage from the electron beam and did not even begin to approach HRTEM, which would offer structural data for the specimen at the atomic level (Apkarian et al, 2003). Because GFP is an 11 stranded beta-barrel composed of individual beta-strands, GFP does share some similarities with amyloid, which is a proteinaceous deposits that polymerize to form cross-beta aggregates. The more important conclusion to be made from the HRTEM study of GFP is that HRTEM may be an underutilized tool for examining the structure of protein aggregates.

Prion disease such as Creutzfeldt-Jakob disease (CJD), bovine spongiform encephalopathy (BSE), and scrapie are infectious agents which corrupt normal proteins, designated PrP, to the abnormal infectious protein, designated PrP^{Sc}. While the PrP isoform is soluble, the PrP^{Sc} isoform remain intractably insoluble and unamenable to X-ray crystallography and NMR spectroscopy. Interestingly in 2007 a specially prepared PrP^{Sc} isoform, complexed with heavy metals, was examined with HRTEM. Among the aggregates were found 2D crystals of the protein (Wille et al, 2007). Thus the potential of TEM using relatively simple negative staining techniques for imaging protein aggregates has some support in the literature and is further reinforced with our HRTEM study of GFP. However because the structure of GFP has been previously resolved using X-ray crystallography, it is possible to directly compare the images acquired to known models of the protein.

Aggregation phenomena are also of interests in developing recombinant GFP fusion proteins. Interestingly the over expression of recombinant proteins, including GFP fusion proteins, in *E. coli* have been shown induce both amorphous and organized inclusion bodies (Schrödel and de Marco, 2005). Evidence presented in this study suggests that GFP fusion proteins might assume aggregations predicated by GFP itself.

Uranyl Acetate Binding

In order to appreciate HRTEM images of the discreet GFP molecule, it is first necessary to understand exactly what is being visualized. Transmission electron microcopy works much like a light microscope in that rather than light, an electron beam is transmitted through the sample - See the appendix titled "How Does a Transmission Electron Microscope Work" for a more in depth explanation. Those regions of the specimen that are more electron dense appear darker, whereas areas with less electron density more easily transmit electrons and appear brighter. Uranyl Acetate, the most common negative stain, was used to prepare the GFP sample for TEM. UA is a substance with high electron scattering properties and thus improves contrast, which remains the main limit to the resolving power of electron microscopes. Thus the uranium appears as a dark background, while the unstained specimen appears bright relative to its surroundings. The uranium also serves to minimally protect biological specimens form the electron beam (Kondo and Brown, 2001). TEM experiments examining unstained GFP demonstrated that the protein by itself remains relatively sensitive and unstable in the electron beam compared to stained samples of GFP.

As observed in the fluorescence micrographs and low magnification TEM images the GFP, UA, and buffer salts assembled into various aggregations including crystals as the liquid sample desiccated. Therefore the UA would appear to have associated with the GFP in a co-crystalline complex. As observed in Figure 24, the control experiment with no UA leaves the screen with very little contrast. The only visible objects are the formvar polymer chains. It is also worth recalling that the GFP proteins are much larger than the uranium atoms. Even though they are small, it is the uranium atoms that are responsible for the increased contrast due to their high electron scattering properties. Therefore it is helpful to consider how the UA stain interacts with the protein sample.

Depending on pH and concentration, the UA solution contains uranyl ions which may form anionic, neutral, or cationic complexes with the acetate. These uranyl ions associate deferentially with negatively charged groups, even phosphate ions of the buffer solution. These electrostatic interactions explain the fundamental principle behind the affinity of UA for the specimen (Hyatt, 2000). It has been determined that uranium salts bind preferentially to the negatively charged residues of Glutamic and Aspartic acid, although uranyl ions will also associate with the positively charged residues of Arginine, Histidine and Lysine (Hyatt, 2000). Figure 32 displays 4 orientations of a GFP Vander Walls radii space filling model designated as 1EMA in the protein data bank, rendered through the Visual Molecular Dynamics (VMD) molecular visualization program. The red corresponds to negatively charged residues, while the blue corresponds to positively charged residues. Of interest to UA deposition for the GFP sample used in this study is that it has a Histidine tag. As such the range of positive charges would be greater for the Enhanced Green Fluorescent Protein (EGFP) than would be indicated by Figure 48. The

last picture is a HRTEM image of a suspected GFP molecule under 450K magnification. Notice the specific regions of UA deposition on the molecule that have been labeled with pink arrows. It is possible that these regions correspond to the charged residues of the GFP protein, but this remains unknown given the current data. Figures 49 through 54 offer more examples of HRTEM images of objects suspected of being the discreet GFP molecule. With further analysis it may be possible to match the predicted regions of UA affinity with the HRTEM images. The ultimate goal of such a scheme would be to map intramolecularly various charge regions. Although this tantalizing prospect has yet to be realized, the mere possibility serves to recognize that the resolution of GFP by our method involves the atomic scale and thus constitutes HRTEM.

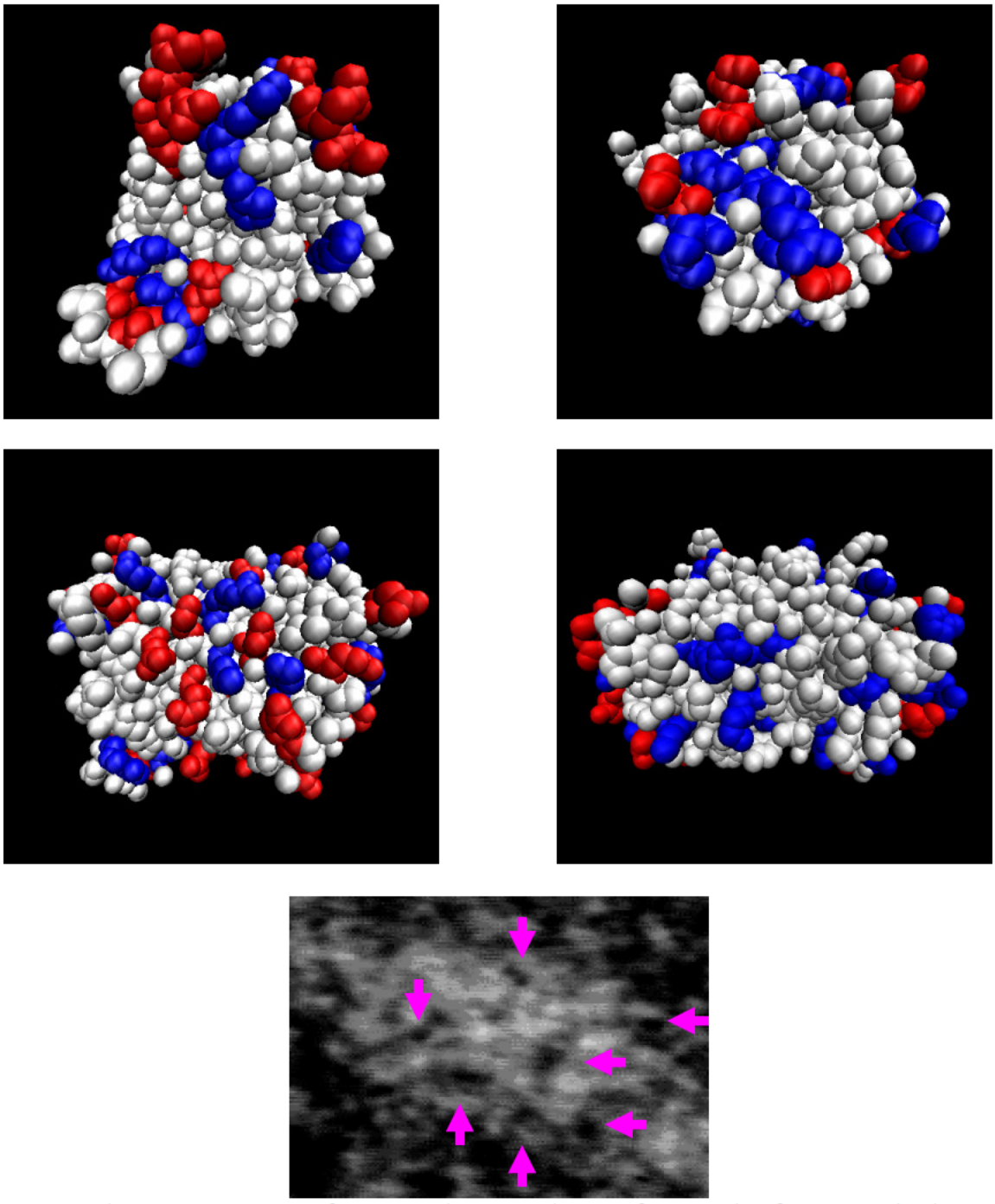

Figure 48 displays 4 orientations of a GFP Vander walls radii space filling model of 1EMA, rendered through VMD. The red corresponds to negatively charged residues, while the blue corresponds to positively charged residues. The bottom electron micrograph is a HRTEM image of a suspected GFP molecule under 450K magnification. Notice the specific regions of UA deposition on the molecule that have been labeled with pink arrows. It is possible that these regions correspond to the charged residues of GFP.

Comparison of Suspected Discrete GFP Molecules to Models of GFP Derived from X-ray Diffraction

While X-ray crystallography has solved the structure of GFP to a resolution of 2 angstroms or better, little if any published work has attempted to characterize the structure of GFP through transmission electron microscopy (Yang et al, 1996). The following galleries compare the known model of GFP to those examples derived through HRTEM which approximate the 3 by 4 nm dimensions of the GFP beta-barrel. Each grouping was taken from one figure or a series of figures and enlarged similarly to within an accuracy of 5%. The brightness and contrast of some images have been altered to emphasize the individual GFP molecules. Of note is that a number of orientations of individual molecules contributed to these galleries. Crucially the observed objects are not a sphere, but rather have a long axis. Thus what has been imaged is a cylindrical object in many different views.

Those monolayers observed along the edges of some crystal formations, as displayed in Figures 20 and 21, and within certain folding regions, as displayed in Figures 22 and 23, are an unambiguous example of the discrete GFP protein. The units are approximately 3 by 4 nm, which constitute the dimensions of the GFP beta-barrel, but more importantly are suspected to have organized into a monolayer whose edge, due to its relative transparency, was more easily resolved by the electron microscope. Each unit of the monolayer was easily differentiated because of the ordered nature of the arrangement. Figure 49 displays a space filled model of GFP, rendered through MDL Chime, alongside the monolayer examples. Most of the suspected proteins appear as an opaque rectangle, just as the space filling Vander Walls radii model would predict when examined in two

dimensions. Some have a characteristic region of heavy uranium deposition, indicated by a dark splotch. The uranium might be deferentially binding to charged residues or have conceivably entered the beta-barrel.

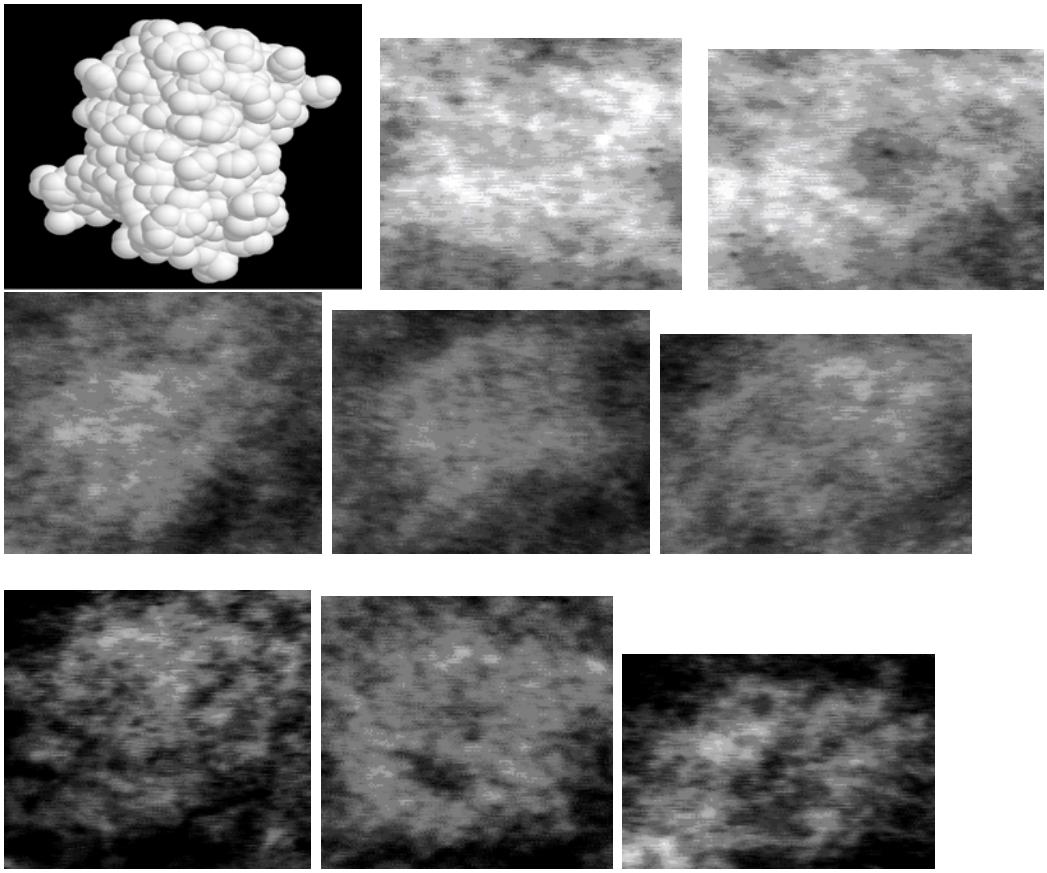

Figure 49 displays a space filled model of GFP, rendered through MDL Chime, along with enlarged objects from Figures 20 through 23 taken under 350K magnification. The units of the monolayer, which correspond to individual GFP proteins, are exquisitely differentiated.

Figure 50 displays barrel shaped objects taken under 350K magnification from Figure 27B. Though the magnification used to image these objects was equal to the monolayer example, the resolution is poorer. This discrepancy is likely a consequence of the objects not having been a component of an ordered crystalline monolayer. Rather the objects were imaged from an aggregation that while not completely amorphous, exhibited little ordered structure.

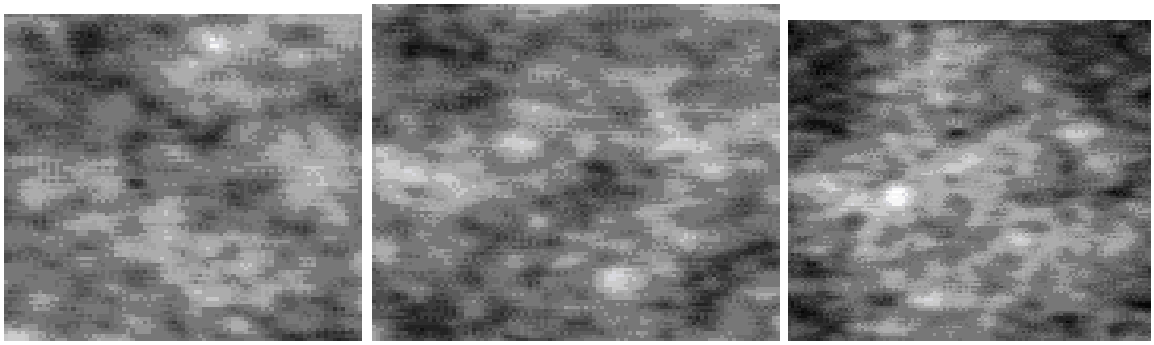

Figure 50 displays enlarged objects from Figure 27 that resemble GFP under 350X magnification

Figure 51 displays enlarged suspected GFP proteins from Figures 29 and 30 alongside two GFP ribbon diagrams (protein data bank 1EMA and 1GFL). The objects are similar to those displayed in Figure 49. In each case parallel lines with heavier uranium deposition between them form the likely GFP candidates. The two parallel lines motif may represent the beta-barrel on its side, with the increased electron density of the edges having resulted from the overlap of beta strands. See Figure 1B which illustrates a beta-barrel with one side removed to reveal the fluorophore; at the edge of the beta-barrel where the beta strands begin to wrap around and form a mesh like pattern, electron density as perceived by the electron microscope might reasonably produce the observation of two parallel lines. The darker area might correspond to areas of higher UA deposition on the surface of the beta-barrel or UA penetration, while the edges would bind poorly to the UA as a result of the compact nature of the beta sheets.

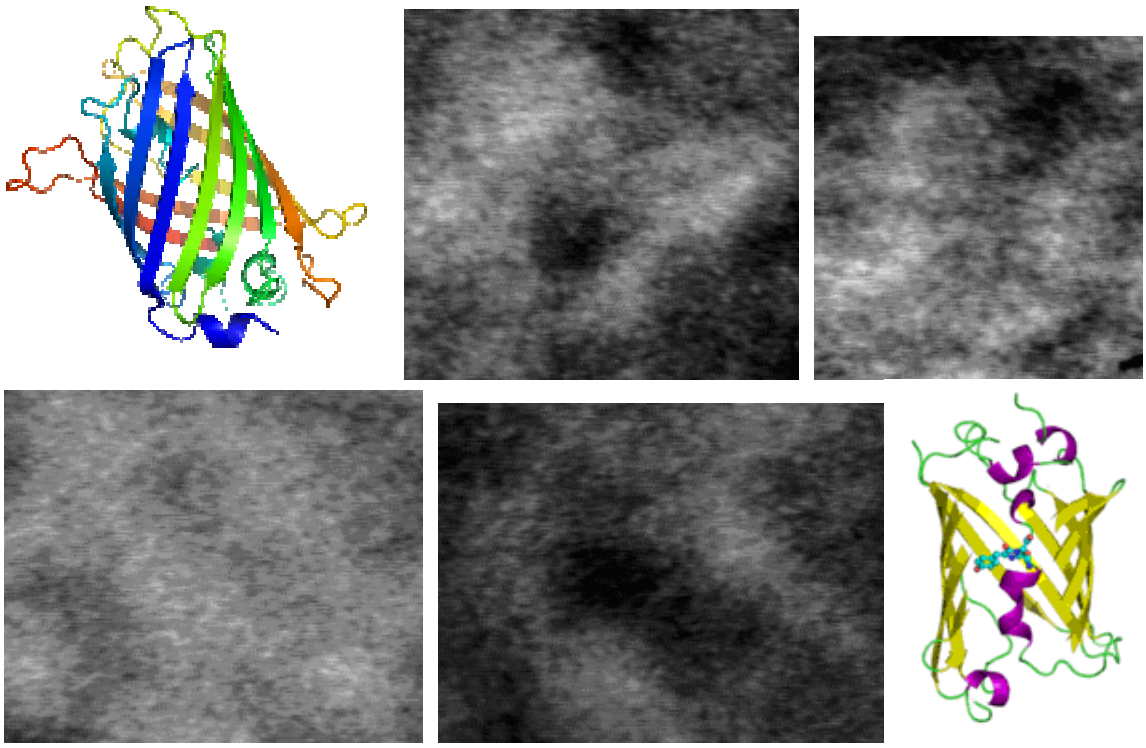

Figure 51 displays enlarged suspected GFP proteins from Figures 29, and 30 with two GFP ribbon diagrams (protein data bank 1EMA and 1GFL). The illustration of 1GFL has one side of the beta-barrel removed to reveal the fluorophore, which also serves to demonstrate how the beta sheets overlap near the edge of the protein, thus possibly creating an electron dense region that would not easily be penetrated by uranium.

Figure 52 displays more examples of probable GFP molecules, taken at 450K magnification from Figure 31, alongside a space filled model of GFP rendered through MDL Chime. Because this group was imaged with the highest magnification setting employed during the study, they offer the best resolution among the galleries. Additionally the specimen was unique because low dose TEM was employed. The area of electron exposure was small and the intensity likely never exceeded 1 pico ammeter. As a consequence, Figure 52 approaches the limits of HRTEM for resolving biological specimens, without resorting to image processing techniques such as Fourier transforms, computer modeling, or assembly of hundreds of images to form a composite. What appear to be regions of deferential uranium deposition are visible as are fine lines that

perhaps represent the polypeptide chains. If this analysis is correct, this is the first time to our knowledge that a globular protein, let alone GFP, has been imaged with HRTEM, to a resolution which permits the visualization of secondary protein structures. Importantly the TEM micrographs of the GFP sample resemble the X-ray crystallography derived models of GFP. Although this method does not easily translate into a model which describes the precise location of every residue, given the primary sequence of the protein is known, it has been demonstrated that the direct visualization of GFP and perhaps other proteins is possible employing simple, almost crude, negative staining techniques without the aid of complex image processing. It is doubtful that TEM would ever replace X-ray crystallography or NMR, but it does provide a useful real time compliment for the direct visualization of proteins that normally wouldn't be amenable to the standard techniques in structural biology studies.

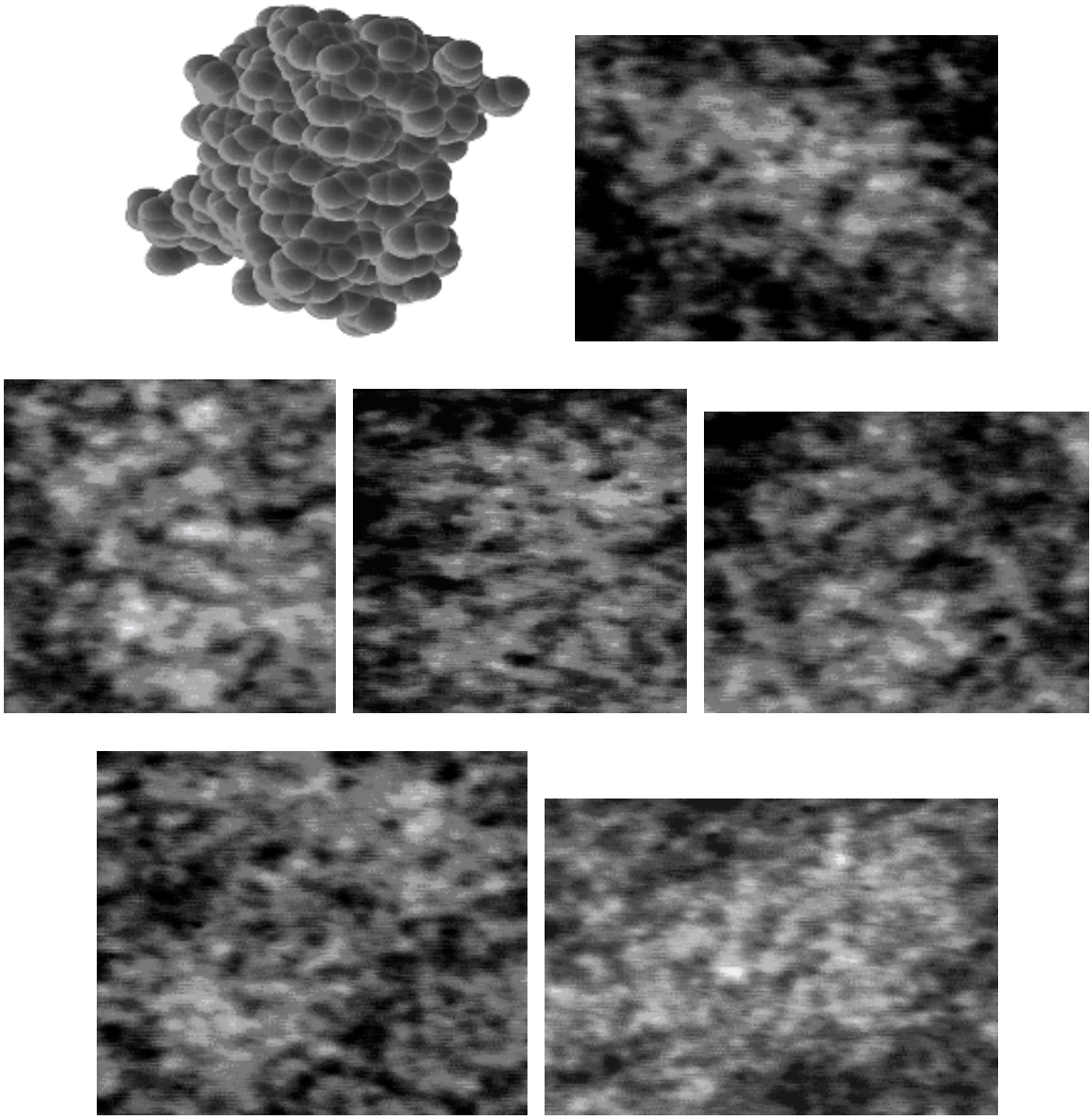

Figure 52 displays a space filled model of GFP, rendered through MDL Chime, along with enlarged objects from Figure 31 under 450K magnification.

Conclusions from Ni-NTA-Nanogold Labeling

It was hoped that the Nanogold would provide a definitive marker of GFP with His tag labeling. However as evident from the control experiments, GFP labeling with Nanogold, and negatively stained GFP labeling with Nanogold, the results were inconclusive. As seen in Figure 38, when viewed alone the gold is quite easy to spot. However when negatively stained the gold seems to experience a more profound

clumping effect. Furthermore, while it is still possible to distinguish between the gold and uranium, the gold is not as visible as it once was. These observations raise several confounding variables. Because the gold seems to clump when negatively stained, it is not known whether negatively stained GFP labeling with Nanogold is selective. In other worlds it would be difficult to know if the gold was binding selectively to the His tags or if the particles were simply aggregating along with everything else. Another confounding variable is the high atomic numbers of both gold and uranium. With TEM, the relatively high atomic number of both elements compared to those which comprise GFP makes it difficult to differentiate between the two, especially when GFP, Nanogold, and UA are combined in the same specimen. However as Figures 40 and 41 demonstrate, when GFP is labeled with Nanogold, but not negatively stained, the gold particles appear to have some order. Those outlying particles that our found outside of large aggregations appear mostly in pairs. This would suggest the possibility that GFP molecules that did not aggregate were in some cases tagged with two Nanogold particles, one for each His tag. The non random assembly of the gold in Figures 40 and 41, and particularly the FFT image, would suggest that the gold and GFP have assembled into an organized lattice. The third confounding factor is that the high resolution images of the negatively stained GFP labeled with Nanogold very closely resembles negatively stained GFP. In retrospect this is not too unexpected, but it was hoped that the Nanogold would provide definitive and independent conformation that GFP was indeed imaged.

Despite falling short of expectations, the Nanogold still yielded interesting results. Based on comparisons between Figures 42 and 43, washing the specimen positively increased contrast between the Nanogold and UA, because the darker gold particles can be more

easily differentiated. Presumably washing the specimen removes unbound UA and Gold, thus clearing the viewing area of objects that would otherwise disrupt the image. Figure 43 importantly demonstrates that the gold has selectively labeled the sample or otherwise aggregated with it. It is not known whether this represents selective biding because negatively stained Nanogold also seems to clump. Figure 43, along with having superior contrast, shows many objects which approximate the 3 by 4 nm dimensions of the GFP beta-barrel, some closely associated with gold particles. Several examples are reproduced in Figure 53 below. Thus the Nanogold labeling might be considered somewhat of a success. However the aggregation of the sample brings the selectivity of the binding into doubt. Thus while Figure 53 might look impressive, it is with the current data impossible to know if the gold truly was bound in a selective manner to GFP. Doubtless control experiments using a recombinant protein without a His tag would provide some insight into this matter.

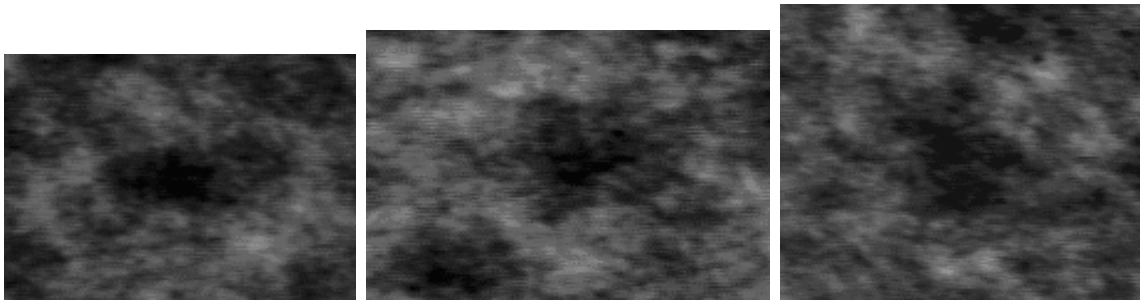

Figure 53 displays enlarged images taken at 450K from Figure 43. The gallery shows Nanogold in close proximity to what may be a GFP molecule.

Because the preparation used in Figures 45 and 46 used a more dilute Nanogold concentration, those images more closely resemble negatively stained GFP. Figure 54 displays a gallery of images of objects circled in Figure 45 which are suspected of being

discrete GFP molecules. They closely resemble those galleries displayed in Figures 49 through 52 of the negatively stained GFP specimens.

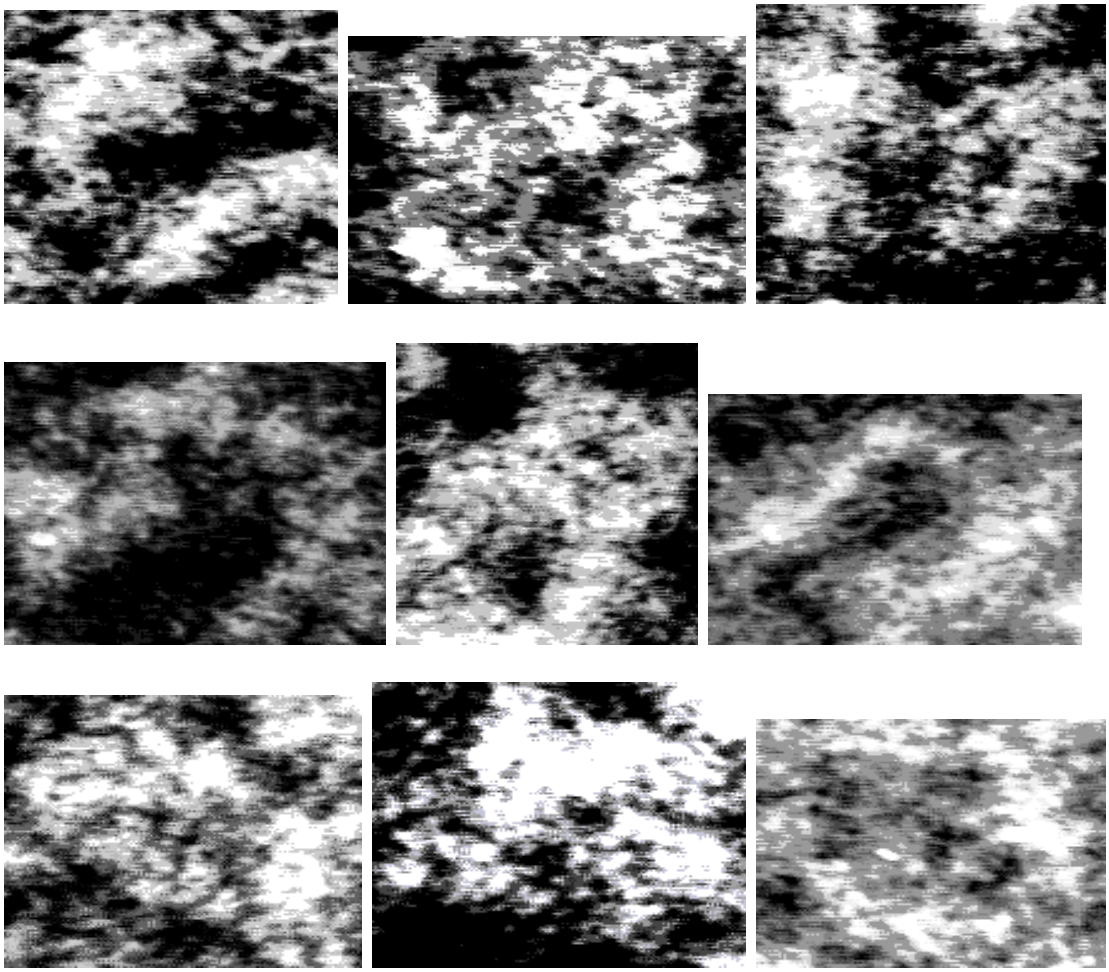

Figure 54 displays enlarged objects from Figure 45 under 450K magnification which are believed to be discrete GFP molecules.

The Future

This study, which is ongoing, investigated the structure of the green fluorescent protein, novel and unexpected aggregation phenomena, and used fluorescence as an indicator of protein integrity under the conditions of the electron microscope. Future experiments will continue to push the resolution of TEM for biological molecules. Notably immunolabeling by polyclonal anti-GFP and anti-His tag antibodies will comprise the

next phase of the experiment. The next challenge will be to determine if antibodies can be imaged with the same technique used to resolve GFP. If so, it may be possible to capture an image of an antibody binding to GFP, thus independently confirming with incontrovertible evidence that those objects believed to be the discrete GFP molecules are indeed GFP. Extensive circumstantial evidence suggests that the images are of GFP: The observation of fluorescing crystal structures in TEM micrographs; The visualization of ordered crystalline monolayers of 3 by 4 nm barrel shaped objects; The visualization of 3 by 4 nm barrel shaped objects is the less well defined GFP aggregates; Evidence of secondary protein structure; the HRTEM resolution of deferential UA deposition on the GFP objects; and the observation of what appears to be an ordered lattice of GFP and Nanogold. With time this technique might be refined and offer useful alternatives to cryo-EM and X-ray crystallography for proteins and biological molecules that do not readily crystallize or which form insoluble aggregates. Most importantly, the successful resolution of GFP represents a successful proof of method that TEM with relatively simple sample preparation techniques and minimum image processing can nonetheless provide a powerful tool in structural biology studies.

References

Alkaabi, Klaithem, Yafea, A., Ashraf, S. Effect of pH on thermal- and chemical-induced denaturation of GFP. 2005. Applied Biochemistry and Biotechnology, Volume 126, Number 2, pp. 149-156(8)

Apkarian, R.P., Dong J., Lynn D.G. 2002. Tem Analysis of B-Amyloid Fibrillogenesis: New Strategyold Problem. Microscopy and Microanalysis. 8 (Suppl. 02): pp. 830-831

Brown, Jr. R.M, Barnes, Z., Sawatari, C., and T. Kondo. 2007. Polymer Manipulation and Nanofabrication in real time using transmission electron microscopy. Biomacromolecules 8**:** 70-76.

Griffiths, Gareth. 2001. Bringing electron microscopy back into focus for cell biology. ScienceDirect. Volume 11, Issue 4, pp. 153-154

Hyat, M. A. 2000. Principles and Techniques of Electron Microscopy Biological Applications." 4th Edition. Cambridge University Press. Pages 343-344

Inoue, Shinya. Fluorescence Polarization of GFP Crystals. Biol. Bull. 201: 231–233. 2001

Jiang, Wen, Baker, M., Jakana, J., Weigele, P., King J. and, Chiu, W. Backbone structure of the infectious 15 virus capsid revealed by electron cryomicroscopy. 2008. Nature 451, 1130-1134

Kondo, T., Togawa, E. and R. M. Brown, Jr. 2001. Nematic Ordered Cellulose; A concept of glucan chain associations. Biomacromolocules 2: 1234-1330

Mycek, Mary-An and Pogue, Brian W. 2003. Handbook of Biomedical Fluorescence. CRC Press. pp. 434

Piston, David, Patterson, G., Lippincott-Schwartz, J., Claxton, N., and Davidson, M. 2007. Introduction to Fluorescent Proteins. Nikon. URL source:
http://www.microscopyu.com/articles/livecellimaging/fpintro.html

Saibil, Helen R. 2000. Conformational changes studied by cryo-electron microscopy. Nature Structural Biology 7, 711 - 714 doi:10.1038/78923

Schrödel, Andrea and Ario de Marco. 2005 Characterization of the aggregates formed during recombinant protein expression in bacteria. BMC Biochemistry. 6**:**10doi:10.1186/1471-2091-6-10

Sharp, Judith A. and R. M. Brown, Jr. 1995. Atomic and Molecular Imaging with the Transmission Electron Microscope. URL: http://www.botany.utexas.edu/facstaff/facpages/mbrown/ongres/jsharp.htm

Spires, Tara and R. M. Brown, Jr. 1998. An Introduction to High Resolution Transmission Electron Microscopy. URL Source:
http://www.botany.utexas.edu/facstaff/facpages/mbrown/ongres/tspires/poster.htm

Tsien, Roger. 1998. The Green Fluorescent Protein Annu. Rev. Biochem. 67:509–44.

Wille, Holger, Govaerts, C., Borovinskiy, A., Latawiec, D., Downing, K., Cohen, F., and Prusiner, S. Electron crystallography of the scrapie prion protein complexed with heavy metals. 2007. Biochemistry and Biophysics Volume 467, Issue 3, pp. 239-248

Yang, F., Moss, L. G. and Phillips, G. N. 1996. The Molecular Structure of Green Fluorescent Protein. Nat. Biotechnol. 14, 1246–1251

Acknowledgements

I would like to express heartfelt gratitude to my research advisor and mentor, Dr. R. Malcolm Brown Jr., who taught me to use the transmission electron microscope and whose skill with device is responsible for capturing many of the eloquent and profound images presented in this paper. Also many thanks are in order to individuals at The R. Malcolm Brown Jr. Laboratory for Cellulose and Biofuels Research including Ms. Kalpa Mehta, Mr. Richard Santos, and Dr. David Nobles for their support, insights, and gracious contributions of technical knowledge and assistance during this endeavor. This study has been supported by a grant from the Welch Foundation (F-1217) to Dr. Brown.

Appendix: How Does a Transmission Electron Microscope Work?

Transmission electron microscopy (TEM) was devised in response to the physical limitations of light microscopy. Originally used for locating defects in bulk materials, electron microscopes have become routine tools of inquiry in biological, chemical, and physical research as resolution improved (Brown, 1998). In the past twenty years, especially as electron microscope designs and specimen preparation techniques have improved, the field of cell biology has benefited greatly from electron microscopy (Brown, 2007).

The correlation between the limit of resolution and the wavelength of the illuminating radiation remains true for all forms of radiation, including visible light and electrons. Namely, the limit of resolution increases with decreased wavelength because in physical terms, a given wavelength of light may not interrogate material features significantly shorter than its own wavelength (Gibbs, 2002).

Electrons like photons, according to the de Broglie hypothesis, exhibit wave particle duality. The de Broglie relation simply states that the wavelength of a particle is inversely proportional to the momentum of the particle and that its frequency is directly proportional to the particle's kinetic energy. The derivation of the relation is as follows. Starting with the energy of a photon (E), refer to Equation 1, in terms of its frequency (ν) and planks constant (h), (E) is then equated to Einstein's special theory of relativity which yields an expression in terms of (m), the non zero relativistic mass of light which is none-zero because it travels at the speed of light, and (c), the velocity of light. Recalling, refer to Equation 2, that frequency (ν) may be expressed in terms of the velocity of light and wavelength (λ), the wavelength of a photon may be expressed by Equation 3. The analogous form of Equation 3 for objects that do not travel at the speed of light is the de Broglie relation, or Equation 4, were (m) is the mass of the particle, v is the velocity of the particle, and p is the momentum of the particle (Nave, 2005).

$$E = h\nu = mc^2 \qquad \text{(i)}$$

$$\nu = c / \lambda \qquad \text{(ii)}$$

$$\lambda = h / mc \qquad \text{(iii)}$$

$$\lambda = h / mv = h / p \qquad \text{(iv)}$$

In simple terms, the wavelength of an electron decreases as its velocity increases. For example, an electron microscope with an accelerating voltage of 100,000 V would produce an electron beam of wavelength .004 nm (Gibbs, 2002). Equation 5 is de Broglie's relation, but with accelerating voltage V substituted for momentum (Brown, 2007).

$$\lambda = 12.26/\sqrt{V} \qquad \text{(v)}$$

Theoretically, the resolution of such an electron microscope would be approximately .002 nm, or 10^4 times the limit of resolution for light microscopy. However, for reasons to be discussed shortly, the practical limit of resolution for modern electron microscopes is no smaller than .1 nm (1 Å) (Gibbs, 2002). But first, if all matter exhibits wave particle duality as de Broglie's relation implies, why can larger objects, say a baseball, aside from their destructive effects on specimens, not be employed in microscopy? Calculating the de Broglie wavelength of a .15 Kg baseball thrown at 40 m/s yields a λ value of $1.1*10^{-34}$ m, which is significantly less than the diameter of a proton. The implication for mundane objects is that wave particle duality will never be observed, because their wavelengths are infinitely minute (Nave, 2005).

Returning to the practical resolving power of electron microscopes, multiple difficulties further reduce the limit of resolution. First, the numerical apertures of electromagnetic lenses are relatively small by necessity (more on this later). In addition, preparation of specimens, contrast, and electron beam damage limit the practical resolution for biological specimens. However, this still represents a vast improvement over light microcopy with 100 times the effective resolution (Gibbs, 2002). Most severely though, resolution is limited by poor contrast at high magnifications. Both phase and amplitude contrast contribute to the image. Phase contrast is analogous to phase contrast light microscopy whereby light or in the case of TEM, electrons are retarded by the specimen and remain out of phase with electrons that did not transverse the specimen. Phase contrast may be enhanced through under focusing the image. Amplitude contrast represents a loss of electron density from the beam. Electron scattering within the specimen contributes to amplitude contrast and may be enhanced through certain staining techniques which will be discussed later (Brown, 2007).

Notable achievements within electron microcopy include Huxley's inquiry into skeletal muscle that would ultimately support the sliding filament model of muscle contraction and Branton's use of freeze-fracture techniques to visualize transmembrane proteins. In addition, electron microscopy has proved invaluable for visualizing viruses, bacteria, cytoskeletal filaments, and providing high resolution images of specimens (Gibbs, 2002).

For the remainder of the introduction, the configuration of the transmission electron microscope will be discussed. For clarification, refer to Figure 2, which displays the specifications for the Philips EM420 microscope used in this study. For organizational purposes, the structure of the transmission electron microscope may be divided into the electron source, associated vacuum systems, electromagnetic lenses, and imaging system.

Just as the light source in light microscopy provides the necessary photons to bombard specimens with, the electron source produces the electron beam. Electron sources, like photon sources, are diverse. One crude method for producing an electron beam is to induce strong external positive charges that attract electrons from the source within a confined space. However, such an approach does not produce a constant electron beam of uniform velocity and requires relatively copious amounts of accelerating voltage that may harm the specimen. The Philips EM420 used in this study employs a more docile process whereby therminonic emission from a tungsten wire is induced by passing a

current though the filament. Heating the filament to 2200ºK results in significant electron emission. For the purpose of producing a constant electron beam, a biased electron gun is employed; refer to Figure 2 position 1. The filament is enclosed by a Wehnelt cylinder which possesses a net negative charge. The aperture of the cylinder hence focuses the electrons, because of Coulomb's law. An anode positioned after the opening of the Wehnelt cylinder provides the necessary accelerating voltage, ranging from 80 to 120 kilovolts, to generate the electron beam (Brown, 2007).

Because accelerated electrons transverse only one centimeter at atmospheric pressure, a complex set of vacuum systems is required for the electron beam to cross the distances necessitated by the length of electron microscope. The vacuum systems are in series and include a mechanical pump, oil diffusion pump, and ion-getter pump. The mechanical pump alone achieves a vacuum of approximately 10^{-2} Torr; however, 10^{-4} Torr is required for the electron microscope to operate effectively. The oil diffusion pump further adds to the vacuum. It consists of a low vapor pressure oil which is heated in the vacuum created by the mechanical pump. The oil undergoes a phase change into vapor as a result of heating and low atmospheric pressure. The pump itself is highly convoluted and allows for the vapor to condense on a vast surface area. When the condensed oil droplets return the liquid phase, residual gasses are sequestered or dissolved in the liquid phase of the oil, thus further reducing the pressure within the electron microscope. However, care must be taken to ensure that oil vapor does not come into contact with the delicate and complex pieces of the electron microscope. This possibility is regulated by physical shielding and cryoshielding, which is simply lowering the temperature of the highly convoluted baffle surfaces of the pump that encourage condensation. Finally, an ion-getter pump acts to trap remaining gas molecules on titanium plates, which attract ionized gas molecules which were imparted with charge by the accelerating voltage. In addition, the Philips 420 TEM possesses a 200 μm aperture between the projector lens and camera system; Refer to Figure 2 position 4. The aperture acts to ensure that oil vapor does not penetrate the delicate devices, such as the electromagnetic lenses and electron source (Brown, 2007).

The electromagnetic lenses, located a positions 2 and 4 of Figure 2, are quite complicated and serve to collect, focus, and manipulate the electron beam much like a light microscope manipulates light rays. The trajectory of an electron may be influenced in one of two ways. The first, known as an electrostatic lens, is somewhat antiquated and not employed by the Philips 420 TEM. The electrostatic lens relies on an electric field to change the velocity and direction of electrons where the refractive index is proportional to the square root of the field strength. However, the electrostatic lens separates electrons only along the field lines generated by the electric field. This process results in unsymmetrical field variations that ultimately hinder the resolving power of the lens system. An electromagnetic lens, the variety used by the Philips 420 TEM, employs a magnetic field that alters only the path of the electron. The lens itself is quite complicated and consist of a pole piece and solenoid electromagnetic windings. The strength of the magnetic field is influenced by changing the current that flows through the solenoid. Recall from electromagnetism that moving charges generate a magnetic field. The analytical electronics that regulate the electromagnetic lens used in TEM are beyond

the scope of this paper, but refer to Figure 1 for an approximate illustration of the electron beam's distortion by the condenser and objective lenses. Note in Figure 2 position 2, that four lenses are employed in the condenser apparatus and in position 4, that 5 lenses are employed in the objective apparatus. Figure 1 displays the approximate path of the electron beam path as it is condensed, transmitted through the specimen, and later collected by the objective lens, and finally transmitted to the imaging device (Brown, 2007).

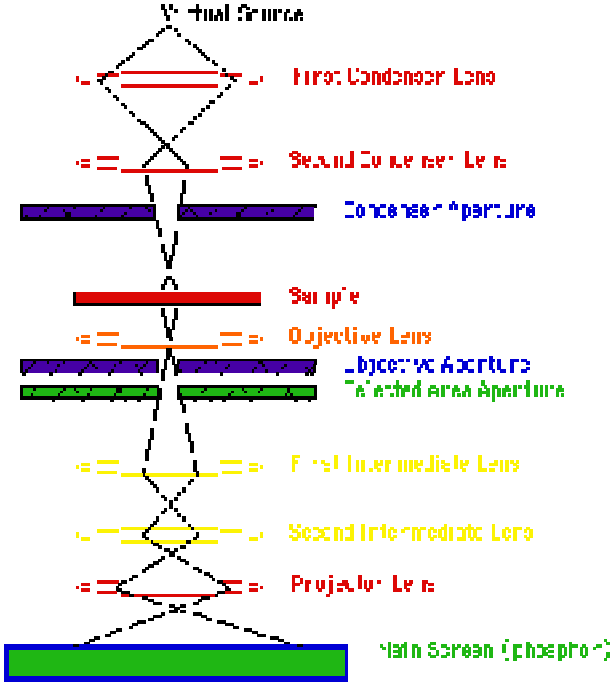

Figure 1: Simplified illustration of the electron beam path through the TEM (CMRA).

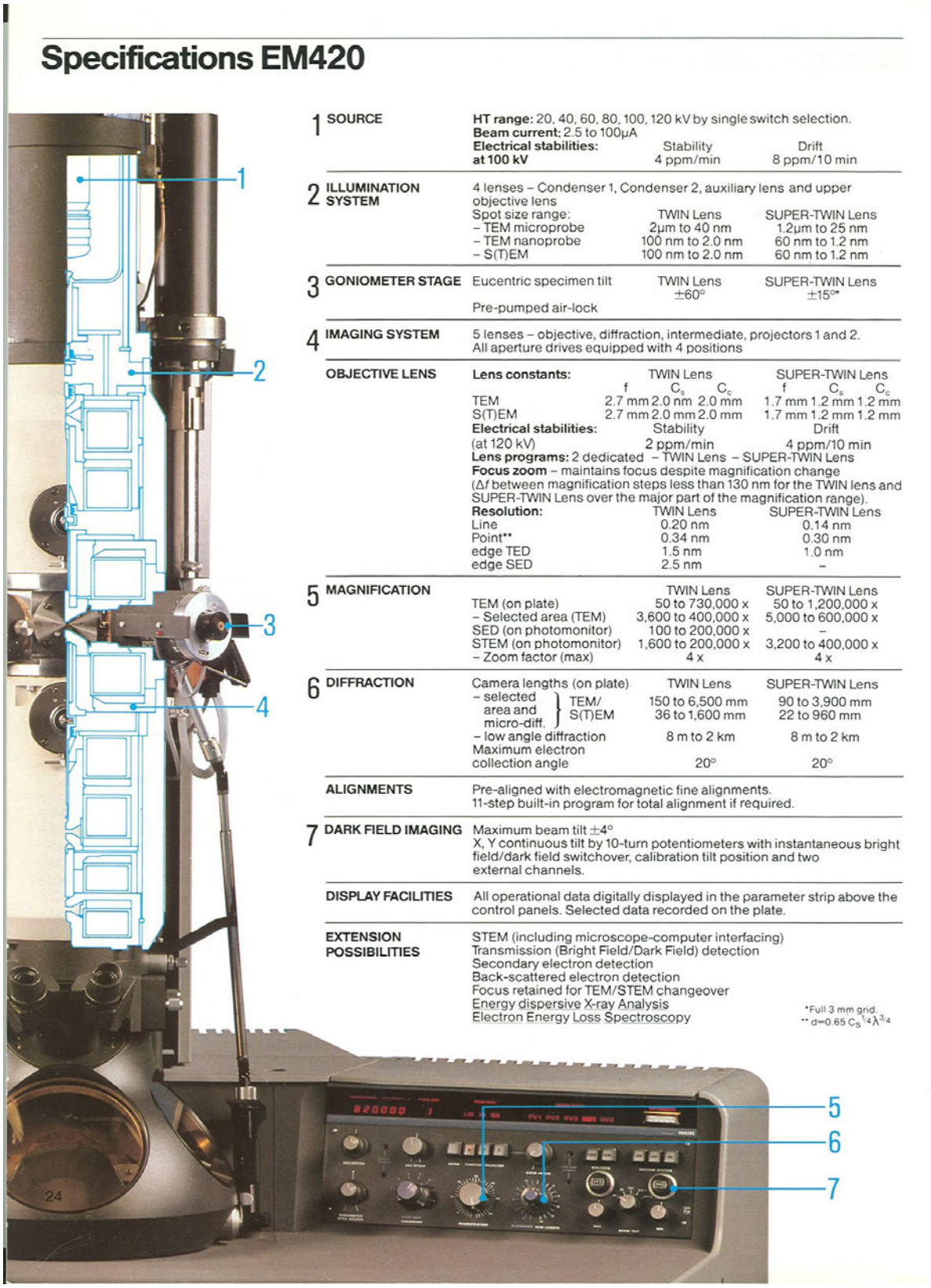

Figure 2: Figure 2 displays the complex intricacies of the Philips 420 TEM used in this study.

Briefly, the imaging system, refer to Figure 2 position 4, employed by the Philips 420 TEM must convert electron signals into photon signals. This is accomplished through the use of a yttrium aluminum garnet crystal. When electrons bombard the surface of the crystal, photons are emitted in what might be considered to be the photoelectric effect in reverse. An oil coupled interface transmits the photon image to a low light level system (silicon intensified diode) that can detect light as low as $1*10^{-6}$ footcandles. Electron signals are converted to high resolution photon images using a Gatan camera system consisting of an yttrium aluminum garnet (YAG) crystal. The image is subsequently transmitted to a Kontron IBAS imaging system where it is digitized at a final screen magnification of approximately 18 times the instrument magnification. Besides the Gatan camera system, an ion-getter pump maintains a clean vacuum which exceeds 10^{-7} Torr at the specimen level. These factors, along with the use of a tungsten filament and biased electron gun, which provides a uniform and coherent electron beam, allow for this Philips instrument to regularly resolve 3.35 Å graphite lattices in addition to 2.01 Å atomic gold lattices. The image may then be digitally transferred to any compatible media (Brown, 2007).

References (for the Appendix)

Jaszczak, John. "Graphite Crystal Structures." The Graphite Page. Jul 2006: http://www.phy.mtu.edu/~jaszczak/graphite.html

Brown, Malcolm. "Section IX and X: Electron Microscopy." Laboratory Studies in Cell Biology. University Co-op, 2007.

Brown, Malcolm. "An Introduction to High Resolution Transmission Electron Microscopy." Tara Spires. Feb 1998: http://www.botany.utexas.edu/facstaff/facpages/mbrown/ongres/tspires/poster.htm

Gibbs, Sarah. ed. Molecular Biology of the Cell. 4th ed. New York. Garland Science, 2002.

Nave, C.R. Wave Nature of Electron. Hyperphysics. 2005: http://hyperphysics.phy-astr.gsu.edu/hbase/debrog.html#c5

"Transmission Electron Microscope." CMRA. http://www.unl.edu/CMRAcfem/temoptic.htm